COMPUTATIONAL MODELLING OF ELECTRO-ACTIVE POLYMERS

A THESIS SUBMITTED TO
THE GRADUATE SCHOOL OF NATURAL AND APPLIED SCIENCES
OF
MIDDLE EAST TECHNICAL UNIVERSITY

BY

SİNAN FIRAT DAL

IN PARTIAL FULFILLMENT OF THE REQUIREMENTS
FOR
THE DEGREE OF MASTER OF SCIENCE
IN
CIVIL ENGINEERING

AUGUST 2019

Approval of the thesis:

COMPUTATIONAL MODELLING OF ELECTRO-ACTIVE POLYMERS

submitted by **SİNAN FIRAT DAL** in partial fulfillment of the requirements for the degree of **Master of Science in Civil Engineering Department, Middle East Technical University** by,

Prof. Dr. Halil Kalıpçılar
Dean, Graduate School of **Natural and Applied Sciences** _____

Prof. Dr. Ahmet Türer
Head of Department, **Civil Engineering** _____

Assoc. Prof. Dr. Serdar Göktepe
Supervisor, **Civil Engineering Department, METU** _____

Examining Committee Members:

Prof. Dr. İsmail Özgür YAMAN
Civil Engineering Department, METU _____

Assoc. Prof. Dr. Serdar Göktepe
Civil Engineering Department, METU _____

Prof. Dr. Suat Kadıoğlu
Mechanical Engineering Department, METU _____

Assist. Prof. Dr. Onur Pekcan
Civil Engineering Department, METU _____

Assist. Prof. Dr. Besim Baranoğlu
Manufacturing Engineering Department, Atılım University _____

Date: _____

I hereby declare that all information in this document has been obtained and presented in accordance with academic rules and ethical conduct. I also declare that, as required by these rules and conduct, I have fully cited and referenced all material and results that are not original to this work.

Name, Surname: Sinan Fırat Dal

Signature :

ABSTRACT

COMPUTATIONAL MODELLING OF ELECTRO-ACTIVE POLYMERS

Dal, Sinan Fırat
M.S., Department of Civil Engineering
Supervisor: Assoc. Prof. Dr. Serdar Göktepe

August 2019, 92 pages

This study is concerned with the stability of Electro-Active Polymers (EAPs) having geometries with periodic microstructures subjected to coupled electromechanical effects. For this purpose, coupled electromechanical equations, which are nonlinear, are discretized using the Finite Element Method (FEM) under the prescribed boundary conditions.

EAPs are smart materials that may undergo large mechanical deformations when subjected to an electric field. Unlike many other materials that show permanent deformations under the influence of the electric field, EAPs can return to their original shapes when the electric field is deactivated. In addition, EAPs are used in many engineering applications where robot and artificial muscle production are effective since they can respond quickly to the electrical fields to which they are exposed. In order to study the coupled electro-mechanical behavior of EAPs, two different but coupled differential equations must be solved. The governing equations of coupled electro-mechanics are introduced by the Maxwell equations for electrostatics and the conservation of linear momentum for elastostatics. These two differential equations are discretized

in space by using FEM. Since the residual vector formed through discretization is still non-linear, linearization must be performed. As a result, the equation system of degrees of freedom is solved iteratively by using the Newton method. Different material models are used to analyze the coupled problem. The efficiency of the models are tested through numerical examples of benchmark problems borrowed from various references.

Moreover, the developed computational model of coupled electro-mechanics is further used to analyze the behavior of porous EAPs with periodic microstructures. The effect of electro-mechanical coupling on the stability behavior of EAPs is investigated through stability analyzes in the presence of an electric field for representative geometries with periodic microstructures. It is shown that in the presence of an electric field not only the value of the critical load where the pattern transformation takes place can be shifted but also the shape of the final pattern can be totally changed.

Keywords: Electro-Active Polymers (EAPs), Finite Element Method (FEM), Periodic Microstructures, Pattern Transformation

ÖZ

ELEKTRO-AKTİF POLİMERLERİN HESAPLAMALI MODELLENMESİ

Dal, Sinan Fırat
Yüksek Lisans, İnşaat Mühendisliği Bölümü
Tez Yöneticisi: Doç. Dr. Serdar Göktepe

Ağustos 2019 , 92 sayfa

Bu çalışma, bağlaşık elektromekanik etkilere maruz kalan periyodik mikro yapılı geometrilere sahip bulunan Elektro Aktif Polimerlerin (EAP) kararlılıklarını konu almaktadır. Bu amaçla, doğrusal olmayan bağlaşık elektromekanik denklemler, belirtilen sınır koşulları altında Sonlu Elemanlar Yöntemi (SEY) ile ayrıklaştırılarak çözülmektedir.

EAP'ler, elektrik alana maruz kaldıklarında büyük mekanik deformasyonlar gösteren akıllı malzemelerdir. Elektrik alanın etkisi altında kalıcı deformasyonlar gösteren diğer birçok malzemeden farklı olarak, EAP'ler, elektrik alan devre dışı bırakıldığında ilk şekillerine dönebilirler. Ek olarak, EAP'ler maruz kaldıkları elektrik alanlarına hızlı bir şekilde tepki verebildiklerinden robot ve yapay kas üretiminin etkili olduğu birçok mühendislik uygulamasında kullanılmaktadır. EAP'lerin bağlaşık elektro-mekanik davranışını incelemek için iki farklı fakat birbiri ile bağlaşık diferansiyel denklemin çözülmesi gerekir. Bağlaşık elektro-mekaniğin ana denge denklemleri, elektrostatik için Maxwell denklemleri iken elastostatik için doğrusal momentumun korunumu yasasıdır. Bu iki diferansiyel denklem SEY kullanılarak konumsal

uzayda ayrıklaştırılır. Ayrıklaştırma yoluyla elde edilen artık vektör hala doğrusal olmadığından, doğrusallaştırma yapılmalıdır. Sonuç olarak, serbestlik dereceleri için oluşturulan denklem sistemi Newton metodu kullanılarak yinelemeli şekilde çözülür. Bağlaşık problemi analiz etmek için farklı malzeme modelleri kullanılmıştır. Modellerin verimliliği, çeşitli kaynaklardan alınan kıyaslama problemlerinin sayısal örnekleri ile test edilmiştir.

Öbür yandan, bağlaşık elektro-mekaniğin gelişmiş hesaplamalı modeli, gözenekli periyodik mikroyapılı EAP'lerin davranışını analiz etmek için de kullanılmıştır. Bağlaşık elektro-mekaniğin EAP'lerin kararlılık davranışı üzerindeki etkisi, periyodik mikro yapıları olan temsili geometriler için elektrik alanın varlığında kararlılık analizleri yapılarak araştırılmıştır. Elektrik alanın varlığında, sadece malzemenin ilk örüntüsünü değiştiren kritik yük değerinin ötelenmediği, son örüntü şeklinin de tamamen değiştiği gösterilmektedir.

Anahtar Kelimeler: Elektro-Aktif Polimerler (EAP), Sonlu Elemanlar Yöntemi (SEY), Periyodik Mikroyapılar, Örüntü Dönüşümü

Dedicated to all my loved ones.

ACKNOWLEDGMENTS

This thesis was completed between the years 2016-2019 when I worked as a research assistant in the Department of Civil Engineering at Middle East Technical University. Therefore, I would like to thank everyone who contributed to me until I ended this work.

First, I would like to thank my thesis advisor, Assoc. Prof. Dr. Serdar Göktepe for his faith and trust in me. I was able to complete this work thanks to his patience, experience and vast knowledge of mechanics. Without our numerous academic debates and examinations we had with him, I would never have completed this thesis successfully.

In addition, I would like to thank the jury members Prof. Dr. İsmail Özgür Yaman, Prof. Dr. Suat Kadıoğlu, Assist. Prof. Dr. Onur Pekcan, and Assist. Prof. Dr. Besim Baranoğlu for their constructive comments and help.

I will not pass without adding Prof. Dr. Turhan Yaşar Erdoğan who was passed away last year. He was not only the teacher of teachers in our department but he was also the one who behaves me as a second father. Dr. Erdoğan has played a major role in me being an assistant in the Department of Civil Engineering at Middle East Technical University. I can never forget Dr. Erdoğan's efforts on me.

Secondly, I would like to thank my dear wife, my life partner Saniye Rabia Dal, for her continued support, assistance and effort. Although she continues her thesis work, I cannot thank her enough for providing me with the support and love I need all the time. In addition, I would like to thank Satılmış Ozül, Sultan Ozül, Merve Nur Ozül, and Fehmi Ozül who are my wife's family. I will never forget their support and hospitality every time we meet.

I would also like to thank my mother Ayşe Dal and my lovely sister, Esin Doğa Dal, for never losing their faith in me, for being always by my side and always loving me. I hope that after this study, they will have found their prayers for me. I cannot forget

but mention my father's efforts. Unfortunately, he could not see for himself that I had finished this work. But I can feel him watching me from the heaven and being proud of me. I will always feel his and my mother's love in my heart.

I would like to thank Mehran Ghasabeh and Özgür Paşaoğlu for their assistance and advice on many issues during my graduate studies. I would also like to thank my roommates and my colleagues Sepehr Sayedian Choubi, Berkay Akçören and Bilgin Koçak for listening to my troubles and helping me. In short, I would like to thank all my colleagues for providing a friendly and calm work environment.

TABLE OF CONTENTS

ABSTRACT v

ÖZ vii

ACKNOWLEDGMENTS x

TABLE OF CONTENTS xii

LIST OF TABLES xv

LIST OF FIGURES xvi

LIST OF ABBREVIATIONS AND SYMBOLS xix

CHAPTERS

1 INTRODUCTION 1

1.1 Motivation and Problem Definition 1

1.2 Smart Material: Electro-Active Polymers 4

1.3 Pattern Transformation of Solids 7

1.4 Challenges 9

1.5 Contributions and Novelties 9

1.6 The Outline of the Thesis 9

2 FUNDAMENTALS OF CONTINUUM MECHANICS AND ELECTROSTATICS 11

2.1 Fundamentals of Continuum Mechanics 11

2.1.1 The Motion of a Material Body and Deformation Measures . . 12
2.1.2 Cauchy-Green Tensors 17
2.1.3 Material and Spatial Velocity Gradients 20
2.1.4 The Lie Derivative of Spatial Objects 21
2.1.5 The Cauchy's Mechanical Stress Theorem 22
2.2 Fundamentals of Electrostatics 25
2.2.1 Coulomb's Law and Lorentz Law of Force 26
2.2.2 Faraday's Law 27
2.2.3 Gauss's Flux Theorem 28
2.2.4 Electric Polarization and Electric Displacement Vector 29
2.2.5 Geometric Mapping For Electrical Objects 33
2.2.6 Balance Laws of Continuum Electromechanics 34
2.2.6.1 Conservation of Mass 35
2.2.6.2 Balance of Linear Momentum 36
2.2.6.3 Balance of Angular Momentum 38
2.2.6.4 Balance of Energy 40
2.2.6.5 Balance of Entropy 41
3 CONSTITUTIVE EQUATIONS 47
3.1 Model I 49
3.2 Model II 52
3.3 Model III 53
4 DISCRETIZATION OF THE COUPLED EQUATIONS 55
4.1 Preliminaries 55

4.2 Discretization using Finite Element Method 58

4.3 Linearization of Galerkin Functional 59

4.4 Discretization of Galerkin Functionals 62

5 NUMERICAL EXAMPLES 65

5.1 Coupled Electromechanics 66

5.1.1 Example I: Bending Beam Actuator 66

5.1.2 Example II: C-Shaped Plate 71

5.2 Pattern Transformations in Porous Elastomers 73

5.3 Pattern Transformations in Porous EAPs Under Electromechanical Loading 77

5.3.1 Uniform Electric Field in Elements 77

5.3.2 Uniform Electric Potentials on Edges 80

5.3.3 Uniform Electric Potentials on Edges For Microscale Model . 82

6 CONCLUSION 85

REFERENCES 87

LIST OF TABLES

TABLES

Table 1.1 The list of electronic and ionic EAPs [1, 2] 6

Table 3.1 Material Properties for Model I 51

Table 3.2 Material Properties for Model II 53

Table 3.3 Material Properties for Model III 54

Table 5.1 Geometric properties of the microstructure 75

Table 5.2 The value of $x-$ and $y-$components of the applied electric field in each element $\mathcal{B}^e$ 78

Table 5.3 The value of $x-$ and $y-$components of the applied electric fields $\boldsymbol{e}_1$ and $\boldsymbol{e}_2$ 79

LIST OF FIGURES

FIGURES

Figure 1.1 Scanning Electron Micrograph (SEM) views of iridescent setea from Polychaete worm [3] with (a) 2 μm, (b) 5 μm, (c) 1 μm, and (d) 120 nm. 3

Figure 2.1 The motion of a solid body in time $t \in \mathbb{R}_+$. 13

Figure 2.2 The *deformation gradient*, $\boldsymbol{F}$, transforms tangential vector $d\boldsymbol{X} \in T_X\mathcal{B}$ in reference configuration into its counterpart in current configuration $d\boldsymbol{x} \in T_x\mathcal{S}$ by $d\boldsymbol{x} := \boldsymbol{F}d\boldsymbol{X}$. 14

Figure 2.3 The *volume map* ($J :=$ det$\boldsymbol{F}$) maps infinitesimal volume element dV in reference configuration into the infinitesimal volume element in current configuration dv by $dv := JdV$. 15

Figure 2.4 The *normal map* (cof$\big[\boldsymbol{F}\big]$) transforms normal vector $\boldsymbol{N}dA \in T^*_X\mathcal{B}$ in reference configuration into its counterpart in current configuration $\boldsymbol{n}da \in T^*_x\mathcal{S}$ by $\boldsymbol{n}da :=$ cof$\big[\boldsymbol{F}\big]\boldsymbol{N}dA$. 16

Figure 2.5 *Commutative Diagram* for deformation tensors. Combination of the *push-forward* and *pull-back* operations among the deformation tensors. 20

Figure 2.6 *Euler's Cut Principle*. The undeformed $\mathcal{P}_\mathcal{B}$ and deformed $\mathcal{P}_\mathcal{S}$ parts, their corresponding traction and normal vectors. 22

Figure 2.7 *Commutative Diagram* for stress tensors. Combination of the *push-forward* and *pull-back* operations among the stress measures. . . . 25

Figure 2.8 *Commutative Diagram* for electrostatical objects in each configuration. 34

Figure 5.1 Representation of the bending actuator and its dimensions. . . . 67

Figure 5.2 2D representation of the bending actuator with an applied electric voltage difference. 67

Figure 5.3 Deformed shapes of bending actuator. 68

Figure 5.4 The stretch distribution on the undeformed form of the bending beam actuator. 69

Figure 5.5 Potential difference vs. normalized displacement of Point A in $x-$direction. 70

Figure 5.6 Potential difference vs. normalized displacement of Point A in $y-$direction. 70

Figure 5.7 Dimensions of the C-shaped plate and quadrilateral mesh for standard FEM. 71

Figure 5.8 Applied electrical boundary conditions on the C-shaped plate. . . 72

Figure 5.9 $\epsilon_r = 5\epsilon_0$ with electric potentials applied on upper and lower boundary of the plate. 72

Figure 5.10 $\epsilon_r = 10\epsilon_0$ with electric potentials applied on upper and lower boundary of the plate. 73

Figure 5.11 $\epsilon_r = 100\epsilon_0$ with electric potentials applied on upper and lower boundary of the plate. 73

Figure 5.12 The dimensions of periodic microstructures (left) and quadratic triangular mesh and boundary conditions (right). 74

Figure 5.13 The pattern transformation between undeformed and deformed state. 75

Figure 5.14 Comparison of the nominal stress-strain graph for different meshes with [4, 5]. 76

Figure 5.15 (a) Uniform electric field applied in each element $\mathcal{B}^e$ (b) Deformed shape of the periodic microstructure under combined electric field and compressive load $u_d = 4.985$ mm. 77

Figure 5.16 (a) Uniform electric field which the magnitude but different directions applied to different portions of the microstructure (b) Deformed shape of the periodic microstructure under combined electric fields in different directions and compressive load. 79

Figure 5.17 Nominal stress-strain graph for constant electric fields applied on different portions of the microstructure. 80

Figure 5.18 (a) Electric potentials are employed on the left and right edge of the microstructure and (b) Deformed shape of the periodic microstructure under the influence of applied electric potentials and compression. . 81

Figure 5.19 Nominal stress-strain graph for applied electric potentials on the left and right surfaces of the microstructure. 82

Figure 5.20 Deformed shapes of the periodic microstructure under combined electric field and compressive load. 83

Figure 5.21 Nominal stress-strain graph for applied electric potentials on the left and right surfaces of the micron sized microstructure. 83

LIST OF ABBREVIATIONS AND SYMBOLS

EAPs	Electro-Active Polymers
FEM	Finite Element Method
BEM-FEM	Coupled Boundary Element Method and Finite Element Method
REA	Refined Eigen Analysis
CPI	Clausius-Planck Inequality
FI	Fourier Inequality
PBC	Periodic Boundary Conditions
B	A material body
P	A material point
$\mathbb{R}^3$	The three dimensional Euclidean space
t	Any instant of time
$\boldsymbol{\chi}$	The configuration of the material body
$\boldsymbol{\chi}_{t_0}$	The initial configuration of the body
$\boldsymbol{\chi}_t$	The configuration of the body at current time $t > t_0$
$\mathcal{B}$	The reference state
$\mathcal{S}$	The current state
$\boldsymbol{X}$	The position vector of a material point P
$\boldsymbol{x}$	The spatial position vector
X^I	The indicial representation of reference position vector
x^i	The indicial representation of current position vector
$\boldsymbol{E}_I$	The indicial representation of the basis vector for Lagrangian configuration in Euclidean space
$\boldsymbol{e}_i$	The indicial representation of the basis vector for Eulerian configuration in Euclidean space

$\boldsymbol{\varphi}_t(\boldsymbol{X})$	The non-linear deformation map
$\boldsymbol{\varphi}_t^{-1}(\boldsymbol{x})$	The inverse of the non-linear deformation map
$\boldsymbol{V}(\boldsymbol{X}, t)$	The material velocity vector
$\boldsymbol{A}(\boldsymbol{X}, t)$	The material acceleration vector
$\boldsymbol{v}(\boldsymbol{x}, t)$	The spatial velocity vector
$\boldsymbol{a}(\boldsymbol{x}, t)$	The spatial acceleration vector
$\boldsymbol{T}$	A tangent vector in the reference configuration
$\boldsymbol{t}$	A tangent vector in the spatial configuration
$\boldsymbol{F}$	Tangent map (the deformation gradient tensor)
T^I	The indicial representation of a tangent vector in the reference configuration
t^i	The indicial representation of a tangent vector in the spatial configuration
F^i_I	The indicial representation of the deformation gradient tensor
J	Jacobian (volume) map
$\det(\boldsymbol{F})$	The determinant of the deformation gradient
$\boldsymbol{N}$	A unit normal vector in the reference configuration
$\boldsymbol{n}$	A unit normal vector in the spatial configuration
$\boldsymbol{F}^{-T}$	Normal Map
N_I	The indicial representation of a normal vector in the reference configuration
n_i	The indicial representation of a normal vector in the spatial configuration
$(F^{-1})^I_i$	The indicial representation of the inverse of the deformation gradient tensor
$\boldsymbol{G}$	Co-variant reference metric tensor
$\boldsymbol{g}$	Co-variant spatial metric tensor
$\boldsymbol{G}^{-1}$	The inverse of the co-variant metric tensor in the reference configuration

$\boldsymbol{g}^{-1}$	The inverse of the co-variant metric tensor in the spatial configuration
G_{IJ}	The indicial representation of the co-variant reference metric tensor
g_{ij}	The indicial representation of the co-variant spatial metric tensor
$\left(G^{-1}\right)^{IJ}$	The indicial representation of the inverse of the co-variant reference metric tensor
$\left(g^{-1}\right)^{ij}$	The indicial representation of the inverse of the co-variant spatial metric tensor
$\boldsymbol{T}^{\flat}$	A material normal vector in the co-tangent space
$\boldsymbol{t}^{\flat}$	A spatial normal vector in the co-tangent space
T_I	The indicial representation of a normal vector in the reference configuration in the co-tangent space
t_i	The indicial representation of a normal vector in the spatial configuration in the co-tangent space
δ_{IJ}	Kronecker's delta for the fully index lowered case in the reference configuration
δ_{ij}	Kronecker's delta for the fully index lowered case in the spatial configuration
$\mid \boldsymbol{T} \mid_{\boldsymbol{G}}$	The length of the Lagrangian tangent vector $\boldsymbol{T}\left(\boldsymbol{X}\right)$
$\mid \boldsymbol{t} \mid_{\boldsymbol{g}}$	The length of the Eulerian tangent vector $\boldsymbol{t}\left(\boldsymbol{x}\right)$
$\mid \boldsymbol{N} \mid_{\boldsymbol{G}^{-1}}$	The length of the Lagrangian normal vector $\boldsymbol{N}\left(\boldsymbol{X}\right)$
$\mid \boldsymbol{n} \mid_{\boldsymbol{g}^{-1}}$	The length of the Eulerian normal vector $\boldsymbol{n}\left(\boldsymbol{x}\right)$
λ	The stretch
λ^{-1}	The inverse of the stretch
ν	The area stretch
ν^{-1}	The inverse of the area stretch
$\boldsymbol{C}$	The right Cauchy-Green deformation tensor

$\boldsymbol{C}^{-1}$	The inverse of the right Cauchy-Green deformation tensor
$\boldsymbol{b}$	The left Cauchy-Green deformation tensor
$\boldsymbol{\varphi}^{*}$	The pull-back operator
$\boldsymbol{\varphi}_{*}$	The push-forward operator
$\dot{\boldsymbol{t}}$	The time rate of change of a tangent vector
$\boldsymbol{L}$	The material velocity gradient
$\boldsymbol{l}$	The spatial velocity gradient
$\mathcal{L}_{\boldsymbol{v}}(\bullet)$	The Lie derivative of the spatial object
$\mathcal{P}_{\mathcal{B}}$	The material subdomain cut out off the material body $\mathcal{B}$
$\mathcal{P}_{\mathcal{S}}$	The spatial subdomain cut out off the spatial body $\mathcal{S}$
$\boldsymbol{t}$	The surface traction vector in Eulerian configuration (using fully Eulerian stress tensor)
$\boldsymbol{T}$	The surface traction vector in Eulerian configuration (using two-point stress tensor)
$\tilde{\boldsymbol{T}}$	The surface traction vector in Lagrangian configuration
$\boldsymbol{\sigma}$	The Cauchy stress tensor
$\boldsymbol{\tau}$	The Kirchhoff stress tensor
$\boldsymbol{P}$	The first Piola-Kirchhoff stress tensor
$\boldsymbol{S}$	The second Piola-Kirchhoff stress tensor
σ^{ij}	The indicial representation of the Cauchy stress tensor
τ^{ij}	The indicial representation of the Kirchhoff stress tensor
P^{iJ}	The indicial representation of the first Piola-Kirchhoff stress tensor
S^{IJ}	The indicial representation of the second Piola-Kirchhoff stress tensor
q	The charge at position $\boldsymbol{x}$
Q	The charge at position $\boldsymbol{x}'$
$\boldsymbol{f}$	The force of attraction between two charges (Coulomb's law)

ϵ_0	The electric permittivity of the free space ($8.854 \cdot 10^{-12} \left[\mathrm{F/m}\right]$)
ϵ_r	The relative electric permittivity
$\boldsymbol{e}$	The electric field vector in the spatial configuration
$\boldsymbol{E}$	The electric field vector in the reference configuration
$\boldsymbol{b}^{mg}$	The magnetic induction vector
ρ_e	The volume charge density within the confined volume
ϕ	The electrostatic potential or electric potential
grad $(\bullet)$	The gradient operator with respect to spatial position vector ($\nabla_{\boldsymbol{x}} (\bullet)$)
Grad $(\bullet)$	The gradient operator with respect to reference position vector ($\nabla_{\boldsymbol{X}} (\bullet)$)
div $(\bullet)$	The divergence operator with respect to spatial position vector ($\nabla_{\boldsymbol{x}} \cdot (\bullet)$)
Div $(\bullet)$	The divergence operator with respect to reference position vector ($\nabla_{\boldsymbol{X}} \cdot (\bullet)$)
curl $(\bullet)$	The curl operator with respect to spatial position vector ($\nabla_{\boldsymbol{x}} \times \nabla_{\boldsymbol{x}} (\bullet)$)
Curl $(\bullet)$	The curl operator with respect to reference position vector ($\nabla_{\boldsymbol{X}} \times \nabla_{\boldsymbol{X}} (\bullet)$)
W^e	The work done by electric field on a particle q
U_1	The potential energy density at position $\boldsymbol{x}_1$
U_2	The potential energy density at position $\boldsymbol{x}_2$
$\boldsymbol{\delta}$	The electric dipole vector or the electric dipole moment
$\boldsymbol{\Omega}$	The torque due to electric polarization and Coulomb force in the presence of electric field
$\boldsymbol{p}$	The electric polarization vector at position $\boldsymbol{x}$ directed from negative charges to positive charges in the spatial configuration
$\boldsymbol{P}$	The electric polarization vector in the reference configuration

$W^{\boldsymbol{p}}$	The total work done on electric dipole by the electric field vector
ρ_b	The volume charge density of the bound charges
ρ_f	The volume charge density of the free charges
σ_b	The surface charge density of the bound charges
σ_f	The surface charge density of the free charges
$\boldsymbol{d}$	The electric displacement vector in the spatial configuration
$\boldsymbol{D}$	The electric displacement vector in the reference configuration
$\mathcal{M}_{\mathcal{P}_\mathcal{B}}$	The mass of the material subdomain
$\mathcal{M}_{\mathcal{P}_\mathcal{S}}$	The mass of the spatial subdomain
ρ_0	The mass density in the Lagrangian setting
ρ	The mass density in the Eulerian setting
$\boldsymbol{\mathcal{I}}_{\mathcal{P}_\mathcal{S}}$	The linear momentum of the spatial subdomain
$\boldsymbol{\mathcal{F}}_{\mathcal{P}_\mathcal{S}}$	The sum of the forces acting on the spatial subdomain
$\boldsymbol{\gamma}$	The total body force vector
$\boldsymbol{\gamma}^m$	The mechanical body force vector
$\boldsymbol{\gamma}^e$	The electrical body force vector
$\boldsymbol{\sigma}$	The mechanical Cauchy stress tensor
$\boldsymbol{\sigma}^e$	The electric Maxwell stress tensor
$\overline{\boldsymbol{\sigma}}$	The total Cauchy stress tensor (symmetric)
$\boldsymbol{\mathcal{D}}_{\mathcal{P}_\mathcal{S}}$	The angular momentum of the spatial subdomain
$\boldsymbol{\mathcal{M}}_{\mathcal{P}_\mathcal{S}}$	The resultant moment acting on the spatial subdomain
ϵ_{ijk}	The indicial representation of the permutation symbol (Levi-Civita symbol)
$\boldsymbol{\omega}$	The skew-symmetric tensor of the mechanical Cauchy stress
$\mathcal{E}_{\mathcal{P}_\mathcal{S}}$	The total energy of the spatial subdomain
$\mathcal{K}_{\mathcal{P}_\mathcal{S}}$	The total kinetic energy of the spatial subdomain
$\mathcal{U}_{\mathcal{P}_\mathcal{S}}$	The total internal energy of the spatial subdomain

$\mathcal{P}_{\mathcal{P}_\mathcal{S}}$	The mechanical power of the spatial subdomain
$\mathcal{Q}_{\mathcal{P}_\mathcal{S}}$	The thermal power of the spatial subdomain
e	The internal energy density
r	The total energy supply
r^m	The mechanical energy supply
r^e	The electrical energy supply
$\boldsymbol{q}$	The heat flux vector
$\Gamma_{\mathcal{P}_\mathcal{S}}$	The total rate of entropy production of the spatial subdomain
$\dot{\mathcal{H}}_{\mathcal{P}_\mathcal{S}}$	The rate of entropy change of the spatial subdomain
$\dot{\mathcal{S}}_{\mathcal{P}_\mathcal{S}}$	The entropy power of the spatial subdomain
η	The mass specific spatial entropy
θ	The absolute temperature
γ	The masss specific spatial rate of entropy production
$\rho\mathcal{D}$	The spatial dissipation
$\rho\mathcal{D}_{loc}$	The spatial local dissipation
$\rho\mathcal{D}_{con}$	The spatial conductive dissipation
Ψ	The Helmholtz free energy
$\overline{\boldsymbol{\tau}}$	The total Kirchhoff stress tensor
$\boldsymbol{\tau}$	The mechanical Kirchhoff stress tensor
$\boldsymbol{\tau}^e$	The electrical Kirchhoff stress tensor
$\mathfrak{P}_{mec}$	The mechanical stress power per unit reference volume
$\mathfrak{P}_{elec}$	The electrical stress power per unit reference volume
$\overline{\boldsymbol{P}}$	The total first Piola-Kirchhoff stress tensor
$\overline{\boldsymbol{S}}$	The total second Piola-Kirchhoff stress tensor
Ψ^m	The mechanical part of the total Helmholtz free energy density function
Ψ^{em}	The electro-mechanical part of the total Helmholtz free energy density function

$\boldsymbol{c}$	The rigid body translation vector
$\boldsymbol{Q}$	The rigid body rotation vector
$\boldsymbol{F}_{vol}$	The volumetric (spherical) part of the deformation gradient
$\boldsymbol{F}_{iso}$	The isochoric (unimodular) part of the deformation gradient
$\boldsymbol{C}_{iso}$	The isochoric part of the right Cauchy-Green deformation tensor
$\boldsymbol{b}_{iso}$	The isochoric part of the left Cauchy-Green deformation tensor
U	The volumetric part of the mechanical free energy function
$\overline{\Psi}$	The isochoric part of the mechanical free energy function
$\boldsymbol{\tau}_{vol}$	The volumetric part of the total Kirchhoff stress tensor
$\boldsymbol{\tau}_{iso}$	The isochoric part of the total Kirchhoff stress tensor
$\boldsymbol{\tau}^{em}$	The electro-mechanical part of the total Kirchhoff stress tensor
$\tilde{\boldsymbol{d}}$	The electric displacement vector in the tangent space
$\mathbb{c}_{vol}$	The volumetric part of the mechanical moduli in the Eulerian configuration
$\mathbb{c}_{iso}$	The isochoric part of the mechanical moduli in the Eulerian configuration
$\mathbb{c}^{em}$	The electro-mechanical part of the mechanical moduli in the Eulerian configuration
$\mathbb{a}$	The third-order mixed moduli (electrical-mechanical mixed moduli)
$\mathbb{b}$	The third-order mixed moduli (mechanical-electrical mixed moduli)
$\mathbb{d}$	The second order electrical moduli
G^m	The mechanical part of the Galerkin functional
G^m_{int}	The internal mechanical part of the Galerkin functional
G^m_{ext}	The external mechanical part of the Galerkin functional
G^e	The electrical part of the Galerkin functional

G^e_{int}	The internal electrical part of the Galerkin functional
G^e_{ext}	The external electrical part of the Galerkin functional
Lin $(\bullet)$	The linearization operator
ΔG^{mm}_{mat}	The incremental form of the material part of the mechanical Galerkin functional
ΔG^{mm}_{geo}	The incremental form of the geometric part of the mechanical Galerkin functional
ΔG^{me}	The incremental form of the mechanical-electrical mixed part of the Galerkin functional
ΔG^{em}	The incremental form of the electrical-mechanical mixed part of the Galerkin functional
ΔG^{ee}	The incremental form of the electrical part of the Galerkin functional
$\mathcal{B}^e$	The body of the finite elements
N^A	The shape function belonging to Node A where $\forall A = 1, 2, \ldots, n$
$\partial_{Bx} N^A$	The gradient of the shape functions
$\boldsymbol{R}^m$	The mechanical part of the residual vector
$\boldsymbol{R}^e$	The electrical part of the residual vector
$\boldsymbol{K}^{mm}_{mat}$	The material part of the mechanical tangent matrix
$\boldsymbol{K}^{mm}_{geo}$	The geometric part of the mechanical tangent matrix
$\boldsymbol{K}^{me}$	The mechanical-electrical tangent matrix
$\boldsymbol{K}^{em}$	The electrical-mechanical tangent matrix
$\boldsymbol{K}^{ee}$	The electrical tangent matrix
$\boldsymbol{d}^m$	The solution vector for the mechanical part of the coupled electro-mechanical equation system
$\boldsymbol{d}^e$	The solution vector for the electrical part of the coupled electro-mechanical equation system
n_{el}	The total number of element

CHAPTER 1

INTRODUCTION

Computational modelling of Electro-Active Polymers (EAPs) whose microstructure possesses periodicity is investigated throughout this study. So as to examine the coupled electro-mechanical behavior of EAPs, the electro-mechanical coupling is described by the governing electrical and mechanical equations. Moreover, there are some materials whose microstructure consist of periodic or non-periodic heterogeneous cells. These heterogeneities consist mainly of voids or inclusions. The materials which have periodic cellular microstructures undergo pattern transformations under critical mechanical loads [6, 7]. However, there are limited, if any, number of studies existing in literature on the effects of electro-mechanical interaction on periodic microstructures when compared with the works about mechanical response of materials whose microstructure is periodically produced. Hence, in this introductory chapter, background information about the coupled electro-mechanical behavior of materials affected by the presence of electrical field is introduced after the motivation of this study is provided. Later, the overview on the deformation-induced transformations of periodic microstructures for entirely mechanical deformations is given. In each subsection, relavent studies are cited in order to highlight the originality of the current work.

1.1 Motivation and Problem Definition

After the industrial revolution in the late 18th or early 19th century, developments in technology have accelerated. The transition from manual production to the machines that fulfill the given tasks changed the lives of mankind. In this way, the problems

arising from manual production have started to decrease gradually. However, the use of these machines was still difficult at that time. Therefore, sensors and actuators have been developed to control the operating machines in time. These machine parts in charge of control should immediately check for errors in the production line and report on appropriate measures. However, the production of the sensors and actuators was expensive when compared with the other machine parts or tools. The materials that are able to react quickly and cost less to manufacture are still of great importance, even for today's technology. Luckily, today's technology and advancements in computer science allows us to produce computers with high computing power, allowing for the efficient analyses of complex multi-scale and multi-physics problems. The fact that complex problems can be solved has enabled researhers to conduct robust studies on the modeling of natural processes. One of the important problem type arising from the natural processes is the investigation of coupled material behavior.

Some materials have been produced such that one of the properties can be controlled by an externally applied stimulus. These materials are called as the smart materials. There are numerous types of smart materials developed. Shape memory alloys, electrostrictive elastomers, piezoelectric materials, ferroelectric materials, electro- and magneto-active polymers are some of the examples of smart materials that exhibit coupled material behavior [1, 2, 8, 9]. In these examples, electro- and magneto-active polymers are of importance as their mechanical responses is activated very quickly by electric and magnetic fields. These materials are relatively inexpensive, and return to their former shape when they are no longer subjected to electric or magnetic fields [2, 8, 9, 10, 11]. To make a more specific comparison, EAPs exhibit approximately two-fold more strain than electrostrictive piezoelectric ceramics. In addition, EAPs are said to have a faster response speed and less dense than shape memory alloys [2, 8]. Therefore, for the remainder of this chapter, the behavior of EAPs under the influence of an electric field will be examined and various important studies on EAPs will be overviewed.

All matters formed in nature are made up of atoms and molecules. When a material is examined at a molecular level, it is possible to see gaps or voids. When this is the case, approaches that assume that the materials are homogeneous may not yield accurate results. Therefore, the models that aim to describe the behavior of the material at the

macro level should take into account the heterogeneity at the micro level. There are many structures that show heterogeneity at the micro level in nature. These structures can be seen in butterflies, flies, bird wings, fish fins, and feet of various lizards and reptile species, as well as in various plant leaves such as water lily and lotus [3, 6]. For example, in Figure 1.1, the microstructural view of iridescent setae from polychaete worms at different length scales can be observed [3].

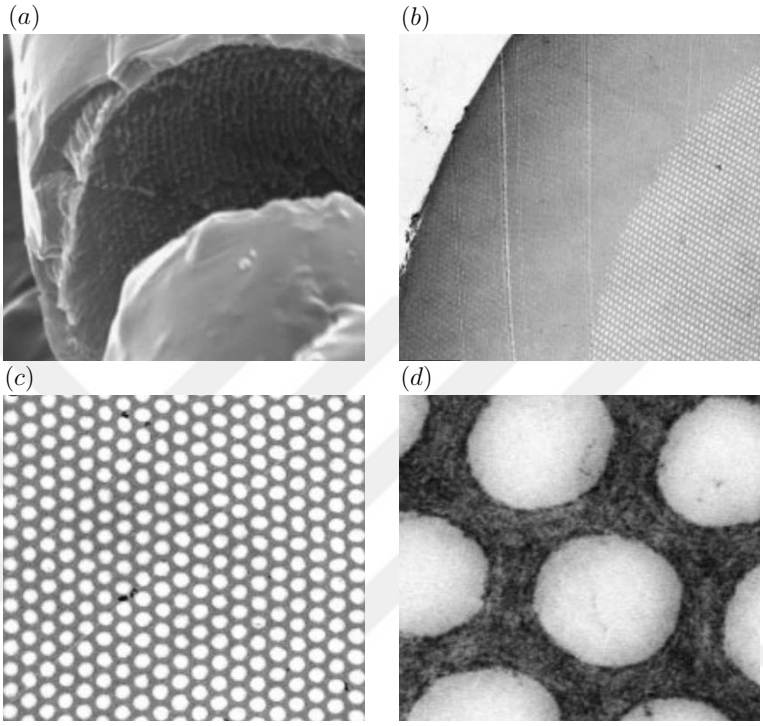

Figure 1.1: Scanning Electron Micrograph (SEM) views of iridescent setea from Polychaete worm [3] with (a) 2 μm, (b) 5 μm, (c) 1 μm, and (d) 120 nm.

When these structures are examined at micro and lower levels, it is observed that they have repetitive appearances. The materials whose microstructures possess repeated units are called periodic cellular solids [6]. Such solids that can be synthetically produced with inspiration from nature are used in various engineering fields such as mechanical, optical, and thermal. There are numerous studies investigating the behavior of periodic materials under mechanical effects [6, 7, 12, 13]. The mechanical effects are primarily compressive. Under compressive loads, the materials whose microstructures are made up of the unit cells with voids or inclusions exhibit local buckling between adjacent unit cells such that original periodicity may alter. How-

ever, there is a limited number of studies that deals with the pattern transformation due to coupled electro-mechanical effects. Consequently, the coupled electromechanical behavior of periodic microstructured solids under the influence of the electric field is a gap in the field to be filled.

1.2 Smart Material: Electro-Active Polymers

Electro-Active Polymers (EAPs) are electro-mechanically responsive polymeric or elastomeric materials that may deform whensubjected to an electric field. Because of their electrostrictive characteristic, EAPs are considered as smart materials, defined as materials whose one or more properties can be controlled and manipulated by an externally applied sources or stimuli. In the case of EAPs, external stimuli are the electric field and the deformations in the presence of the electric field are large. According to [1, 2, 8, 9, 14, 15, 16], EAPs as polymeric materials have many attractive properties such as mechanical flexibility, light weight, easy processing, fracture toughness, and many others.

EAPs are categorized into two forms depending upon the activation mechanisms either electronic (or field-ectivated) or ionic EAPs. The activation of electronic or field-activated EAPs is Coulombic attraction inside the elastomer. Hence, the response of this type of EAPs is fast. Moreover, the fact that electronic EAPs have a high energy density results in large deformation capacity. In order to generate large deformation, however, they require high activation field, i.e. electric field (> 100 kV/μm) [1, 2, 8, 9, 17, 18]. This is one of the drawbacks of these materials. There is a certain number of electronic EAPs. Ferroelectric polymers, dielectric EAPs, and electrostrictive graft elastomers are the most known types of electronic EAPs. In ferroelectric polymers, deformation occurs as a result of dipole vectors in polarized regions changing their sequence in the presence of electric field. However, this alignement is permanent. In other words, the polarized region remains aligned in the direction of the electric field even if the electric field is removed. To restore the polarized area to its previous configuration, an electric field must be applied in the reverse direction. However, hysteresis occurs due to the formation of permanently polarized sections [2, 19]. The dielectric elastomer or dielectric EAP, placed between two compliant

electrodes, is subjected to stress due to the Coulomb forces on electric charges when exposed to the electric field resulting from the given electrical potential differences on the two parallel electrodes. This stress is called the Maxwell stress, which generates compression in the dielectric elastomer in the direction of the electric field, while expansion occurs in the direction perpendicular to this field due to the Poisson effect [2, 9, 16, 20]. Unlike ferroelectric polymers, dielectric elastomers can return to their original position without exhibiting permanently polarized regions when the electric field is removed [2, 9, 11, 17]. Electrostrictive graft elastomers are a type of EAPs with more advanced properties produced at NASA Langley Research Center at 1999 [17]. Electrostrictive graft elastomers show a dispersed distribution within the polymer network. An electrostrictive graft elastomer consists of two parts: flexible graft chains and crystal graft units connected to two backbone chains. The crystal graft unit has polarized semiparticles or moieties. The torque generated in the presence of an electric field on the crystal graft units causes the flexible graft chains to rotate and the backbone chains approach each other, causing a shortening in the direction of the electric field and extending in the direction perpendicular to the electric field [2, 17]. Eventhough there are certain disadvantageous properties of electronic EAPs such as relatively low efficiency, low robustness, and large electric potential demand, electronic EAPs are widely employed in the production of sensors, actuators, robotics, biomimetics, and artificial muscles due to their fast response speed, exhibiting large and reversible deformations, and ease of produce [1, 8, 9, 14, 17]. On the other hand, in ionic EAPs, deformation of the material is determined by the diffusion of the ions of EAPs. Therefore, electromechanical response of this type is slow and actuation forces are lower than that of electronic EAPs. Moreover, they need an electrolytic environment for deformation. However, ionic EAPs need low electric potential as low as 1-2 V and the they deform more than electric EAPs [1, 2]. Ionic polymer gels and carbon nanotubes are two major examples of ionic EAPs. In ionic polymer gels, the gel changes the size and shape as a result of the electrical potential applied to the electrodes placed in an aqueous solution [2]. While the electrode-contacting gels are drawn near the anode, the gels expand near the anode if the electrode is not touched. The volume change of the ionic polymer gels is provided in the pioneering work of [21]. Moreover, experimental and theoretical study conducted by [22] focuses on bending type deformations of polymer gel. The widely used examples of the two

different types of EAP are given in Table 1.1 and more detailed information of each type can be found in [1, 2, 8, 9] and the references cited therein.

Table 1.1: The list of electronic and ionic EAPs [1, 2]

Electronic EAPs	Ionic EAPs
Ferroelectric Polymers	Ionic Polymer Gels
Dielectric EAPs	Carbon Nanotubes
Electrostrictive Graft Elastomer	Ionic Polymer Metal Composite
Electrostrictive Paper	Conducting Polymer
Electro-viscoelestic Elastomer	

The coupled electromechanical effects can be traced back to the Wilhelm Röntgen's experiments with rubber strips. As a result of the deformation of rubber strips exposed to the electric field, studies on electromechanics have started. The theoretical studies and the fundamental information on the coupled electromechanical behavior of dielectric elastomers are based on the pioneering work [23, 24, 25]. In [23], fundamental information of electrostatics, electro-mechanical field equations, and boundary conditions for dielectric elastomers, especially for isotropic dielectric elastomers, are expressed to form a basis. Maxwell's continuum theory of electricity and magnetism and free energy function related with the theory are investigated in [24]. In addition, the nonlinear continuum theory of electromechanical and magnetomechanical interactions are reviewed in [26]. Likewise, the electromechanical continuum theory is examined in [9, 15]. Considering the incompressible nature of the dielectric elastomers, the four-field FEM is used [9, 10, 27]. The four-field FEM, which was previously investigated considering mechanical effects [28, 29], has been developed for the coupled electromechanical interactions. The work in [30] concentrates on the numerical modelling of nonlinear behavior of continuum electro-mechanical coupled system of equations. In order to solve the governing equations of nonlinear electroelasticity, the finite element formulations for both Lagrangian (or reference) and Eulerian (or current) configuration are proposed. To evaluate the robustness of the model, the finite element model is compared with the analytic solutions obtained

from differential equation's solver. In many cases, surrounding environment affects the deformation of the body. The effect of surronding environment on the deformation of electronic EAPs is investigated by [31, 32]. They employ the coupled Boundary Element Method and Finite Element Method (BEM-FEM) such that FEM is used for the material body and BEM is used to simulate the finite or infinite free space surrounding the body of interest. Furthermore, numerical results which are obtained from BEM-FEM approach are compared with only FEM approach. Numerical investigations emphasize that surrounding environment has a significant effect on the deformation of the body. One dimensional electromechanical constitutive equations for electronic EAPs is extended to the three dimensional continuum setting by the micro-sphere formulation in [33]. The phenomenological constitutive modelling of electroviscoelastic coupling in electrostrictive polyurethane which is generally employed for actuators is evaluated in [18, 34]. The inverse motion problem is solved for the coupled electromechanical equations to find a more suitable design of EAPs in [35]. By this way, with the prescribed conditions, the optimal initial state can be predicted. The four-field FEM is again used for the inverse motion problem due to the incompressible nature of EAPs.

1.3 Pattern Transformation of Solids

Humankind have always aimed to simplify their lives by imitating what is in nature. There are certain number of materials which exhibit periodic microstructures frequently found in nature. In order to use these materials in engineering applications, the structural and material stability analyses are combined. The mechanical instability of periodic microstructures under mechanical deformations has been investigated in the studies [6, 7, 13, 36, 37, 38]. In these studies, elastic instability, that is, local buckling in the microstructure which consists of cellular solids with voids, occurs due to compression. As a result of local buckling, the initial pattern transforms into a new pattern such that initial periodicity is broken and a new pattern with different periodicity occurance is establihed. The smallest cell of the microstructure that repeats itself is called a unit cell. Furthermore, different cell types are examined numerically and experimentally [6, 13, 36, 37, 39]. For experimental and numerical investigations,

square cells with circular voids, rectangular cells with elliptic voids, and oblique cells with circular voids are employed in [6] and different void shapes with square cells are analyzed in [37, 39]. In [6], the stability analysis of the model whose dimensions are the same as the sample prepared for the experiment is performed in two ways. These two methods are Refined Eigen Analysis (REA) and the Bloch-Floquet wave analysis. Before any loading is applied onto the microstructure, periodicity is provided for a single cell. When the micrsoctructure is loaded, the initial periodicity may change at some load level which is called as critical loading and the initial periodicity consisting many unit cells may be formed. However, it is unknown how many cells the new periodicity would involve. Hence, all possible configurations can be numerically tested using REA and the configuration with the smallest critical loading causes pattern transformation with a new periodicity. This procedure is called as REA [6, 40]. The Bloch-Floquet method is the other approach to detect the critical load that local instability (local buckling) starts. In this method, the Bloch-Floquet periodic boundary conditions are applied on the unit cell [6, 27, 40, 41]. With these boundary conditions, the information for enlarged unit cells is imposed on the unit cell. Within the finite element framework, when the smallest eigenvalue of the consistent tangent matrix becomes zero; that is, when the consistent tangent matrix becomes singular, the critical load is found. Since the Bloch-Floquet wave analysis requires complex numbers, FEM is designed to be compatible with the Bloch-Floquet wave analysis. To do so, equilibrium equations are split into uncoupled real and imaginary parts [6, 27, 40, 42]. Hence, the consistent tangent matrix and the residual vectors are formed and manipulated with the Bloch-Floquet boundary conditions. It must be stated that Bloch-Floquet wave analysis is applied to detect the critical compressive loading. When the critical eigenvalue and associated eigenvector is found by the Bloch-Floquet wave analysis, the finite and infinite sized specimens can be perturbed by the eigen solutions to obtain the deformed shape.

Besides, to detect and solve structural instabilities for heterogeneous materials, computational homogenization analysis should be performed. The computational procedures for micro-macro transition of heterogeneous materials are provided for small deformations in [43] and for finite deformations [44, 45].

1.4 Challenges

Many analyses and investigations were tried during the preparation of the thesis. Nevertheless, some of them were concluded. These are the four-field FEM with coupled electromechanics, the FEM with coupled electromechanics, and the stability analyses with the Refined Eigen Analysis (REA) for pattern transformations under only mechanical effects. Moreover, these examples were combined to simulate the pattern transformations of EAPs under coupled electromechanical loading scenarios. In order to predict and obtain post-deformed shape of the periodically produced cellular structure, Bloch-Floquet wave analyses were tried along with the two-scale computational homogenization algorithm at finite deformations. However, quadratic convergence of the solution algorithm has not been fulfilled yet. Therefore, micro-macro transition together with the Bloch-Floquet wave analysis will be investigated in the future work.

1.5 Contributions and Novelties

In this study, stability analyses of periodically structured EAPs under coupled electromechanical effects were performed. This study is a combination of two previously mentioned sections. In order to perform stability analyzes under coupled electromechanical effects, both the coupled electromechanical analysis of EAPs in the presence of electric field, and the geometric stability analyzes of the structure consisting of periodic unit cells with circular voids were carried out separately. Although there are studies in the literature on the effects of coupled electromechanical effects on composite materials, no studies exist on the stability of the microstructures that have periodic unit cells with circular voids under electromechanically coupled effect.

1.6 The Outline of the Thesis

In Chapter 2, the fundamentals of non-linear continuum mechanics and the laws of electrostatics are presented to obtain the coupled electro-mechanical equations for EAPs. The governing differential equations are formulated at large strains since the electro-mechanical interaction results in finite deformations. Hence, the chapter be-

gins with the fundamentals of continuum mechanics. Next, it continues with the laws of continuum electrostatics. The expressions are combined to obtain a coupled electromechanical equation system for EAPs.

In Chapter 3, three hyperelastic material models are presented, two of which is introduced for the coupled electro-mechanical investigations and one for the pattern transformation under purely mechanical effects. One of the electromechanical hyperelastic models is provided considering the incompressible nature of EAPs whereas the other is a phenomenological model which is concerned with compressible behavior of EAPs. In instablity analyses, two term I_1-based Mooney-Rivlin material model is employed.

Chapter 4 is devoted to the finite element discretization of the coupled electro-mechanical equations. At first, the preliminary equations of electromechanical equations with prescribed boundary conditions are recalled. Then, the weak form of electromechanically coupled equations is discretized. Within the iterative solution procedure of the Newton method, the non-linear residual vectors are linearized to obtain the electromechanical solution vectors.

Chapter 5 is concerned with the respresentative numerical analyses where the convergence analyzes are performed to ensure the validity of the generated models for understanding the coupled electro-mechanical behavior of EAPs and assuring the stability analysis of periodic microstructural materials. Moreover, by combining these models, which are assured for their accuracy, the effect of coupled electro-mechanical effects on materials possessing periodic microstructure is investigated.

Finally, in Chapter 6, conclusion drawn from the validated and generated models for EAPs with periodic microstructures are given.

CHAPTER 2

FUNDAMENTALS OF CONTINUUM MECHANICS AND ELECTROSTATICS

This chapter outlines the fundamental equations of non-linear continuum mechanics and electrostatics in large deformations, which constitute the basis of coupled electro-mechanical equations. Finite strain continuum mechanics provides mappings between geometric settings, stress expressions for each settings, and transformations between stress and deformation-related quantities. The balance equations of solids undergoing finite deformations are also provided in this chapter. In addition to non-linear continuum mechanics, continuum electrostatics is introduced. The fundamental laws of electrostatics, such as Coulomb's law, Gauss's law, Faraday's law, and Maxwell's equations are presented in the forthcoming subsections. Furthermore, the transformations of electrostatic equations between reference and current states are established. Finally, electrical equations from electrostatics are combined with mechanical equations to form a system of coupled electro-mechanical equations.

2.1 Fundamentals of Continuum Mechanics

In this section, the fundamental equations of continuum mechanics that form the basis for the rest of the thesis are given. For this purpose, various references are cited and the information required for the mechanical part of the associated electro-mechanical expressions is presented. For more detailed information, the reader is referred to [9, 26, 29, 46, 47] and the references cited therein.

2.1.1 The Motion of a Material Body and Deformation Measures

Being different from atomistic and molecular theories, a *continuum* or a *material body*, denoted as B, possess infinitely many *material points*, one of which is denoted as $P \in B$ in Figure 2.1. The material point P is identified in the three dimensional Euclidean space, $\mathbb{R}^3$. When a continuum body B moves, it occupies different regions in Euclidean space $\mathbb{R}^3$ at any instant of time $t \in \mathbb{R}_+$, which is defined as the configuration of the material body and it is characterized by $\boldsymbol{\chi}_t$ as

$$\boldsymbol{\chi} : \begin{cases} B \to \mathcal{B} \subset \mathbb{R}^3 \,, \\ P \in B \mapsto \boldsymbol{X} = \boldsymbol{\chi}_{t_0}(P) \in \mathcal{B} \,. \end{cases} \tag{2.1}$$

Reference state involves the placement of a solid body at a reference time t_0, and it generally refers to the stress-free configuration of a body. Hence, the reference state can be defined as the configuration of the body at time t_0 or $\mathcal{B} \equiv \boldsymbol{\chi}_{t_0}(B)$. Similarly, $\mathcal{S} \equiv \boldsymbol{\chi}_t(B)$ is the configuration of the body at current time $t > t_0$. The position vector of a *material point P* at reference state can be denoted as $\boldsymbol{X} \in \mathcal{B}$. Likewise, at current time t, spatial coordinates can be identified with the spatial position vector, $\boldsymbol{x} \in \mathcal{S}$, depicted in Figure 2.1. The position vectors at reference and spatial configuration can be decomposed into components and their basis such that position vector at reference state can be defined as $\boldsymbol{X} = X^I \boldsymbol{E}_I$ for $I = 1, 2, 3$. As in the case of the position vector at the reference state, the spatial position vector can also be decomposed as $\boldsymbol{x} = x^i \, \boldsymbol{e}_i$ for $i = 1, 2, 3$. It is important to note that upper case indices is employed for Lagrangian state vectors or tensors in indicial notation, whereas lower case letters is used for Eulerian counterparts. In addition, $\boldsymbol{E}_I$ and $\boldsymbol{e}_i$ are basis vectors for Lagrangian and Eulerian configurations, respectively.

As one of the most fundamental representations in finite strain continuum mechanics, the non-linear deformation map $\boldsymbol{\varphi}_t(\boldsymbol{X})$ describes the motion of a solid body from initial (reference, Lagrangian) configuration ($\boldsymbol{\chi}_{t_0}(B)$) to the current (spatial, Eulerian) configuration ($\boldsymbol{\chi}_t(B)$).

$$\boldsymbol{\varphi}_t(\boldsymbol{X}) : \begin{cases} \mathcal{B} \to \mathcal{S} = \boldsymbol{\varphi}_t(\mathcal{B}) \,, \\ \boldsymbol{X} \mapsto \boldsymbol{x} = \boldsymbol{\varphi}(\boldsymbol{X}, t) := \boldsymbol{\chi}_t \circ \boldsymbol{\chi}_{t_0}^{-1}(\boldsymbol{X}) \,. \end{cases} \tag{2.2}$$

The non-linear deformation map $\boldsymbol{\varphi}_t(\boldsymbol{X})$ is *one-to-one* and *bijective*. Consequently,

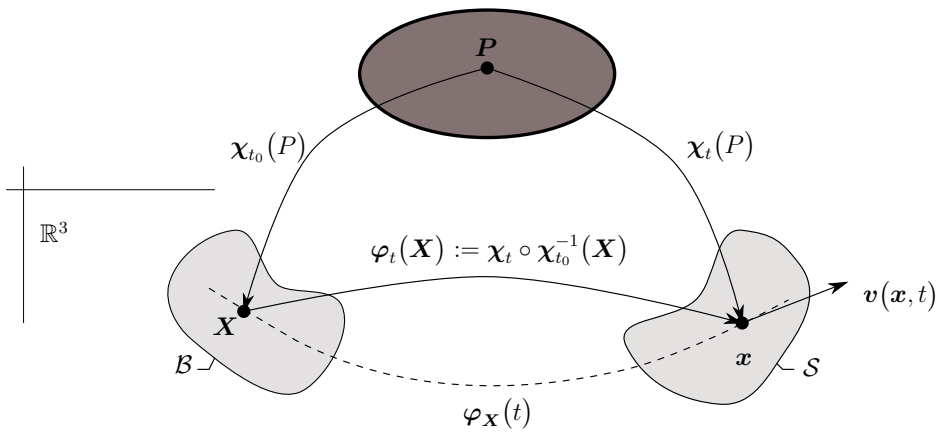

Figure 2.1: The motion of a solid body in time $t \in \mathbb{R}_+$.

the inverse of the deformation map can be obtained uniquely as

$$\boldsymbol{\varphi}_t^{-1}(\boldsymbol{x}) : \begin{cases} \mathcal{S} \to \mathcal{B}\,, \\ \boldsymbol{x} \mapsto \boldsymbol{X} = \boldsymbol{\varphi}^{-1}(\boldsymbol{x},t) := \boldsymbol{\chi}_{t_0} \circ \boldsymbol{\chi}_t^{-1}(\boldsymbol{x})\,. \end{cases} \tag{2.3}$$

At any instant of time $t \in \mathbb{R}_+$, the non-linear deformation map states the corresponding configuration of a material point. At that instant of time, *the material velocity* $\boldsymbol{V}\big(\boldsymbol{X},t\big) \in T_x\mathcal{S}$, which is parametrized by the material point $\boldsymbol{X}$, can be determined by the time rate of change of its configuration.

$$\boldsymbol{V}\big(\boldsymbol{X},t\big) := \frac{\partial}{\partial t}\boldsymbol{\varphi}\big(\boldsymbol{X},t\big) = \frac{d}{dt}\boldsymbol{\varphi}_{\boldsymbol{X}}\big(t\big)\,. \tag{2.4}$$

Likewise, *the material acceleration*, $\boldsymbol{A}\big(\boldsymbol{X},t\big) \in T_x\mathcal{S}$ can be determined by

$$\boldsymbol{A}\big(\boldsymbol{X},t\big) := \frac{\partial}{\partial t}\boldsymbol{V}\big(\boldsymbol{X},t\big) = \frac{d}{dt}\boldsymbol{V}_{\boldsymbol{X}}\big(t\big)\,. \tag{2.5}$$

It should be emphasized that $\boldsymbol{V}\big(\boldsymbol{X},t\big)$ and $\boldsymbol{A}\big(\boldsymbol{X},t\big)$ are vector fields and they belong to the tangent space of the current configuration $T_x\mathcal{S}$. When the material velocity and acceleration are expressed in terms of spatial coordinates $\boldsymbol{x}$, they are called *the spatial velocity*, $\boldsymbol{v}\big(\boldsymbol{x},t\big) \in T_x\mathcal{S}$, and *the spatial acceleration*, $\boldsymbol{a}\big(\boldsymbol{x},t\big) \in T_x\mathcal{S}$, respectively. They can be obtained as

$$\begin{aligned} \boldsymbol{v}\big(\boldsymbol{x},t\big) &:= \boldsymbol{V}\big(\boldsymbol{\varphi}_t^{-1}(\boldsymbol{x}),t\big) = \boldsymbol{V}_t\big(\boldsymbol{X}\big) \circ \boldsymbol{\varphi}_t^{-1}\big(\boldsymbol{x}\big)\,, \\ \boldsymbol{a}\big(\boldsymbol{x},t\big) &:= \boldsymbol{A}\big(\boldsymbol{\varphi}_t^{-1}(\boldsymbol{x}),t\big) = \boldsymbol{A}_t\big(\boldsymbol{X}\big) \circ \boldsymbol{\varphi}_t^{-1}\big(\boldsymbol{x}\big)\,. \end{aligned} \tag{2.6}$$

The so-called *deformation gradient* $\boldsymbol{F}$ transforms or maps a tangent vector in the reference configuration $\boldsymbol{T} \in T_X\mathcal{B}$ into the vector in the current configuration $\boldsymbol{t} \in T_x\mathcal{S}$ as depicted in Figure 2.2.

$$\boldsymbol{F} : \begin{cases} T_X\mathcal{B} \to T_x\mathcal{S}\,, \\ \boldsymbol{T} \mapsto \boldsymbol{t} = \boldsymbol{F}\boldsymbol{T}\,, \end{cases} \tag{2.7}$$

where $T_X\mathcal{B}$ and $T_x\mathcal{S}$ are the tangent spaces of the reference and current settings, respectively.

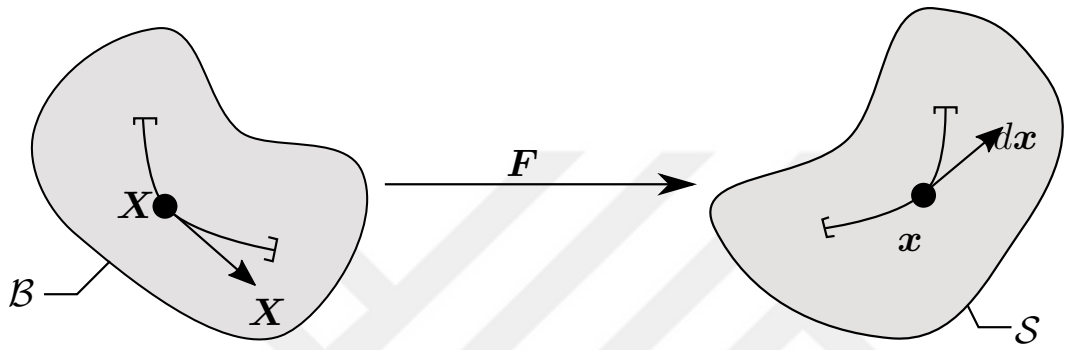

Figure 2.2: The *deformation gradient*, $\boldsymbol{F}$, transforms tangential vector $d\boldsymbol{X} \in T_X\mathcal{B}$ in reference configuration into its counterpart in current configuration $d\boldsymbol{x} \in T_x\mathcal{S}$ by $d\boldsymbol{x} := \boldsymbol{F}d\boldsymbol{X}$.

As a consequence, deformation gradient is called *the tangent map* that can also be defined as the Fréchet derivative of the non-linear deformation map with respect to material coordinates $\boldsymbol{X}$.

$$\boldsymbol{F}(\boldsymbol{X}) = \nabla_{\boldsymbol{X}}\boldsymbol{\varphi}(\boldsymbol{X}, t)\,. \tag{2.8}$$

Deformation gradient tensor can be denoted as $F^i_I := \frac{\partial \varphi^i}{\partial X^I}$ in indicial notation with $t^i = F^i_I\, T^I$.

One of the most important constraint in kinematics is *the Jacobian*, or *volume map* such that $J := \det\left[\boldsymbol{F}\right] > 0$ to eliminate penetration of the material points. *The Jacobian* can be found by the relation between the infinitesimal volume element in the initial configuration dV and that in the current configuration dv. Infinitesimal volume elements dV and dv can be defined as the scalar triple products of tangent

vectors $d\boldsymbol{X}^{I=1,2,3} \in T_X\mathcal{B}$ and $d\boldsymbol{x}^{i=1,2,3} \in T_x\mathcal{S}$, i.e.

$$\begin{aligned} dV &= d\boldsymbol{X}^1 \cdot \left(d\boldsymbol{X}^2 \times d\boldsymbol{X}^3\right), \\ dv &= d\boldsymbol{x}^1 \cdot \left(d\boldsymbol{x}^2 \times d\boldsymbol{x}^3\right). \end{aligned} \tag{2.9}$$

Employing relation (2.9), *the Jacobian* can be obtained as:

$$dv = \left(\boldsymbol{F}d\boldsymbol{X}^1\right) \cdot \left(\left(\boldsymbol{F}d\boldsymbol{X}^2\right) \times \left(\boldsymbol{F}d\boldsymbol{X}^3\right)\right) = \det \boldsymbol{F}dV := JdV\,. \tag{2.10}$$

The representation of *volume map* can be described as:

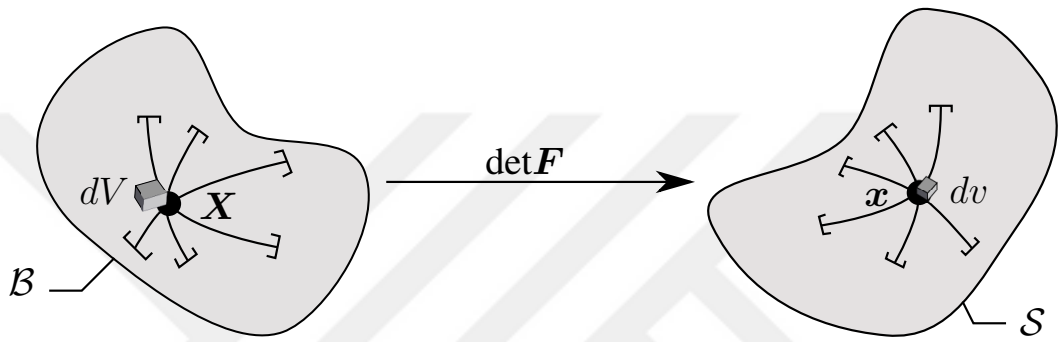

Figure 2.3: The *volume map* ($J := \det\boldsymbol{F}$) maps infinitesimal volume element dV in reference configuration into the infinitesimal volume element in current configuration dv by $dv := JdV$.

Therefore, *the Jacobian* maps the infinitesimal volume element in the reference configuration into its counterpart in the current configuration.

$$J = \det \boldsymbol{F} : \begin{cases} \mathbb{R}_+ \to \mathbb{R}_+\,, \\ dV \mapsto dv = JdV\,. \end{cases} \tag{2.11}$$

While *the deformation gradient*, $\boldsymbol{F}$ maps the tangent vectors and *the Jacobian J* maps the volume elements, *the normal map* transforms the area element in the reference configuration into its counterpart in the spatial configuration employing *Nanson's formula*, i.e. $\boldsymbol{n}\,da := \operatorname{cof}\left[\boldsymbol{F}\right]\boldsymbol{N}\,dA$ where $\operatorname{cof}\left[\boldsymbol{F}\right] := J\,\boldsymbol{F}^{-T}$. This equivalance can be found by using the geometrical meaning of the area element. Vector or cross product of two infinitesimal vector elements presents an vectorial area which is spanned

by these vectors and its normal vector.

$$\begin{aligned} \boldsymbol{N}dA &= d\boldsymbol{X}^2 \times d\boldsymbol{X}^3 \,, \\ \boldsymbol{n}da &= d\boldsymbol{x}^2 \times d\boldsymbol{x}^3 \,. \end{aligned} \tag{2.12}$$

Since $d\boldsymbol{x}^1 \cdot \boldsymbol{n}da = dv = JdV$, the above equation becomes:

$$\begin{aligned} \left(\boldsymbol{F}d\boldsymbol{X}^1\right) \cdot \boldsymbol{n}da &= Jd\boldsymbol{X}^1 \cdot \left(d\boldsymbol{X}^2 \times d\boldsymbol{X}^3\right) , \\ \left(\boldsymbol{F}d\boldsymbol{X}^1\right) \cdot \boldsymbol{n}da &= Jd\boldsymbol{X}^1 \cdot \boldsymbol{N}dA \,, \\ \left(d\boldsymbol{X}^1\boldsymbol{F}^T\right) \cdot \boldsymbol{n}da &= d\boldsymbol{X}^1 \cdot J\boldsymbol{N}dA \quad \text{for any} \quad d\boldsymbol{X}_1 \neq \boldsymbol{0} \,, \\ \boldsymbol{F}^T \cdot \boldsymbol{n}da &= J\boldsymbol{N}dA \,, \\ \boldsymbol{n}da &= J\boldsymbol{F}^{-T}\boldsymbol{N}dA := \operatorname{cof}\left[\boldsymbol{F}\right]\boldsymbol{N}dA \,. \end{aligned} \tag{2.13}$$

Hence, *the normal map*, $\boldsymbol{F}^{-T}$, maps the normal of a surface in the reference configuration into the surface normal in the current configuration. *The normal map* can then be defined as:

$$\boldsymbol{F}^{-T} : \begin{cases} T^*_X\mathcal{B} \to T^*_x\mathcal{S} \,, \\ \boldsymbol{N} \mapsto \boldsymbol{n} = \boldsymbol{F}^{-T}\boldsymbol{N} \,, \end{cases} \tag{2.14}$$

where $T^*_X\mathcal{B}$ and $T^*_x\mathcal{S}$ are the co-tangent (normal) spaces for reference and current settings, respectively. Normal map can be portrayed as in Figure 2.4.

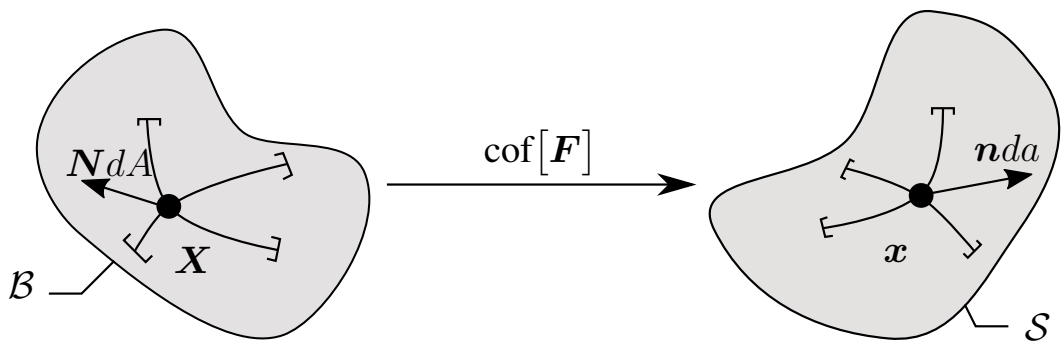

Figure 2.4: The *normal map* ($\operatorname{cof}\left[\boldsymbol{F}\right]$) transforms normal vector $\boldsymbol{N}dA \in T^*_X\mathcal{B}$ in reference configuration into its counterpart in current configuration $\boldsymbol{n}da \in T^*_x\mathcal{S}$ by $\boldsymbol{n}da := \operatorname{cof}\left[\boldsymbol{F}\right]\boldsymbol{N}dA$.

Moreover, inverse of the deformation gradient tensor can be represented as $\left(\boldsymbol{F}^{-1}\right)^I_i := \frac{\partial X^I}{\partial x^i}$ with $n_i = \left(F^{-1}\right)^I_i N_I$.

All these tensors can be evaluated by using a curvilinear coordinate system rather than using the Cartesian coordinate system. In that case, metric tensors must be introduced such that $\boldsymbol{G} = G_{IJ}$ and $\boldsymbol{g} = g_{ij}$ are the co-variant reference and spatial metrics, respectively. The co-variant reference metric $\boldsymbol{G}$ maps a vector in the tangent space into a normal in the co-tangent space as

$$\boldsymbol{T}^{\flat} = \boldsymbol{G}\boldsymbol{T}, \qquad \text{where} \quad T_I = G_{IJ}T^J \,. \tag{2.15}$$

In a similar manner, the co-variant metric in the current configuration, i.e. $\boldsymbol{g}$, maps a vector in the tangent space into a normal in the co-tangent space as

$$\boldsymbol{t}^{\flat} = \boldsymbol{g}\boldsymbol{t}, \qquad \text{where} \quad t_i = g_{ij}t^j \,. \tag{2.16}$$

Thus, the co-variant reference metric $\boldsymbol{G}$ and the current metric $\boldsymbol{g}$ can be defined as

$$\begin{aligned} \boldsymbol{G} &: T_X\mathcal{B} \to T_X^*\mathcal{B} \,, \\ \boldsymbol{g} &: T_x\mathcal{S} \to T_x^*\mathcal{S} \,. \end{aligned} \tag{2.17}$$

Analogously, the inverse of the co-variant metric tensors can be defined as

$$\begin{aligned} \boldsymbol{T} &= \boldsymbol{G}^{-1}\boldsymbol{T}^{\flat}, \qquad \text{where} \quad T^I = \left(G^{-1}\right)^{IJ} T_J \,, \\ \boldsymbol{t} &= \boldsymbol{g}^{-1}\boldsymbol{t}^{\flat}, \qquad \text{where} \quad t^i = \left(g^{-1}\right)^{ij} t_j \,. \end{aligned} \tag{2.18}$$

Metric tensors become *Kronecker's delta*, when they are used in the Cartesian coordinate system such as $G_{IJ} = \delta_{IJ}$ and $g_{ij} = \delta_{ij}$. In fact, *Kronecker's deltas* are defined as $\delta^I_{\ J}$ in the reference configuration and $\delta^i_{\ j}$ in the current configuration. However, in order to satisfy either an index raising or lowering operation for metric tensors, *Kronecker's deltas* are defined as either a fully index raised case or a lowered case. Additionally, it must be emphasized that metric tensors are both positive definite tensors. In Cartesian coordinate system, they are defined as:

$$G_{IJ} : \begin{cases} 1, & \text{if} \quad I = J \,, \\ 0, & \text{if} \quad I \neq J \,. \end{cases} \qquad\qquad g_{ij} : \begin{cases} 1, & \text{if} \quad i = j \,, \\ 0, & \text{if} \quad i \neq j \,. \end{cases} \tag{2.19}$$

2.1.2 Cauchy-Green Tensors

For a given deformation, the Lagrangian vector $\boldsymbol{T}\left(\boldsymbol{X}\right) \in T_X\mathcal{B}$, whose length can be denoted as $\mid \boldsymbol{T} \mid_{\boldsymbol{G}} = \sqrt{\boldsymbol{T} \cdot \boldsymbol{G}\boldsymbol{T}}$ becomes an Eulerian vector $\boldsymbol{t} = \boldsymbol{F}\boldsymbol{T} \in T_x\mathcal{S}$, whose

length can be determined by $\mid \boldsymbol{t} \mid_{\boldsymbol{g}} = \sqrt{\boldsymbol{t} \cdot \boldsymbol{g}\boldsymbol{t}}$. If the length of the Lagrangian vector $\boldsymbol{T}$ is taken as unity, $\mid \boldsymbol{T} \mid_{\boldsymbol{G}} = 1$, the ratio of the length of the Eulerian vector to that its the Lagrangian counterpart will give *the stretch*, λ. Using this definition, *the stretch* can be found by

$$\begin{aligned}
\lambda := \frac{\mid \boldsymbol{t} \mid_{\boldsymbol{g}}}{\mid \boldsymbol{T} \mid_{\boldsymbol{G}}} &= \frac{\sqrt{\boldsymbol{t} \cdot \boldsymbol{g}\boldsymbol{t}}}{\sqrt{\boldsymbol{T} \cdot \boldsymbol{G}\boldsymbol{T}}} \\
&= \frac{\sqrt{(\boldsymbol{F}\boldsymbol{T}) \cdot (\boldsymbol{g}\boldsymbol{F}\boldsymbol{T})}}{\sqrt{\boldsymbol{T} \cdot \boldsymbol{G}\boldsymbol{T}}} \quad \text{for} \quad \mid \boldsymbol{T} \mid_{\boldsymbol{G}} = 1 \\
&= \sqrt{\boldsymbol{T} \cdot (\boldsymbol{F}^T \boldsymbol{g} \boldsymbol{F})\boldsymbol{T}} \\
&= \sqrt{\boldsymbol{T} \cdot \boldsymbol{C}\boldsymbol{T}} \\
&=: \mid \boldsymbol{T} \mid_{\boldsymbol{C}} ,
\end{aligned} \tag{2.20}$$

where $\boldsymbol{C}$ is *the right Cauchy-Green tensor* and it is defined by

$$\boldsymbol{C} := \boldsymbol{\varphi}^*(\boldsymbol{g}) = \boldsymbol{F}^T \boldsymbol{g} \boldsymbol{F} , \tag{2.21}$$

The right Cauchy-Green tensor is the *pull-back* of the spatial metric tensor and pull-back operation can be denoted by $\boldsymbol{\varphi}^*$ operator. If the length of the Eulerian vector is taken as unity, using the expression $\boldsymbol{T} = \boldsymbol{F}^{-1}\boldsymbol{t} \in T_X\mathcal{B}$ inverse of the stretch can be defined as:

$$\begin{aligned}
\lambda^{-1} := \frac{\mid \boldsymbol{T} \mid_{\boldsymbol{G}}}{\mid \boldsymbol{t} \mid_{\boldsymbol{G}}} &= \frac{\sqrt{\boldsymbol{T} \cdot \boldsymbol{G}\boldsymbol{T}}}{\sqrt{\boldsymbol{t} \cdot \boldsymbol{g}\boldsymbol{t}}} \\
&= \frac{\sqrt{(\boldsymbol{F}^{-1}\boldsymbol{t}) \cdot \boldsymbol{G}(\boldsymbol{F}^{-1}\boldsymbol{t})}}{\sqrt{\boldsymbol{t} \cdot \boldsymbol{g}\boldsymbol{t}}} \\
&= \sqrt{\boldsymbol{t} \cdot (\boldsymbol{F}^{-T} \boldsymbol{G} \boldsymbol{F}^{-1})\boldsymbol{t}} \\
&= \sqrt{\boldsymbol{t} \cdot \boldsymbol{c}\boldsymbol{t}} \\
&=: \mid \boldsymbol{t} \mid_{\boldsymbol{c}} ,
\end{aligned} \tag{2.22}$$

where $\boldsymbol{c}$ is the inverse of the *left Cauchy-Green* tensor, $\boldsymbol{b}$. The inverse of the left Cauchy-Green tensor is the *push-forward* of the Lagrangian metric $\boldsymbol{G}$ and can be defined as

$$\boldsymbol{c} := \boldsymbol{\varphi}_*(\boldsymbol{G}) = \boldsymbol{F}^{-T} \boldsymbol{G} \boldsymbol{F}^{-1} , \tag{2.23}$$

where $\boldsymbol{\varphi}_*$ is the push-forward operator. Analogously, the Lagrangian normal vector $\boldsymbol{N}(\boldsymbol{X}) \in T_X^*\mathcal{B}$ becomes the Eulerian normal vector $\boldsymbol{n}(\boldsymbol{x}) \in T_X^*\mathcal{S}$ by the normal map

$\boldsymbol{n} := \boldsymbol{F}^{-T}\boldsymbol{N}$. Since stretch is defined as the ratio of the length of the Eulerian object to its Lagrangian counterpart, *the area stretch*, which is defined as ν, is the ratio of the area of an Eulerian object, $\mid \boldsymbol{n} \mid_{\boldsymbol{g}^{-1}}$, to the area of a Lagrangian object, $\mid \boldsymbol{N} \mid_{\boldsymbol{G}^{-1}}$. If $\mid \boldsymbol{N} \mid_{\boldsymbol{G}^{-1}} = 1$, then area stretch can be found by:

$$\begin{aligned}
\nu := \frac{\mid \boldsymbol{n} \mid_{\boldsymbol{g}^{-1}}}{\mid \boldsymbol{N} \mid_{\boldsymbol{G}^{-1}}} &= \frac{\sqrt{\boldsymbol{n} \cdot \boldsymbol{g}^{-1}\boldsymbol{n}}}{\sqrt{\boldsymbol{N} \cdot \boldsymbol{G}^{-1}\boldsymbol{N}}} \\
&= \frac{\sqrt{\left(\boldsymbol{F}^{-T}\boldsymbol{N}\right) \cdot \boldsymbol{g}^{-1}\left(\boldsymbol{F}^{-T}\boldsymbol{N}\right)}}{\sqrt{\boldsymbol{N} \cdot \boldsymbol{G}^{-1}\boldsymbol{N}}} \\
&= \sqrt{\boldsymbol{N} \cdot \left(\boldsymbol{F}^{-1}\boldsymbol{g}^{-1}\boldsymbol{F}^{-T}\right)\boldsymbol{N}} \\
&= \sqrt{\boldsymbol{N} \cdot \boldsymbol{C}^{-1}\boldsymbol{N}} \\
&=: \mid \boldsymbol{N} \mid_{\boldsymbol{C}^{-1}},
\end{aligned} \tag{2.24}$$

where $\boldsymbol{C}^{-1}$ is the inverse of the right Cauchy-Green tensor. Moreover, it is the pull-back of inverse of the Eulerian metric tensor; that is,

$$\boldsymbol{C}^{-1} := \boldsymbol{\varphi}^*\left(\boldsymbol{g}^{-1}\right) = \boldsymbol{F}^{-1}\boldsymbol{g}^{-1}\boldsymbol{F}^{-T}. \tag{2.25}$$

In the spatial description, for the inverse of the area stretch, $\mid \boldsymbol{n} \mid_{\boldsymbol{g}^{-1}} = 1$ is specified using $\boldsymbol{N} := \boldsymbol{F}^T\boldsymbol{n} \in T^*_X\mathcal{B}$

$$\begin{aligned}
\nu^{-1} := \frac{\mid \boldsymbol{N} \mid_{\boldsymbol{G}^{-1}}}{\mid \boldsymbol{n} \mid_{\boldsymbol{g}^{-1}}} &= \frac{\sqrt{\boldsymbol{N} \cdot \boldsymbol{G}^{-1}\boldsymbol{N}}}{\sqrt{\boldsymbol{n} \cdot \boldsymbol{g}^{-1}\boldsymbol{n}}} \\
&= \frac{\sqrt{\left(\boldsymbol{F}^T\boldsymbol{n}\right) \cdot \boldsymbol{G}^{-1}\left(\boldsymbol{F}^T\boldsymbol{n}\right)}}{\sqrt{\boldsymbol{n} \cdot \boldsymbol{g}^{-1}\boldsymbol{n}}} \\
&= \sqrt{\boldsymbol{n} \cdot \left(\boldsymbol{F}\boldsymbol{G}^{-1}\boldsymbol{F}^T\right)\boldsymbol{n}} \\
&= \sqrt{\boldsymbol{n} \cdot \boldsymbol{b}\boldsymbol{n}} \\
&=: \mid \boldsymbol{n} \mid_{\boldsymbol{b}},
\end{aligned} \tag{2.26}$$

where $\boldsymbol{b}$ is *the left Cauchy-Green tensor*, which is none other than *the push-forward* of the inverse of the Lagrangian metric tensor, $\boldsymbol{G}^{-1}$

$$\boldsymbol{b} := \boldsymbol{\varphi}_*\left(\boldsymbol{G}^{-1}\right) = \boldsymbol{F}\boldsymbol{G}^{-1}\boldsymbol{F}^T. \tag{2.27}$$

The *push-forward* and *pull-back* operations can be carried out easily by using the *commutative diagram* presented in Figure 2.5.

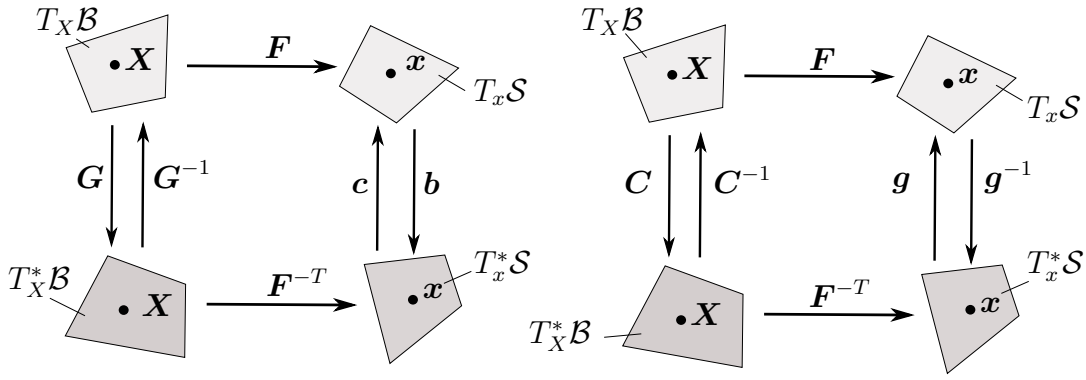

Figure 2.5: *Commutative Diagram* for deformation tensors. Combination of the *push-forward* and *pull-back* operations among the deformation tensors.

2.1.3 Material and Spatial Velocity Gradients

The time rate of change of a vector $\boldsymbol{t} \in T_x\mathcal{S}$, which is the spatial form of the Lagrangian vector $\boldsymbol{T} \in T_X\mathcal{B}$ and can be found by the relation $\boldsymbol{t} = \boldsymbol{F}\boldsymbol{T}$, is defined as

$$\dot{\boldsymbol{t}} := \dot{\boldsymbol{F}}\boldsymbol{T} =: \boldsymbol{L}\boldsymbol{T}\,, \tag{2.28}$$

where the time rate of change of deformation gradient can be determined by:

$$\boldsymbol{L} = \dot{\boldsymbol{F}} = \frac{\partial}{\partial t}\Big(\nabla_{\boldsymbol{X}}\boldsymbol{\varphi}\big(\boldsymbol{X},t\big)\Big) = \nabla_{\boldsymbol{X}}\Big(\frac{\partial}{\partial t}\boldsymbol{\varphi}\big(\boldsymbol{X},t\big)\Big) = \nabla_{\boldsymbol{X}}\boldsymbol{V}\big(\boldsymbol{X},t\big)\,. \tag{2.29}$$

Geometrically, the material velocity gradient $\boldsymbol{L}$ can be expressed as

$$\boldsymbol{L}\big(\boldsymbol{X},t\big) := \begin{cases} T_X\mathcal{B} \to T_x\mathcal{S}\,, \\ \boldsymbol{T} \mapsto \dot{\boldsymbol{t}} = \boldsymbol{L}\boldsymbol{T}\,. \end{cases} \tag{2.30}$$

Hence, the time derivative of the deformation gradient can also be called as *the material velocity gradient*. Employing that $\boldsymbol{T} = \boldsymbol{F}^{-1}\boldsymbol{t}$, *spatial velocity gradient* can be defined as

$$\dot{\boldsymbol{t}} := \dot{\boldsymbol{F}}\boldsymbol{F}^{-1}\boldsymbol{t} =: \boldsymbol{l}\boldsymbol{t}\,, \tag{2.31}$$

where

$$\boldsymbol{l} := \dot{\boldsymbol{F}}\boldsymbol{F}^{-1} = \boldsymbol{L}\boldsymbol{F}^{-1} = \nabla_{\boldsymbol{X}}\Big(\boldsymbol{V}\big(\boldsymbol{X},t\big)\Big)\cdot\nabla_{\boldsymbol{x}}\boldsymbol{X} = \nabla_{\boldsymbol{x}}\Big(\boldsymbol{v}\big(\boldsymbol{x},t\big)\Big)\,. \tag{2.32}$$

2.1.4 The Lie Derivative of Spatial Objects

The Lie derivative is associated with the relative change of a spatial object in time. The Lie derivative of a spatial object can be determined in three steps:

1. *Pull-back* of the spatial object to the reference configuration
2. Material time derivative of the pulled-back object
3. *Push-forward* of the material time derivative of the pulled-back object

In other words, the Lie derivative of the spatial object can be determined by

$$\mathcal{L}_{\boldsymbol{v}}(\,\bullet\,) = \boldsymbol{\varphi}_*\Big[\frac{d}{dt}\{\boldsymbol{\varphi}^*(\,\bullet\,)\}\Big]\,. \tag{2.33}$$

To illustrate, the Lie derivative of the Eulerian metric $\boldsymbol{g}$ can be determined by:

1. ***Pull-back operation***

$$\boldsymbol{\varphi}^*(\boldsymbol{g}) = \boldsymbol{F}^T\boldsymbol{g}\boldsymbol{F} = \boldsymbol{C}\,,$$

2. ***Material time derivative of*** $\boldsymbol{C}$

$$\frac{d}{dt}\boldsymbol{C} = \dot{\boldsymbol{C}} = \dot{\boldsymbol{F}}^T\boldsymbol{g}\boldsymbol{F} + \boldsymbol{F}^T\dot{\boldsymbol{g}}\boldsymbol{F} + \boldsymbol{F}^T\boldsymbol{g}\dot{\boldsymbol{F}}\,,$$

   where $\dot{\boldsymbol{g}} = \boldsymbol{0}$,

3. ***Push-forward operation***

$$\begin{aligned}\boldsymbol{\varphi}_*\big(\dot{\boldsymbol{F}}^T\boldsymbol{g}\boldsymbol{F} + \boldsymbol{F}^T\boldsymbol{g}\dot{\boldsymbol{F}}\big) &= \boldsymbol{F}^{-T}\Big[\dot{\boldsymbol{F}}^T\boldsymbol{g}\boldsymbol{F} + \boldsymbol{F}^T\boldsymbol{g}\dot{\boldsymbol{F}}\Big]\boldsymbol{F}^{-1}\\ &= \big(\dot{\boldsymbol{F}}\boldsymbol{F}^{-1}\big)^T\boldsymbol{g} + \boldsymbol{g}\big(\dot{\boldsymbol{F}}\boldsymbol{F}^{-1}\big)\\ &= \boldsymbol{l}^T\boldsymbol{g} + \boldsymbol{g}\boldsymbol{l}\,,\end{aligned}$$

   Hence, the Lie derivative of Eulerian metric tensor is found to be $\mathcal{L}_{\boldsymbol{v}}\big(\boldsymbol{g}\big) = \boldsymbol{l}^T\boldsymbol{g} + \boldsymbol{g}\boldsymbol{l}$

It is important to note that the Lie derivative yields the basic class of objective time derivatives of spatial tensors, since they are not affected from the superimposed rigid body motions.

2.1.5 The Cauchy's Mechanical Stress Theorem

Consider a material body in its deformed configuration $\mathcal{S}$. When an arbitrary subdomain $\mathcal{P}_\mathcal{B} \subset \mathcal{B}$ is extracted from the whole body $\mathcal{S}$, there exist a surface traction $\boldsymbol{t}$ on the removed body according to *the Euler's cut principle*. In a similar manner, on a surface of the material subdomain $\mathcal{P}_\mathcal{B} \subset \mathcal{B}$, a traction force $\tilde{\boldsymbol{T}}$ occurs due to the rest of the body when the material is cut out off the whole material domain $\mathcal{B}$ in the undeformed configuration. Here, $\boldsymbol{t}$ represents the *Cauchy (true) surface traction vector* exerted on the surface of the particular subdomain $\partial\mathcal{P}_\mathcal{S}$ which is depicted in Figure 2.35.

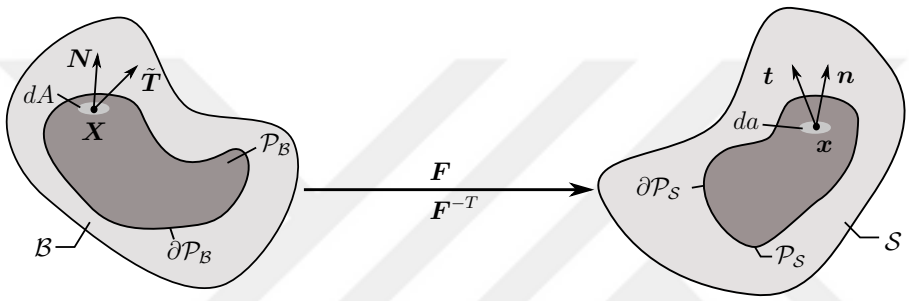

Figure 2.6: *Euler's Cut Principle*. The undeformed $\mathcal{P}_\mathcal{B}$ and deformed $\mathcal{P}_\mathcal{S}$ parts, their corresponding traction and normal vectors.

According to *the Cauchy's stress theorem*, there exists a unique second-order tensor called *the Cauchy* or *true stress* tensor and denoted as $\boldsymbol{\sigma}$ such that

$$\boldsymbol{t}\big(\boldsymbol{x}, t, \boldsymbol{n}\big) := \boldsymbol{\sigma}\big(\boldsymbol{x}, t\big) \cdot \boldsymbol{n}\,. \tag{2.34}$$

Hence, the Cauchy stress tensor can be defined as an Eulerian object that maps normal vectors $\boldsymbol{n}$ onto tangent vectors $\boldsymbol{t}$ and denoted as

$$\boldsymbol{\sigma} := \begin{cases} T_x^*\mathcal{S} \to T_x\mathcal{S}\,, \\ \boldsymbol{n} \mapsto \boldsymbol{t} = \boldsymbol{\sigma}\,\boldsymbol{n}, \quad \text{where} \quad t^i = \sigma^{ij} n_j\,. \end{cases} \tag{2.35}$$

The Cauchy stress tensor is symmetric, i.e. $\boldsymbol{\sigma} = \boldsymbol{\sigma}^T$. The symmetry condition for the Cauchy stress tensor will be shown in the upcoming sections.

There are other stress measures employed, one of which is called *the Kirchhoff stress* tensor. The Kirchhoff stress tensor is also a spatial stress measure and is defined as $\boldsymbol{\tau} := J\boldsymbol{\sigma}$. From the geometrical viewpoint, $\boldsymbol{\tau}$ can be tought as

$$\boldsymbol{\tau} := \begin{cases} T_x^*\mathcal{S} \to T_x\mathcal{S}\,, \\ \boldsymbol{n} \mapsto J\boldsymbol{t} = \boldsymbol{\tau}\,\boldsymbol{n}, \quad \text{where} \quad Jt^i = \tau^{ij}n_j\,, \end{cases} \tag{2.36}$$

where J is the *Jacobian* defined in (2.10). Since the Cauchy stress tensor is symmetric, the Kirchhoff stress tensor is also symmetric; that is, $\boldsymbol{\tau} = \boldsymbol{\tau}^T$. There are also Lagrangian counterparts of the Eulerian Cauchy's theorem that transforms the Lagrangian normal vector $\boldsymbol{N}$ onto the Eulerian traction vector $\boldsymbol{T} \in T_x\mathcal{S}$ by introducing *the first Piola-Kirchhoff* stress tensor $\boldsymbol{P}$. Hence the Lagrangian counterpart of the Cauchy's theorem reads

$$\boldsymbol{T}\big(\boldsymbol{x}, t, \boldsymbol{N}\big) = \boldsymbol{P}\big(\boldsymbol{x}, t\big) \cdot \boldsymbol{N}\,. \tag{2.37}$$

The first Piola-Kirchhoff stress is defined as

$$\boldsymbol{P} := \begin{cases} T_X^*\mathcal{B} \to T_x\mathcal{S}\,, \\ \boldsymbol{N} \mapsto \boldsymbol{T} = \boldsymbol{P}\,\boldsymbol{N}, \quad \text{where} \quad T^i = P^{iJ}N_J\,. \end{cases} \tag{2.38}$$

It is important to emphasize that $\boldsymbol{T}$ is the traction vector associated with the deformed surface on $\partial\mathcal{P}_\mathcal{S}$ and both $\boldsymbol{t}$ and $\boldsymbol{T}$ are parallel vectors. $\boldsymbol{T}$ is required to satisfy

$$\boldsymbol{T}dA = \boldsymbol{t}da\,, \tag{2.39}$$

for force equality. Employing (2.13) and (2.39), the first Piola-Kirchhoff stress tensor can be determined by

$$\begin{aligned} \boldsymbol{T}dA &= \boldsymbol{t}da\,, \\ \boldsymbol{P}\,\boldsymbol{N}\,dA &= \boldsymbol{\sigma}\,\boldsymbol{n}\,da, \quad \text{where} \quad \boldsymbol{n}\,da = J\,\boldsymbol{F}^{-T}\,\boldsymbol{N}\,dA\,, \\ \boldsymbol{P}\,\boldsymbol{N}\,dA &= J\,\boldsymbol{\sigma}\,\boldsymbol{F}^{-T}\,\boldsymbol{N}\,dA\,. \end{aligned} \tag{2.40}$$

Employing last part of (2.40), $\boldsymbol{P} = J\,\boldsymbol{\sigma}\,\boldsymbol{F}^{-T}$ is obtained. As a result, the first Piola-Kirchhoff stress tensor is the pull-back of the Kirchhoff stress tensor, or vice versa

$$\boldsymbol{P} = \boldsymbol{\varphi}^*\big(\boldsymbol{\tau}\big)\,. \tag{2.41}$$

Another important point for the first Piola-Kirchhoff stress tensor is that it is a *two-point* tensor such that it maps a Lagrangian normal to an Eulerian vector. In addition, although the Cauchy and Kirchhoff stress tensors are symmetric, i.e. $\boldsymbol{\sigma} = \boldsymbol{\sigma}^T$ and $\boldsymbol{\tau} = \boldsymbol{\tau}^T$, based on (2.40) the first Piola-Kirchhoff stress tensor is generally unsymmetric as in the case of deformation gradient.

Another Cauchy type theorem in the Lagrangian configuration defines the *second Piola-Kirchhoff* stress tensor that maps a Lagrangian normal vector $\boldsymbol{N} \in T_X^*\mathcal{B}$ to a Lagrangian traction vector $\tilde{\boldsymbol{T}} \in T_X\mathcal{B}$ such that

$$\tilde{\boldsymbol{T}}\big(\boldsymbol{X}, t, \boldsymbol{N}\big) = \boldsymbol{S}\big(\boldsymbol{X}, t\big) \cdot \boldsymbol{N}\,, \tag{2.42}$$

where

$$\boldsymbol{S} := \begin{cases} T_X^*\mathcal{B} \to T_X\mathcal{B}\,, \\ \boldsymbol{N} \mapsto \tilde{\boldsymbol{T}} = \boldsymbol{S}\,\boldsymbol{N}, \quad \text{where} \quad \tilde{T}^I = S^{IJ} N_J\,. \end{cases} \tag{2.43}$$

It is known that the nominal stress traction vector $\boldsymbol{T} \in T_x\mathcal{S}$ is the push-forward of $\tilde{\boldsymbol{T}} \in T_X\mathcal{B}$. In other words, it can be written as follows:

$$\tilde{\boldsymbol{T}} = \boldsymbol{F}^{-1}\,\boldsymbol{T}\,. \tag{2.44}$$

Combining (2.38), and (2.40-2.44), the second Piola-Kirchhoff stress tensor is found to be the pull-back of the first Piola-Kirchhoff stress tensor and the Kirchhoff stress tensor. To illustrate, employing (2.40), (2.43), and (2.44), the second Piola-Kirchhoff stress tensor can be obtained by

$$\tilde{\boldsymbol{T}} = \boldsymbol{F}^{-1}\,\boldsymbol{T} = \boldsymbol{F}^{-1}\,\boldsymbol{P}\,\boldsymbol{N} = \boldsymbol{S}\,\boldsymbol{N} = \boldsymbol{F}^{-1}\,\boldsymbol{\tau}\,\boldsymbol{F}^{-T}\,\boldsymbol{N}\,. \tag{2.45}$$

Consequently, (2.45) can be denoted as

$$\boldsymbol{S} = \boldsymbol{\varphi}^*\big(\boldsymbol{P}\big) = \boldsymbol{\varphi}^*\big(\boldsymbol{\tau}\big)\,. \tag{2.46}$$

Apperantly, all these push-forward and pull-back operations can be illustrated by using the commutative diagram described in Figure 2.7.

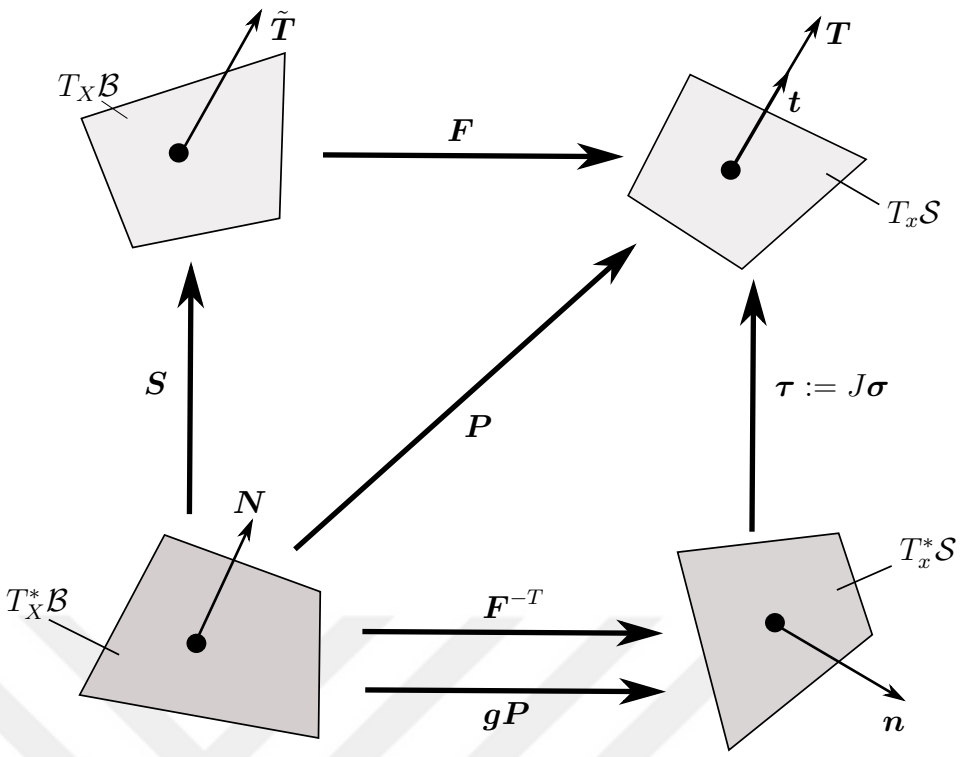

Figure 2.7: *Commutative Diagram* for stress tensors. Combination of the *push-forward* and *pull-back* operations among the stress measures.

2.2 Fundamentals of Electrostatics

This section will cover the basic expressions of electrostatic. Thus, the associated electro-mechanical equations will be obtained by combining electrical expressions with the mechanical equations introduced in Section 2.1. Fundamental equations of electrostatics such as Coulomb's law, Lorentz's law, Faraday's law and Maxwell's equations for electrostatics will be presented at first. Then, the balance equations of continuum electromechanics will be introduced using geometric transformations of electrical expressions for each configuration in order to obtain the coupled electro-mechanical equations for upcoming chapters. For detailed information on electrostatics and coupled electromechanics, the reader is referred to the references [9, 15, 26] and the references cited therein.

2.2.1 Coulomb's Law and Lorentz Law of Force

One of the essential laws of electrostatics is the Coulomb's law, which has been discovered by Charles Augustin de Coulomb while conducting experiments on charged particles at rest [26]. Coulomb states that when two charged particles, which are denoted by q and Q with opposite signs, are placed at locations $\boldsymbol{x}$ and $\boldsymbol{x}'$, respectively. They attract each other, whereas they repel each other when these two charges have same sign. The law that determines the force of attraction on these charges is called *Coulomb's law*. Specifically, the force exerted on the charge q at position $\boldsymbol{x}$ due to the charge Q at position $\boldsymbol{x}'$ can be determined as

$$\boldsymbol{f}\big(\boldsymbol{x}, q\big) := \frac{1}{4\pi\epsilon_0} q\, Q\, \frac{\boldsymbol{x} - \boldsymbol{x}'}{\mid \boldsymbol{x} - \boldsymbol{x}' \mid^3}\,, \tag{2.47}$$

where ϵ_0 is called the electric permittivity of free space and it is $8.854 \cdot 10^{-12}\big[\mathrm{F/m}\big]$ according to the SI system of units. Hence, the force of attraction on the particle q is dependent upon the magnitude and sign of the charge itself and the distance between the charges.

Another important electrostatic relation, the Lorentz law of force, states that the force of attraction on the charge q at rest exists due to the electric field $\boldsymbol{e}\big(\boldsymbol{x}\big)$ at position $\boldsymbol{x}$ due to the presence of the electric charge Q at position $\boldsymbol{x}'$ which can be defined as

$$\boldsymbol{f}\big(\boldsymbol{x}, q\big) := q\boldsymbol{e}\big(\boldsymbol{x}\big), \quad \text{where} \quad \boldsymbol{e}\big(\boldsymbol{x}\big) = \frac{1}{4\pi\epsilon_0}\, Q\, \frac{\boldsymbol{x} - \boldsymbol{x}'}{\mid \boldsymbol{x} - \boldsymbol{x}' \mid^3}\,. \tag{2.48}$$

It is important to state that electric charge q must be as small as possible, i.e. $q \to 0$, in order that it does not perturb the system. In other words, if magnitude of q is considerably high, then, the force of attraction on charge Q may change its position, hence, influence the electric field $\boldsymbol{e}\big(\boldsymbol{x}\big)$.

The Lorentz law, given in (2.48), considers the attractive force on the charge q in the presence of a single charge Q. Considering several source of charges Q_i at positions $\boldsymbol{x}_i'$ where $i = 1, 2, \ldots, n$, *the principle of superposition* can be used to find out the resultant force of attraction on the test charge q, i.e.

$$\boldsymbol{e}\big(\boldsymbol{x}\big) = \sum_{i=1}^{n} \frac{Q_i}{4\pi\epsilon_0}\, \frac{\boldsymbol{x} - \boldsymbol{x}'}{\mid \boldsymbol{x} - \boldsymbol{x}' \mid^3}\,. \tag{2.49}$$

When a case where magnetic effects are not ignored and the particle q is not at rest but moving is considered and the instantaneous velocity of the particle q is assumed to be $\boldsymbol{v}$ at position $\boldsymbol{x}$, there is an extra force, to which particle q is subjected, due to the magnetic induction vector $\boldsymbol{b}^{mg}$ at position $\boldsymbol{x}$. This force occurs in the direction perpendicular to the instantaneous velocity $\boldsymbol{v}$. Therefore, the Lorentz law can be generalized as

$$\boldsymbol{f}\big(\boldsymbol{x}, q, \boldsymbol{v}\big) := q\boldsymbol{e}\big(\boldsymbol{x}\big) + q\boldsymbol{v} \times \boldsymbol{b}^{mg} \,. \tag{2.50}$$

2.2.2 Faraday's Law

Considering the case that several source charges Q_i at positions $\boldsymbol{x}_i'$ where $i = 1, \ldots, n$ constitute a spherical volume $\mathcal{S}$ whose center is located at position $\boldsymbol{x}'$, the total charge within $\mathcal{S}$ can be determined by

$$\sum_{i=1}^{n} Q_i = \int_{\mathcal{S}} \rho_e\big(\boldsymbol{x}'\big) \, dv' \,, \tag{2.51}$$

where $\rho_e\big(\boldsymbol{x}'\big)$ is called as *volume charge density* within the confined volume $\mathcal{S}$. Moreover, it must be emphasized that $dv' = dv'\big(\boldsymbol{x}'\big)$.

Thus, the relation in (2.49) can be recast into

$$\boldsymbol{e}\big(\boldsymbol{x}\big) = \sum_{i=1}^{n} \frac{Q_i}{4\pi\epsilon_0} \frac{\boldsymbol{x} - \boldsymbol{x}'}{\mid \boldsymbol{x} - \boldsymbol{x}' \mid^3} = \frac{1}{4\pi\epsilon_0} \int_{\mathcal{S}} \rho_e\big(\boldsymbol{x}'\big) \frac{\boldsymbol{x} - \boldsymbol{x}'}{\mid \boldsymbol{x} - \boldsymbol{x}' \mid^3} \, dv' \,. \tag{2.52}$$

For vector calculus, it is known that gradient operation can be handled by

$$\frac{\boldsymbol{x} - \boldsymbol{x}'}{\mid \boldsymbol{x} - \boldsymbol{x}' \mid^3} := -\nabla_{\boldsymbol{x}}\Big(\frac{1}{\mid \boldsymbol{x} - \boldsymbol{x}' \mid}\Big) = \nabla_{\boldsymbol{x}'}\Big(\frac{1}{\mid \boldsymbol{x} - \boldsymbol{x}' \mid}\Big) \,. \tag{2.53}$$

Substituting (2.53) into (2.52), the electric field because of the contributions from all source charges within volume $\mathcal{S}$ can be rewritten as

$$\boldsymbol{e}\big(\boldsymbol{x}\big) = -\nabla_{\boldsymbol{x}}\Big(\frac{1}{4\pi\epsilon_0} \int_{\mathcal{S}} \frac{\rho_e\big(\boldsymbol{x}'\big)}{\mid \boldsymbol{x} - \boldsymbol{x}' \mid} \, dv'\Big) \,. \tag{2.54}$$

The latter states that electric field vector can be obtained by the gradient of a scalar field function known as *the electrostatic potential* or *the electric potential*. Consequently, the electric potential can be defined as

$$\phi\big(\boldsymbol{x}\big) := \frac{1}{4\pi\epsilon_0} \int_{\mathcal{S}} \frac{\rho_e\big(\boldsymbol{x}'\big)}{\mid \boldsymbol{x} - \boldsymbol{x}' \mid} \, dv' \,. \tag{2.55}$$

Since the curl of a gradient of a scalar-valued function is zero, that is, $\nabla_{\boldsymbol{x}} \times \nabla_{\boldsymbol{x}} \big(\blacksquare\big) = \mathbf{0}$ where $\blacksquare$ is any scalar-valued function, *the first equation of electrostatics* or *Faraday's law of electrostatics* can be obtained as

$$\text{curl}\,\big(\boldsymbol{e}\big) := \mathbf{0} \quad \text{where} \quad \boldsymbol{e} = -\nabla_{\boldsymbol{x}}\,\phi\,. \tag{2.56}$$

2.2.3 Gauss's Flux Theorem

The Gauss's law of electrostatics expresses the electric flux through any closed surface $\partial\mathcal{S}$ of volume $\mathcal{S}$ because of a source charge Q. For simplicity, to illustrate the Gauss's flux theorem, the closed volume $\mathcal{S}$ is assumed to be a sphere and that the source charge is placed at the center of the sphere located at $\boldsymbol{x}'$. Thus, (2.48) can be rewritten in terms of the direction normal of the electric field vector as

$$\boldsymbol{e}\big(\boldsymbol{x}\big) = \frac{1}{4\pi\epsilon_0}\,Q\,\frac{\boldsymbol{n}}{\mid \boldsymbol{x}-\boldsymbol{x}'\mid^2}\,, \tag{2.57}$$

where $\boldsymbol{n} := \frac{\boldsymbol{x}-\boldsymbol{x}'}{|\boldsymbol{x}-\boldsymbol{x}'|}$ is defined as the radially outward direction normal at point $\boldsymbol{x} \in \partial\mathcal{S}$. As a consequence, for a single source charge, flux through any infinitesimal area element *da* at point $\boldsymbol{x}$ can be depicted as

$$\boldsymbol{e}\cdot\boldsymbol{n}\;da := \mid \boldsymbol{e} \mid\; da = \frac{1}{4\pi\epsilon_0}\,\frac{Q da}{\mid \boldsymbol{x}-\boldsymbol{x}'\mid^2}\,, \tag{2.58}$$

where $da = \mid \boldsymbol{x}-\boldsymbol{x}'\mid^2 \sin\theta d\theta\; d\gamma$ in a spherical coordinate system. The total flux through the surface of sphere can be determined by

$$\oint_{\partial\mathcal{S}} \boldsymbol{e}\cdot d\boldsymbol{a} = \int_0^{2\pi}\int_0^{\pi} \frac{Q}{4\pi\epsilon_0}\sin\theta d\theta\; d\gamma = \frac{Q}{\epsilon_0}\,. \tag{2.59}$$

Note that (2.59) is written for a single source charge within the volume $\mathcal{S}$ enclosed by the surface $\partial\mathcal{S}$. For the same volume, provided that there are certain amount of source charges within the volume $\mathcal{S}$, the former can be generalized by employing the principle of superposition as

$$\oint_{\partial\mathcal{S}} \boldsymbol{e}\cdot d\boldsymbol{a} = \sum_{i=1}^{n} \frac{Q_i}{\epsilon_0}\,. \tag{2.60}$$

Combining (2.51) and (2.60), and employing the divergence theorem, (2.60) can also be written as

$$\int_{\partial\mathcal{S}} \boldsymbol{e} \cdot d\boldsymbol{a} = \int_{\mathcal{S}} \text{div}\,\big(\boldsymbol{e}\big) dv' = \int_{\mathcal{S}} \frac{\rho_e\big(\boldsymbol{x}'\big)}{\epsilon_0}\, dv' \,. \tag{2.61}$$

The local form of 2.61 then becomes

$$\text{div}\,\big(\boldsymbol{e}\big) := \frac{\rho_e}{\epsilon_0}\,, \tag{2.62}$$

which is called *the second equation of electrostatics* or *Gauss's law*.

The work done by electric field $W^{\boldsymbol{e}}$ on a particle q can be determined by

$$W^{\boldsymbol{e}} = \int_{\boldsymbol{x}_1}^{\boldsymbol{x}_2} \boldsymbol{f}\big(\boldsymbol{x}, q\big) \cdot d\boldsymbol{x}\,. \tag{2.63}$$

Incorporating (2.48), (2.56), into (2.63), it becomes

$$W^{\boldsymbol{e}} = \int_{\boldsymbol{x}_1}^{\boldsymbol{x}_2} q\boldsymbol{e}\big(\boldsymbol{x}\big) \cdot d\boldsymbol{x} = \int_{\boldsymbol{x}_2}^{\boldsymbol{x}_1} q\, \nabla_{\boldsymbol{x}}\phi \cdot d\boldsymbol{x}\,. \tag{2.64}$$

Using the fundamental theorem of calculus, (2.64) is tranformed into

$$\int_{\boldsymbol{x}_2}^{\boldsymbol{x}_1} q\, \nabla_{\boldsymbol{x}}\phi \cdot d\boldsymbol{x} = q\, \phi|_{\boldsymbol{x}_2}^{\boldsymbol{x}_1} = U_1 - U_2\,. \tag{2.65}$$

In short, the negative change of potential energy or work required to move the particle q from position $\boldsymbol{x}_1$ to $\boldsymbol{x}_2$ in the presence of an electric field $\boldsymbol{e}$ is the difference between the corresponding electric potentials at $\boldsymbol{x}_1$ and at $\boldsymbol{x}_2$ times the particle charge q. Since the change of potential energy is the negative of work done by the system, the potential energy at $\boldsymbol{x}_1$ and $\boldsymbol{x}_2$ will be determined as

$$U_1 = q\, \phi\big(\boldsymbol{x}_1\big), \quad \text{and} \quad U_2 = q\, \phi\big(\boldsymbol{x}_2\big)\,. \tag{2.66}$$

2.2.4 Electric Polarization and Electric Displacement Vector

Up to now, the electric field is applied in the vacuum. When the substance is placed in an electric field, there will be the Coulombic attraction on the atoms of the substance. At first, neutrallity of the nucleus will change, i.e. positive charges try to move in the direction of electric field and opposite occurs for the negative charges. Since negative

charges are lighter than the positive charges, at first, negative charges try to move in the opposite direction of electric field.

For a general case in a polarized atom, it is assumed that positive and negative charges are displaced by a small amount $\frac{\boldsymbol{\delta}}{2}$ from the initial center of nucleus. The vector from negative charges to positive charges is called *the electric dipole vector* or *the electric dipole moment*, $\boldsymbol{\delta}$. The electric field is also externally applied such that there exists a force of attraction on these particles such that the direction of the force is dependent upon the direction of the electric field vector and the sign of the particle. The net force on these particles in the atom will vanish. However, depending on the direction of $\boldsymbol{\delta}$, there occurs a torque between these two particles, trying to orient the particles in the direction of the electric field. The direction and magnitude of the torque can be expressed as

$$\boldsymbol{\Omega} := \boldsymbol{\delta} \times \boldsymbol{f} \,. \tag{2.67}$$

Using (2.48), the latter becomes

$$\begin{aligned} &\boldsymbol{\Omega} := \boldsymbol{\delta} \times q\boldsymbol{e} \\ &\boldsymbol{\Omega} := \boldsymbol{p} \times \boldsymbol{e} \quad \text{and} \quad \mid \boldsymbol{\Omega} \mid = \mid \boldsymbol{p} \mid\mid \boldsymbol{e} \mid \sin\big(\theta\big) \,, \end{aligned} \tag{2.68}$$

where $\boldsymbol{p} := q\boldsymbol{\delta}$ which is called *the electric polarization vector* directed from negative charges to positive charges and θ is the angle between electric field vector and electric dipole moment.

The infinitesimal work done by the torque is the scalar product of the torque, $\boldsymbol{\Omega}$, and infinitesimal rotation, $d\boldsymbol{\theta}$, i.e.

$$dW^{\boldsymbol{p}} := \boldsymbol{\Omega} \cdot d\boldsymbol{\theta} = -pe \sin\big(\theta\big) d\theta \,, \tag{2.69}$$

where "-" sign that is used in (2.69) indicates that the direction of the torque and the rotation is opposite. Hence, for finite rotations, the total work done on electric dipole by the electric field vector can be calculated as

$$W^{\boldsymbol{p}} = \int_{\theta_1}^{\theta_2} -pe \sin\big(\theta\big)\, d\theta = pe\Big(\cos\big(\theta_2\big) - \cos\big(\theta_1\big)\Big) \,. \tag{2.70}$$

Note that the expression in (2.70) is none other than the scalar product of the electric

polarization and the electric field vectors

$$\Delta W = U = \boldsymbol{p} \cdot \boldsymbol{e} \,. \tag{2.71}$$

As a result, combining (2.55), (2.66), and (2.71), the electric potential can be rewritten through the electric polarization

$$\phi(\boldsymbol{x}) = \int_{\mathcal{S}} \frac{1}{4\pi\epsilon_0} \frac{\boldsymbol{p}(\boldsymbol{x}') \cdot (\boldsymbol{x} - \boldsymbol{x}')}{\mid \boldsymbol{x} - \boldsymbol{x}' \mid^3} \, dv' \,. \tag{2.72}$$

According to [9] and many others, *dielectric materials* or just *dielectrics* are the materials that show certain polarization in the presence of an electric field such that positive charges accumulate on the surface in the direction of electric field vector and negative ones will move towards opposite direction due to the polarization. Hence, the total charge density in (2.62) can be decomposed into bound charges ρ_b and free charges ρ_f. Taking into consideration of the electric potantial incorporating polarization, (2.72), the electric potential can be rewritten for the dielectric materials using (2.53) as

$$\phi(\boldsymbol{x}) = \frac{1}{4\pi\epsilon_0} \int_{\mathcal{S}} \boldsymbol{p}(\boldsymbol{x}') \cdot \nabla_{\boldsymbol{x}'} \Big(\frac{1}{\mid \boldsymbol{x} - \boldsymbol{x}' \mid} \Big) \, dv' \,. \tag{2.73}$$

The divergence theorem is applied to (2.73) to obtain

$$\phi(\boldsymbol{x}) = \frac{1}{4\pi\epsilon_0} \int_{\mathcal{S}} \Big(-\nabla_{\boldsymbol{x}'} \cdot \boldsymbol{p}(\boldsymbol{x}') \Big) \frac{1}{\mid \boldsymbol{x} - \boldsymbol{x}' \mid} \, dv' + \frac{1}{4\pi\epsilon_0} \int_{\partial\mathcal{S}} \frac{\boldsymbol{p}(\boldsymbol{x}') \cdot \boldsymbol{n}'}{\mid \boldsymbol{x} - \boldsymbol{x}' \mid} \, da' \,, \tag{2.74}$$

which can be rewritten as

$$\phi(\boldsymbol{x}) = \frac{1}{4\pi\epsilon_0} \int_{\mathcal{S}} \frac{\rho_b}{\mid \boldsymbol{x} - \boldsymbol{x}' \mid} \, dv' + \frac{1}{4\pi\epsilon_0} \int_{\partial\mathcal{S}} \frac{\sigma_b}{\mid \boldsymbol{x} - \boldsymbol{x}' \mid} \, da' \,. \tag{2.75}$$

Since it is known that $\rho_b(\boldsymbol{x}') = -\nabla_{\boldsymbol{x}'} \cdot \boldsymbol{p}(\boldsymbol{x}') =: -\text{div}\,'(\boldsymbol{p})$ at any point $\boldsymbol{x}'$ in V, it can be inferred that $\rho_b(\boldsymbol{x}) = -\nabla_{\boldsymbol{x}} \cdot \boldsymbol{p}(\boldsymbol{x}) = -\text{div}\,(\boldsymbol{p})$ at any point $\boldsymbol{x}$ in V. Therefore, the first term on the right-hand side of (2.75) is defined as the contribution of volume density of bound charges, and the second term is the *Cauchy's theorem for electric expressions* as follows

$$\rho_b = -\text{div}\,(\boldsymbol{p}) \quad \text{in} \quad \mathcal{S} \,, \quad \sigma_b = \boldsymbol{p} \cdot \boldsymbol{n} \quad \text{on} \quad \partial\mathcal{S} \,. \tag{2.76}$$

Since the total volume charge denisity is detemined by (2.62) and the latter is the bound charge density for polarized materials or dielectric materials, the rest can be

explained by the density of free charges, i.e. ρ_f. Thus, the free charge density can be found by

$$\begin{aligned} &\rho_e = \rho_b + \rho_f \,, \\ &\epsilon_0 \operatorname{div}\big(\boldsymbol{e}\big) = -\operatorname{div}\big(\boldsymbol{p}\big) + \rho_f \,, \\ &\operatorname{div}\big(\epsilon_0 \boldsymbol{e} + \boldsymbol{p}\big) = \operatorname{div}\big(\boldsymbol{d}\big) = \rho_f \,, \end{aligned} \tag{2.77}$$

where $\boldsymbol{d} := \epsilon_0 \boldsymbol{e} + \boldsymbol{p}$ is *the electric displacement vector*. It should be noted that in isotropic linear dielectrics, the polarization vector is the parallel to the electric field vector, hence (2.77) simplifies to

$$\boldsymbol{d} = \epsilon_r \boldsymbol{e} \,, \tag{2.78}$$

where ϵ_r is the relative electric permittivity and different from the electric permittivity of vacuum ϵ_0. In order to understand the electric displacement vector, a capacitor should be considered. The capacitor, by definition, is a device that stores electric potential energy and electric charge. It consists of two conductors that surround dielectric material. Since there occur electric charges on these two parallel conductors, the electric field develops between them. In other words, one of the conductors is fully filled with positive charges whereas the other is filled with negative charges, resulting in the electric field between these two conductors. The electric field between two conductor plates is directed from positively charged conductor to negatively charged one. Due to the electric field, there exists bound charges on the surfaces of the dielectric due to the polarization. The orientation of the bound charges are expressed such that negative bound charges try to move to the surface of the positively charged conductor and vice versa. The orientation of the bound charges creates another electric field within the dielectric material whose direction is opposite to the electric field created by conductors. The total (or net) charge enclosed on the surface of the capacitor and dielectric is called free charges on the surface which are the consequence of the electric displacement vector. The electric displacement occurs until the net electric field vanishes, which may happen as long as charge distribution is canceled out [9, 48].

$$\int_{\partial \mathcal{S}} \boldsymbol{d} \cdot \boldsymbol{n} \, da = \int_{\partial \mathcal{S}} \sigma_f \, da \tag{2.79}$$

(2.79) is the Cauchy's theorem for electric expression.

2.2.5 Geometric Mapping For Electrical Objects

For continuum electromechanics, the transformation of electrical objects is essentially transformed to each other [9]. Using (2.56), the electric field vector in the Eulerian configuration is found as

$$\begin{aligned} \boldsymbol{e} &= -\nabla_{\boldsymbol{x}}\, \phi\,, \\ \phi\big(\boldsymbol{x}\big) &= -\int_{\boldsymbol{x}'}^{\boldsymbol{x}} \boldsymbol{e}\cdot d\boldsymbol{x} = \int_{\boldsymbol{x}}^{\boldsymbol{x}'} \boldsymbol{e}\cdot d\boldsymbol{x}\,. \end{aligned} \tag{2.80}$$

Combining (2.7) and (2.80), (2.80) can be recast into

$$\int_{\boldsymbol{x}}^{\boldsymbol{x}'} \boldsymbol{e}\cdot d\boldsymbol{x} = \int_{\boldsymbol{X}}^{\boldsymbol{X}'} \boldsymbol{e}\cdot \boldsymbol{F} d\boldsymbol{X} = \int_{\boldsymbol{X}}^{\boldsymbol{X}'} \boldsymbol{E}\cdot d\boldsymbol{X}\,, \tag{2.81}$$

where $\boldsymbol{e} \in T_x^*\mathcal{S}$ and $\boldsymbol{E} \in T_X^*\mathcal{B}$.

The Lagrangian electric field vector is denoted by $\boldsymbol{E}$ and it is *the pull-back* of the Eulerian electric field; that is,

$$\boldsymbol{E} = \boldsymbol{\varphi}^*\big(\boldsymbol{e}\big) = \boldsymbol{F}^T\boldsymbol{e}\,. \tag{2.82}$$

Rearranging the definition in (2.79) and employing the *Nanson's formula* for area map in (2.13), the electric displacement vector in the Lagrangian configuration can be obtained as

$$\int_{\partial\mathcal{S}} \boldsymbol{d}\cdot\boldsymbol{n} da = \int_{\partial\mathcal{B}} \boldsymbol{d}\cdot J\boldsymbol{F}^{-T}\boldsymbol{N} dA = \int_{\partial\mathcal{B}} \boldsymbol{D}\cdot\boldsymbol{N} dA \tag{2.83}$$

Accordingly, the electric displacement vector in the Lagrangian configuration $\boldsymbol{D}$ is defined as *the pull-back* of the Eulerian electric displacement.

$$\boldsymbol{D} = \boldsymbol{\varphi}^*\big(\boldsymbol{d}\big) = J\boldsymbol{F}^{-1}\boldsymbol{d} = \boldsymbol{F}^{-1}\tilde{\boldsymbol{d}}\,, \tag{2.84}$$

where $\tilde{\boldsymbol{d}} \in T_x\mathcal{S}$ and $\boldsymbol{D} \in T_X\mathcal{B}$.

Similarly, the electric polarization vector defined in (2.76) is the Eulerian tangent space can be transformed into its Lagrangian counterpart as

$$\int_{\partial\mathcal{S}} \boldsymbol{p}\cdot\boldsymbol{n} da = \int_{\partial\mathcal{B}} \boldsymbol{p}\cdot J\boldsymbol{F}^{-T}\boldsymbol{N} dA = \int_{\partial\mathcal{B}} \boldsymbol{P}\cdot\boldsymbol{N} dA \tag{2.85}$$

where $\boldsymbol{p} \in T_x\mathcal{S}$ and $\boldsymbol{P} \in T_X\mathcal{B}$.

The electric field, electric displacement, and electric polarization vectors in each setting can be shown in a commutative diagram as shown in Figure 2.8.

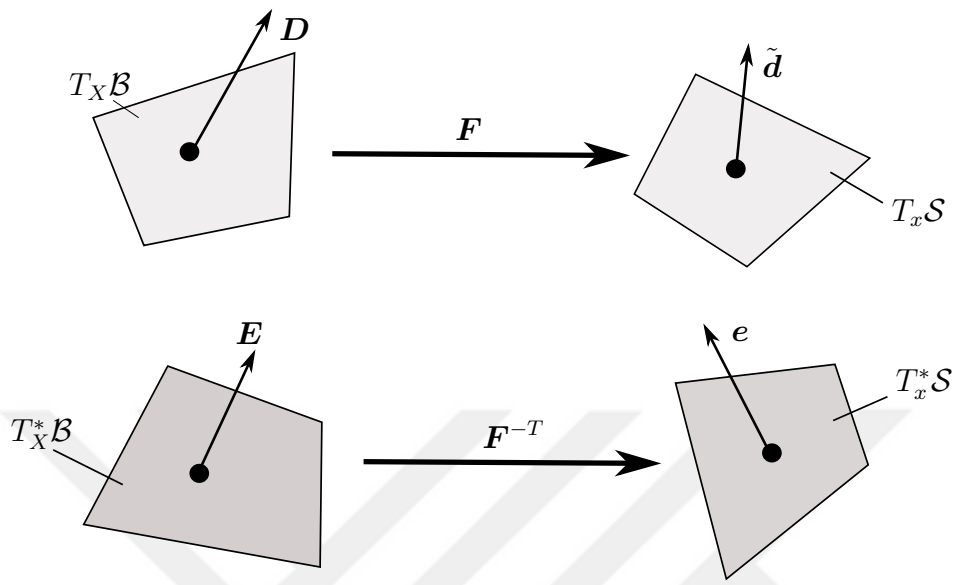

Figure 2.8: *Commutative Diagram* for electrostatical objects in each configuration.

However, it is important to emphasize that the electric field belong to the covariant (normal) space while the electric displacement and electric polarization vectors are defined in contravariant (tangent) space. Therefore, the relation (2.77) should be rewritten considering the space of the vectors. The final form of (2.77) will be presented as

$$\boldsymbol{d} = \epsilon_0 \boldsymbol{g}^{-1}\, \boldsymbol{e} + \boldsymbol{p} \tag{2.86}$$

2.2.6 Balance Laws of Continuum Electromechanics

The balance laws in continuum mechanics consist of a fundamental set of equations. These are the conservation of mass, the conservation of linear and angular momentum, and the conservation of energy. The contribution of an electric activity on the balance laws of continuum mechanics will show additional effects for the coupled electro-mechanical interactions. The global balance laws are written and all the for-

mulations applies for the rest of the thesis in the Eulerian setting.

2.2.6.1 Conservation of Mass

For closed systems such as $\mathcal{P}_{\mathcal{S}} \subset \mathcal{S}$ defined in *the Cauchy's theorem* in (2.35), there is no mass flow in or out with time, meaning that the mass cannot be produced or destroyed within the system. In other words, $\mathcal{M}_{\mathcal{P}_{\mathcal{B}}} = \mathcal{M}_{\mathcal{P}_{\mathcal{S}}}$. Hence, the relation for the conservation of mass of the cut $\mathcal{P}_{\mathcal{S}} \subset \mathcal{S}$ can be defined as

$$\begin{gathered} \mathcal{M}_{\mathcal{P}_{\mathcal{B}}} = \mathcal{M}_{\mathcal{P}_{\mathcal{S}}} \,, \\ \int_{\mathcal{P}_{\mathcal{B}}} \rho_0\big(\boldsymbol{X}\big)\; dV = \int_{\mathcal{P}_{\mathcal{S}}} \rho\big(\boldsymbol{x}, t\big)\; dv \,. \end{gathered} \tag{2.87}$$

Recalling the relation between the volume elements, i.e. *the Jacobi map* defined in (2.11), (2.87) becomes

$$\int_{\mathcal{P}_{\mathcal{B}}} \rho_0\big(\boldsymbol{X}\big)\; dV = \int_{\mathcal{P}_{\mathcal{B}}} \rho\big(\boldsymbol{x}, t\big)\; JdV \,. \tag{2.88}$$

Localizing the latter for arbitrarily small $\mathcal{P}_{\mathcal{B}}$ we end up with the first equation of the conservation of mass

$$\rho_0\big(\boldsymbol{X}\big) = J\; \rho\big(\boldsymbol{x}, t\big) \,. \tag{2.89}$$

Since the mass density in the Lagrangian setting does not depend on time, $(2.87)_2$ can be reconsidered as

$$\begin{gathered} \frac{d}{dt}\big(\mathcal{M}_{\mathcal{P}_{\mathcal{B}}}\big) = 0 = \frac{d}{dt}\big(\mathcal{M}_{\mathcal{P}_{\mathcal{S}}}\big) \,, \\ \frac{d}{dt}\Big[\int_{\mathcal{P}_{\mathcal{B}}} \rho_0\big(\boldsymbol{X}\big)\; dV\Big] = \frac{d}{dt}\Big[\int_{\mathcal{P}_{\mathcal{B}}} \rho\big(\boldsymbol{x}, t\big)\; JdV\Big] \,. \end{gathered} \tag{2.90}$$

Using the chain rule for $(2.90)_2$, it will possess its final form as

$$\frac{d}{dt}\Big[\int_{\mathcal{P}_{\mathcal{B}}} \rho\big(\boldsymbol{x}, t\big)\; JdV\Big] = \int_{\mathcal{P}_{\mathcal{B}}} \dot{\rho}\big(\boldsymbol{x}, t\big)\; JdV + \int_{\mathcal{P}_{\mathcal{B}}} \rho\big(\boldsymbol{x}, t\big)\; \dot{J}dV \,. \tag{2.91}$$

(2.91) has to hold locally as well, i.e.

$$\dot{\rho}J + \rho\dot{J} = \dot{\rho}_0 = 0 \,. \tag{2.92}$$

The rate of *the Jacobi map*, $J = \det\big(\boldsymbol{F}\big)$, can be obtained as

$$\dot{J} = \frac{\partial}{\partial \boldsymbol{F}}\big[\det\boldsymbol{F}\big] : \dot{\boldsymbol{F}} = J\boldsymbol{F}^{-T} : \dot{\boldsymbol{F}} = J\mathbf{1} : \dot{\boldsymbol{F}}\boldsymbol{F}^{-1} \,. \tag{2.93}$$

In (2.93), $\dot{\boldsymbol{F}}\boldsymbol{F}^{-1}$ is known as spatial velocity gradient in (2.32). Finally, the rate equation for the conservation of mass is obtained as

$$J\dot{\rho} + J\rho\mathbf{1} : \boldsymbol{l} = 0 \,, \tag{2.94}$$

or $\forall J \neq 0$, otherwise, (2.94) is trivially solved.

$$\dot{\rho} + \rho\mathbf{1} : \boldsymbol{l} = \dot{\rho} + \rho \operatorname{div}\big(\boldsymbol{v}\big) = 0 \,, \tag{2.95}$$

2.2.6.2 Balance of Linear Momentum

In the Eulerian setting, the balance of linear momentum can be expressed as the equality between the time rate of change of the linear momentum ($\boldsymbol{\mathcal{I}}_{\mathcal{P}_\mathcal{S}}$) and the sum of the forces ($\boldsymbol{\mathcal{F}}_{\mathcal{P}_\mathcal{S}}$) acting on the body, $\mathcal{P}_\mathcal{S}$.

$$\frac{\partial}{\partial t}\big(\boldsymbol{\mathcal{I}}_{\mathcal{P}_\mathcal{S}}\big) := \boldsymbol{\mathcal{F}}_{\mathcal{P}_\mathcal{S}} \tag{2.96}$$

with

$$\begin{aligned} \boldsymbol{\mathcal{I}}_{\mathcal{P}_\mathcal{S}} &:= \int_{\mathcal{P}_\mathcal{S}} \rho\big(\boldsymbol{x},t\big)\boldsymbol{v}\big(\boldsymbol{x},t\big)\; dv \,, \\ \boldsymbol{\mathcal{F}}_{\mathcal{P}_\mathcal{S}} &:= \int_{\mathcal{P}_\mathcal{S}} \rho\big(\boldsymbol{x},t\big)\boldsymbol{\gamma}\big(\boldsymbol{x},t\big)\; dv + \int_{\partial\mathcal{P}_\mathcal{S}} \boldsymbol{t}\big(\boldsymbol{x},t\big)\; da \,, \end{aligned} \tag{2.97}$$

where $\boldsymbol{\gamma}$ is the mass specific body force and $\boldsymbol{t}$ is the mechanical Cauchy stress traction, defined in (2.35). It must be stated that the total body force $\boldsymbol{\gamma}$ is the summation of the mechanical body force, $\boldsymbol{\gamma}^m$ and the electrical body force, $\boldsymbol{\gamma}^e$, that is, $\boldsymbol{\gamma} = \boldsymbol{\gamma}^m + \boldsymbol{\gamma}^e$

At first, the left-hand side of (2.96) is considered. In that case, the time rate of change of momentum can be expressed as

$$\frac{d}{dt}\Big[\int_{\mathcal{P}_\mathcal{S}} \rho\boldsymbol{v}\; dv\Big] = \int_{\mathcal{P}_\mathcal{S}} \rho\dot{\boldsymbol{v}}\; dv + \int_{\mathcal{P}_\mathcal{S}} \boldsymbol{v}\; \frac{d}{dt}\big[\rho dv\big] \tag{2.98}$$

The last term on the right-hand side of (2.99) is fulfilled automatically due to the conservation of mass. Therefore, (2.99) boils down to

$$\frac{d}{dt}\Big[\int_{\mathcal{P}_\mathcal{S}} \rho\boldsymbol{v}\; dv\Big] = \int_{\mathcal{P}_\mathcal{S}} \rho\dot{\boldsymbol{v}}\; dv \,. \tag{2.99}$$

In $(2.97)_2$, the surface integral term on the right-hand side can be transformed into a volume integral using *the Cauchy's theorem* (2.35) and the divergence theorem as

$$\int_{\partial\mathcal{P}_{\mathcal{S}}} \boldsymbol{t}\, da = \int_{\partial\mathcal{P}_{\mathcal{S}}} \boldsymbol{\sigma}\cdot\boldsymbol{n}\, da = \int_{\mathcal{P}_{\mathcal{S}}} \operatorname{div}\big(\boldsymbol{\sigma}\big) dv\,. \tag{2.100}$$

Using $(2.97)_2$, (2.99), and (2.100), the final form of the balance of linear momentum can be written as

$$\int_{\mathcal{P}_{\mathcal{S}}} \rho\, \dot{\boldsymbol{v}}\, dv = \int_{\mathcal{P}_{\mathcal{S}}} \rho\boldsymbol{\gamma}\, dv + \int_{\mathcal{P}_{\mathcal{S}}} \operatorname{div}\big(\boldsymbol{\sigma}\big) dv\,. \tag{2.101}$$

The local form of (2.101) can be written for an arbitrary cut out $\mathcal{P}_{\mathcal{S}}$:

$$\rho\dot{\boldsymbol{v}} = \operatorname{div}\big(\boldsymbol{\sigma}\big) + \rho\boldsymbol{\gamma}\,, \tag{2.102}$$

where $\boldsymbol{\sigma}$ is the mechanical Cauchy stress. For the quasi-static case, (2.102) simplifies to

$$\operatorname{div}\big(\boldsymbol{\sigma}\big) + \rho\boldsymbol{\gamma} = \boldsymbol{0} \tag{2.103}$$

Recall that the total body force can be decomposed into two by considering mechanical and electrical contributions; that is, $\boldsymbol{\gamma} = \boldsymbol{\gamma}^m + \boldsymbol{\gamma}^e$. According to [9], the electric body force can be written as

$$\rho\boldsymbol{\gamma}^e = \operatorname{div}\big(\boldsymbol{\sigma}^e\big) = \nabla_{\boldsymbol{x}}\boldsymbol{e}\cdot\boldsymbol{p} + \rho_f\boldsymbol{g}^{-1}\boldsymbol{e}\,, \tag{2.104}$$

where $\boldsymbol{\sigma}^e = \boldsymbol{g}^{-1}\boldsymbol{e}\otimes\boldsymbol{d} - \frac{1}{2}\epsilon_0\big(\boldsymbol{e}\cdot\boldsymbol{g}^{-1}\boldsymbol{e}\big)\,\boldsymbol{g}^{-1}$ is the electric Maxwell stress. According to [9], the former term on the right-hand side of (2.104) can be obtained by using the two dipole model of non-interacting dipoles such that using the generalized Lorentz law accounting for magnetic induction and the Taylor's series expansion, the forces applied on charges of dipole are rewritten and the resultant body force can be obtained. Moreover, the latter one in (2.104) is the consideration of the forces due to free charges. Hence, using (2.104) in (2.102), local form of the linear momentum expression for the quasi-static case transforms into

$$\operatorname{div}\big(\boldsymbol{\sigma} + \boldsymbol{\sigma}^e\big) + \rho\boldsymbol{\gamma}^m = \operatorname{div}\big(\overline{\boldsymbol{\sigma}}\big) + \rho\boldsymbol{\gamma}^m = \boldsymbol{0}\,, \tag{2.105}$$

where $\overline{\boldsymbol{\sigma}}$ is the total Cauchy stress and it is symmetric only for dielectric materials, i.e. $\boldsymbol{e} \parallel \boldsymbol{d}$.

2.2.6.3 Balance of Angular Momentum

The time change of angular momentum $\boldsymbol{\mathcal{D}}_{\mathcal{P}_\mathcal{S}}$ for the cut out element $\mathcal{P}_\mathcal{S}$ is equal to the resultant moment $\boldsymbol{\mathcal{M}}_{\mathcal{P}_\mathcal{S}}$ which is summation of moments generated by the forces acting on $\mathcal{P}_\mathcal{S}$. In other words,

$$\frac{d}{dt}\big(\boldsymbol{\mathcal{D}}_{\mathcal{P}_\mathcal{S}}\big) := \boldsymbol{\mathcal{M}}_{\mathcal{P}_\mathcal{S}} \,, \tag{2.106}$$

where

$$\begin{aligned} \boldsymbol{\mathcal{D}}_{\mathcal{P}_\mathcal{S}} &:= \int_{\mathcal{P}_\mathcal{S}} \boldsymbol{x} \times \rho\big(\boldsymbol{x},t\big)\boldsymbol{v}\big(\boldsymbol{x},t\big)\, dv \,, \\ \boldsymbol{\mathcal{M}}_{\mathcal{P}_\mathcal{S}} &:= \int_{\mathcal{P}_\mathcal{S}} \big[\boldsymbol{x} \times \rho\big(\boldsymbol{x},t\big)\boldsymbol{\gamma}\big(\boldsymbol{x},t\big) + \rho\boldsymbol{\Omega}\big(\boldsymbol{x}\big)\big]\, dv + \int_{\partial\mathcal{P}_\mathcal{S}} \boldsymbol{x} \times \boldsymbol{t}\big(\boldsymbol{x},t\big)\, da \,, \end{aligned} \tag{2.107}$$

In $(2.107)_1$, the time rate of change of angular momentum can then be expressed as

$$\frac{d}{dt}\Big[\int_{\mathcal{P}_\mathcal{S}} \boldsymbol{x} \times \rho\, \boldsymbol{v}\, dv\Big] = \int_{\mathcal{P}_\mathcal{S}} \dot{\boldsymbol{x}} \times \rho\, \boldsymbol{v}\, dv + \int_{\mathcal{P}_\mathcal{S}} \boldsymbol{x} \times \rho\, \dot{\boldsymbol{v}}\, dv \tag{2.108}$$

Since $\dot{\boldsymbol{x}} = \boldsymbol{v}$ and $\boldsymbol{v} \times \boldsymbol{v} = \boldsymbol{0}$, then, the first part of the right-hand side of (2.108) drops out and it becomes

$$\frac{d}{dt}\Big[\int_{\mathcal{P}_\mathcal{S}} \boldsymbol{x} \times \rho\, \boldsymbol{v}\, dv\Big] = \int_{\mathcal{P}_\mathcal{S}} \boldsymbol{x} \times \rho\, \dot{\boldsymbol{v}}\, dv \,. \tag{2.109}$$

The cross product can be written in indicial form as

$$\boldsymbol{a} \times \boldsymbol{b} := \epsilon_{ijk} a_j b_k \,, \tag{2.110}$$

where ϵ_{ijk} is *the permutation symbol* or *the Levi-Civita symbol* defined as

$$\epsilon_{ijk} = \begin{cases} 1 & : \quad \text{even permutation} \,, \\ -1 & : \quad \text{odd permutation} \,, \\ 0 & : \quad \text{double index} \;. \end{cases} \tag{2.111}$$

Combining (2.35), (2.110), and (2.111), the last term in (2.107) can be written in

indicial form as

$$\begin{aligned}\int_{\partial\mathcal{P}_\mathcal{S}} \boldsymbol{x}\times\boldsymbol{t}\big(\boldsymbol{x},t\big)\,da &= \int_{\partial\mathcal{P}_\mathcal{S}} \epsilon_{ijk}x_jt_k\,da\,,\\ &= \int_{\partial\mathcal{P}_\mathcal{S}} \epsilon_{ijk}x_j\sigma_{kl}n_l\,da\,,\\ &= \int_{\mathcal{P}_\mathcal{S}} \frac{\partial\big(\epsilon_{ijk}x_j\sigma_{kl}\big)}{\partial x_l}\,dv\,,\\ &= \int_{\mathcal{P}_\mathcal{S}} \epsilon_{ijk}\sigma_{kj}\,dv + \int_{\mathcal{P}_\mathcal{S}} \epsilon_{ijk}x_j\frac{\partial\sigma_{kl}}{\partial x_l}\,dv\,.\end{aligned} \tag{2.112}$$

Hence, $(2.107)_2$, (2.109), and (2.112) together yields

$$\int_{\mathcal{P}_\mathcal{S}} \boldsymbol{x}\times\big[\rho\dot{\boldsymbol{v}} - \text{div}\,\big(\boldsymbol{\sigma}\big) - \rho\boldsymbol{\gamma}\big]dv + \int_{\mathcal{P}_\mathcal{S}} \rho\boldsymbol{\Omega}\big(\boldsymbol{x}\big)\,dv = \int_{\mathcal{P}_\mathcal{S}} \epsilon_{ijk}\sigma_{kj}dv\,. \tag{2.113}$$

The first term on the left-hand side of (2.113) vanishes identically due to the balance of linear momentum (2.102). Then, (2.113) simplifies to

$$\int_{\mathcal{P}_\mathcal{S}} \rho\Omega_i\,dv = \int_{\mathcal{P}_\mathcal{S}} \epsilon_{ijk}\sigma_{kj}dv\,. \tag{2.114}$$

It is known that $\epsilon_{ijk}\epsilon_{imn} = \delta_{jm}\delta_{kn} - \delta_{jn}\delta_{km}$. Using this identity in the local form of (2.114), we end up with

$$\begin{aligned}\frac{1}{2}\rho\epsilon_{imn}\Omega_i = \frac{1}{2}\epsilon_{imn}\epsilon_{ijk}\sigma_{kj} = \frac{1}{2}\big(\sigma_{mn} - \sigma_{nm}\big)\,,\\ \rho\omega_{mn} = \text{skew}\big(\sigma_{mn}\big)\end{aligned} \tag{2.115}$$

where $\boldsymbol{\omega}$ is the skew-symmetric tensor of the mechanical Cauchy stress and using the definition in (2.68), it can be written as $\rho\boldsymbol{\omega} = \boldsymbol{g}^{-1}\boldsymbol{e}\otimes\boldsymbol{p}$. Moreover, considering (2.104), the skew symmetric part of electric Maxwell stress can be written as

$$\text{skew}\big(\boldsymbol{\sigma}^e\big) = \text{skew}\big(\boldsymbol{g}^{-1}\boldsymbol{e}\otimes\boldsymbol{p}\big) = -\text{skew}\big(\boldsymbol{p}\otimes\boldsymbol{g}^{-1}\boldsymbol{e}\big) = -\rho\boldsymbol{\omega}\,. \tag{2.116}$$

Consequently, skew-symmetric part of total Cauchy stress can be denoted as

$$\text{skew}\big(\overline{\boldsymbol{\sigma}}\big) = \text{skew}\big(\boldsymbol{\sigma} + \boldsymbol{\sigma}^e\big) = \boldsymbol{0}\,. \tag{2.117}$$

In other words, the total Cauchy stres is symmetric whereas mechanical part of the total Cauchy stress is not [9].

2.2.6.4 Balance of Energy

The balance of energy or *the first law of thermodynamics* dictates that the time rate of change of the total energy $\mathcal{E}_{\mathcal{P}_S}$, which is the sum of kinetic energy, i.e. $\mathcal{K}_{\mathcal{P}_S}$, and internal energy, that is, $\mathcal{U}_{\mathcal{P}_S}$, is equal to the summation of mechanical power, $\mathcal{P}_{\mathcal{P}_S}$, and the thermal power, $\mathcal{Q}_{\mathcal{P}_S}$ such that

$$\frac{\partial}{\partial t}\Big[\mathcal{K}_{\mathcal{P}_S} + \mathcal{U}_{\mathcal{P}_S}\Big] = \mathcal{P}_{\mathcal{P}_S} + \mathcal{Q}_{\mathcal{P}_S}\,, \tag{2.118}$$

where

$$\begin{aligned}
\mathcal{K}_{\mathcal{P}_S} &:= \int_{\mathcal{P}_S} \frac{1}{2}\rho \boldsymbol{v}\cdot\boldsymbol{g}\boldsymbol{v} dv\,,\\
\mathcal{U}_{\mathcal{P}_S} &:= \int_{\mathcal{P}_S} \rho e dv\,,\\
\mathcal{P}_{\mathcal{P}_S} &:= \int_{\mathcal{P}_S} \rho\boldsymbol{\gamma}\cdot\boldsymbol{g}\boldsymbol{v}\; dv + \int_{\partial\mathcal{P}_S} \boldsymbol{t}\cdot\boldsymbol{g}\boldsymbol{v}\; da\,,\\
\mathcal{Q}_{\mathcal{P}_S} &:= \int_{\mathcal{P}_S} \rho r\; dv - \int_{\partial\mathcal{P}_S} \boldsymbol{q}\; da
\end{aligned} \tag{2.119}$$

where e is the internal energy density, r is the total energy supply such that $r = r^m + r^e$, and $\boldsymbol{q}$ is the heat flux vector such that $h = \boldsymbol{q}\cdot\boldsymbol{n}$ for the Cauchy-type expression.

In $(2.119)_3$, employing the Cauchy's theorem and the divergence theorem respectively, the mechanical power expression becomes

$$\begin{aligned}
\int_{\mathcal{P}_S} \rho\boldsymbol{\gamma}\cdot\boldsymbol{g}\boldsymbol{v}\; dv + \int_{\partial\mathcal{P}_S} \boldsymbol{t}\cdot\boldsymbol{g}\boldsymbol{v}\; da &:= \int_{\mathcal{P}_S} \rho\gamma^i g_{ij} v^j dv + \int_{\partial\mathcal{P}_S} t^i g_{ij} v^j da\,,\\
&= \int_{\mathcal{P}_S} \rho\gamma^i g_{ij} v^j dv + \int_{\partial\mathcal{P}_S} \sigma^{ik} n_k\, g_{ij} v^j da\,,\\
&= \int_{\mathcal{P}_S} \rho\gamma^i g_{ij} v^j dv + \int_{\mathcal{P}_S} \frac{\partial\big(\sigma^{ik}\, g_{ij} v^j\big)}{\partial\big(x^k\big)} dv\,,\\
&= \int_{\mathcal{P}_S} \rho\gamma^i g_{ij} v^j dv + \int_{\mathcal{P}_S} \frac{\partial\big(\sigma^{ik}\big)}{\partial\big(x^k\big)}\, g_{ij} v^j dv\\
&\quad + \int_{\mathcal{P}_S} \sigma^{ik}\, g_{ij} \frac{\partial\big(v^j\big)}{\partial\big(x^k\big)} dv\,,\\
\int_{\mathcal{P}_S} \rho\boldsymbol{\gamma}\cdot\boldsymbol{g}\boldsymbol{v}\; dv + \int_{\partial\mathcal{P}_S} \boldsymbol{t}\cdot\boldsymbol{g}\boldsymbol{v}\; da &= \int_{\mathcal{P}_S} \rho\boldsymbol{\gamma}\cdot\boldsymbol{g}\boldsymbol{v}\; dv + \int_{\mathcal{P}_S} \operatorname{div}\big(\boldsymbol{\sigma}\big)\cdot\boldsymbol{g}\boldsymbol{v}\; dv\\
&\quad + \int_{\mathcal{P}_S} \boldsymbol{\sigma} : \boldsymbol{g}\boldsymbol{l}\; dv\,.
\end{aligned} \tag{2.120}$$

Moreover, the time rate of change of the kinetic and internal energies will be presented as follows

$$\frac{\partial}{\partial t}\Big[\mathcal{K}_{\mathcal{P}_S} + \mathcal{U}_{\mathcal{P}_S}\Big] = \int_{\mathcal{P}_S} \rho\dot{\boldsymbol{v}} \cdot \boldsymbol{g}\boldsymbol{v} dv + \int_{\mathcal{P}_S} \rho\dot{e} dv \tag{2.121}$$

Combining (2.119), (2.120), and (2.121) along with $h = \boldsymbol{q} \cdot \boldsymbol{n}$, the first law of thermodynamics can be written as

$$\begin{aligned}
\int_{\mathcal{P}_S} \rho\dot{\boldsymbol{v}} \cdot \boldsymbol{g}\boldsymbol{v} dv + \int_{\mathcal{P}_S} \rho\dot{e} dv = &\int_{\mathcal{P}_S} \rho\boldsymbol{\gamma} \cdot \boldsymbol{g}\boldsymbol{v}\, dv + \int_{\mathcal{P}_S} \text{div}\left(\boldsymbol{\sigma}\right) \cdot \boldsymbol{g}\boldsymbol{v}\, dv \\
&+ \int_{\mathcal{P}_S} \boldsymbol{\sigma} : \boldsymbol{g}\boldsymbol{l}\, dv + \int_{\mathcal{P}_S} \rho r\, dv \\
&- \int_{\mathcal{P}_S} \text{div}\left(\boldsymbol{q}\right) dv \\
\int_{\mathcal{P}_S} \boldsymbol{g}\boldsymbol{v}\big[\rho\dot{\boldsymbol{v}} - \text{div}\left(\boldsymbol{\sigma}\right) - \rho\boldsymbol{\gamma}\big] dv + \int_{\mathcal{P}_S} \rho\dot{e} dv = &- \int_{\mathcal{P}_S} \text{div}\left(\boldsymbol{q}\right) dv \\
&+ \int_{\mathcal{P}_S} \boldsymbol{\sigma} : \boldsymbol{g}\boldsymbol{l}\, dv + \int_{\mathcal{P}_S} \rho r\, dv\,.
\end{aligned} \tag{2.122}$$

Rearranging (2.122) considering (2.102), the simplified expression for the balance of energy can be obtained as

$$\int_{\mathcal{P}_S} \rho\dot{e} dv = -\int_{\mathcal{P}_S} \text{div}\left(\boldsymbol{q}\right) dv + \int_{\mathcal{P}_S} \boldsymbol{\sigma} : \boldsymbol{g}\boldsymbol{l}\, dv + \int_{\mathcal{P}_S} \rho r\, dv \tag{2.123}$$

The local form of (2.123) can be written as:

$$\rho\dot{e} = -\text{div}\left(\boldsymbol{q}\right) + \boldsymbol{\sigma} : \boldsymbol{g}\boldsymbol{l} + \rho r\,, \tag{2.124}$$

where $\rho r = \rho r^m + \rho r^e$ and $\rho r^e = \rho\boldsymbol{e} \cdot \frac{d}{dt}\left(\frac{\boldsymbol{p}}{\rho}\right)$ obtained from the work done by the electric forces on an electric dipole and the Taylor's series expansion [9, 15].

2.2.6.5 Balance of Entropy

This balance equation is also known as *the second law of thermodynamics*, and comparing with the other balance expressions, it states that the internal entropy production rate is always *non-negative*. Entropy can be defined as *disorderness* or *the measure of disorder*. The balance of entropy can be expressed as

$$\Gamma_{\mathcal{P}_S} = \dot{\mathcal{H}}_{\mathcal{P}_S} - \dot{\mathcal{S}}_{\mathcal{P}_S} \geq 0\,. \tag{2.125}$$

where

$$
\begin{aligned}
\Gamma_{\mathcal{P}_\mathcal{S}} &:= \int_{\mathcal{P}_\mathcal{S}} \rho\gamma \, dv \,, \\
\dot{\mathcal{H}}_{\mathcal{P}_\mathcal{S}} &:= \int_{\mathcal{P}_\mathcal{S}} \rho\dot{\eta} \, dv \,, \\
\dot{\mathcal{S}}_{\mathcal{P}_\mathcal{S}} &:= \int_{\mathcal{P}_\mathcal{S}} \rho \, \frac{r}{\theta} \, dv - \int_{\partial\mathcal{P}_\mathcal{S}} \frac{\boldsymbol{q}}{\theta} \cdot \boldsymbol{n} \, \theta \, da \,,
\end{aligned}
\tag{2.126}
$$

where $\rho r = \rho r^m + \rho r^e$ as in (2.124). In (2.125) and (2.126), $\dot{\mathcal{H}}_{\mathcal{P}_\mathcal{S}}$ denotes the rate of entropy change and $\dot{\mathcal{S}}_{\mathcal{P}_\mathcal{S}}$ is defined as the entropy power. On the left-hand side of (2.125), the term $\Gamma_{\mathcal{P}_\mathcal{S}}$ stand for the rate of entropy production. Then, the combination of (2.125) and (2.126) will provide as the second law of thermodynamics in an integral forms; that is,

$$
\begin{aligned}
&\int_{\mathcal{P}_\mathcal{S}} \rho \, \dot{\eta} \, dv \geq \int_{\mathcal{P}_\mathcal{S}} \rho \, \frac{r}{\theta} \, dv - \int_{\partial\mathcal{P}_\mathcal{S}} \frac{\boldsymbol{q}}{\theta} \cdot \boldsymbol{n} \, \theta \, da \,, \\
&\int_{\mathcal{P}_\mathcal{S}} \rho\gamma \, dv := \int_{\mathcal{P}_\mathcal{S}} \rho\dot{\eta} \, dv - \int_{\mathcal{P}_\mathcal{S}} \rho \, \frac{r}{\theta} \, dv + \int_{\partial\mathcal{P}_\mathcal{S}} \frac{\boldsymbol{q} \cdot \boldsymbol{n}}{\theta} \, da \,.
\end{aligned}
\tag{2.127}
$$

The last term in $(2.127)_2$ is transferred into a volume integral by

$$
\begin{aligned}
\int_{\partial\mathcal{P}_\mathcal{S}} \frac{\boldsymbol{q} \cdot \boldsymbol{n}}{\theta} \, da &= \int_{\mathcal{P}_\mathcal{S}} \operatorname{div}\left(\frac{\boldsymbol{q}}{\theta}\right) dv \,, \\
&= \int_{\mathcal{P}_\mathcal{S}} \frac{1}{\theta} \operatorname{div} \boldsymbol{q} \, dv - \int_{\mathcal{P}_\mathcal{S}} \frac{1}{\theta^2} \, \boldsymbol{q} \cdot \nabla_{\boldsymbol{x}} \theta \, dv
\end{aligned}
\tag{2.128}
$$

Employing (2.128) in $(2.127)_2$, we arrive at

$$
\int_{\mathcal{P}_\mathcal{S}} \rho \, \gamma \, dv := \int_{\mathcal{P}_\mathcal{S}} \rho\dot{\eta} \, dv - \int_{\mathcal{P}_\mathcal{S}} \rho \, \frac{r}{\theta} \, dv + \int_{\mathcal{P}_\mathcal{S}} \frac{1}{\theta} \operatorname{div} \boldsymbol{q} \, dv - \int_{\mathcal{P}_\mathcal{S}} \frac{1}{\theta^2} \, \boldsymbol{q} \cdot \nabla_{\boldsymbol{x}} \theta \, dv \tag{2.129}
$$

The local form of (2.129) yields

$$
\rho\gamma := \rho\dot{\eta} - \rho \, \frac{r}{\theta} + \frac{1}{\theta} \operatorname{div} \boldsymbol{q} - \frac{1}{\theta^2} \, \boldsymbol{q} \cdot \nabla_{\boldsymbol{x}} \theta \geq 0 \,. \tag{2.130}
$$

The latter is called *the Clausius-Duhem Inequality*. It is obtained from (2.124) that

$$
\frac{1}{\theta}\big(\rho r^m - \operatorname{div} \boldsymbol{q}\big) = \frac{1}{\theta}\big(\rho\dot{e} - \boldsymbol{\sigma} : \boldsymbol{g}\boldsymbol{l} - \rho r^e\big) \tag{2.131}
$$

Next, an alternative form of *the Clausius-Duhem Inequality* is specified as

$$
\rho\gamma := \rho\dot{\eta} - \frac{1}{\theta}\big(\rho\dot{e} - \boldsymbol{\sigma} : \boldsymbol{g}\boldsymbol{l} - \rho r^e\big) - \frac{1}{\theta^2} \, \boldsymbol{q} \cdot \nabla_{\boldsymbol{x}} \theta \geq 0 \,. \tag{2.132}
$$

Besides, the spatial dissipation, $\rho\mathcal{D}$ is defined as the product of entropy production rate and the absolute temperature. In other words, $\rho\mathcal{D} := \rho\theta\gamma$. Thus, the Clausius-Duhem inequality can be rewritten in terms of spatial dissipation.

$$\rho\mathcal{D} := \rho\theta\dot{\eta} - \rho\dot{e} + \boldsymbol{\sigma} : \boldsymbol{g}\boldsymbol{l} - \rho r^e - \frac{1}{\theta}\,\boldsymbol{q}\cdot\nabla_{\boldsymbol{x}}\theta \geq 0 \tag{2.133}$$

Spatial dissipation can be divided into two parts, namely the local dissipation ($\rho\mathcal{D}_{loc}$) or *the Clausius-Planck Inequality* (*CPI*) and the conductive dissipation ($\rho\mathcal{D}_{con}$) or *Fourier Inequality* (*FI*) defined as

$$\begin{aligned} \rho\mathcal{D}_{loc} &:= \rho\theta\dot{\eta} - \rho\dot{e} + \boldsymbol{\sigma} : \boldsymbol{g}\boldsymbol{l} - \rho r^e\,, \\ \rho\mathcal{D}_{con} &:= -\frac{1}{\theta}\,\boldsymbol{q}\cdot\nabla_{\boldsymbol{x}}\theta\,, \end{aligned} \tag{2.134}$$

The Lagrangian form of the spatial dissipations in the Eulerian configuration can be written employing the *pull-back* expressions as

$$\begin{aligned} \rho_0\mathcal{D}_{loc} &:= \rho_0\theta\dot{\eta} - \rho_0\dot{e} + \boldsymbol{g}\boldsymbol{P} : \dot{\boldsymbol{F}} - \rho_0 R^e\,, \\ \rho_0\mathcal{D}_{con} &:= -\frac{1}{\theta}\,\boldsymbol{Q}\cdot\nabla_{\boldsymbol{X}}\theta\,, \end{aligned} \tag{2.135}$$

In (2.135), the internal energy can be replaced by the Helmholtz free energy defined as $\Psi = e - \theta\eta$ using *Legendre transformation*. Consequently, an alternative form of Clausius-Planck inequality is obtained

$$\rho\mathcal{D}_{loc} := \boldsymbol{\sigma} : \boldsymbol{g}\boldsymbol{l} - \rho\eta\dot{\theta} - \rho\dot{\Psi} - \rho r^e\,, \tag{2.136}$$

For the isothermal case ($\theta = constant$), and by the definition of energy supply from electric effect (ρr^e) defined in [15], the Clausius-Planck inequality turns out to be in the Lagrangian form as

$$\rho_0\mathcal{D}_{loc} := \overline{\boldsymbol{\tau}} : \frac{1}{2}\mathcal{L}_{\boldsymbol{v}}\boldsymbol{g} - \rho_0\dot{\Psi} - \tilde{\boldsymbol{d}} : \mathcal{L}_{\boldsymbol{v}}\boldsymbol{e}\,, \tag{2.137}$$

where $\overline{\boldsymbol{\tau}}$ is the total Kirchhoff stress. It can be expressed as $\overline{\boldsymbol{\tau}} = \boldsymbol{\tau} + \boldsymbol{\tau}^e$. Until the end of this chapter, total stress expressions are shown by $\overline{(\blacksquare)}$. Using the *Coleman's Exploitation Method* generated by [49], from the principles of local action and equipresence, the Helmholtz free energy can be defined as

$$\Psi = \hat{\Psi}\big(\boldsymbol{g}; \boldsymbol{F}, \boldsymbol{e}\big)\,. \tag{2.138}$$

As a result, the rate form of the Helmholtz free energy function is defined as

$$\dot{\Psi} = 2\partial_{\boldsymbol{g}}\Psi : \frac{1}{2}\mathcal{L}_{\boldsymbol{v}}\boldsymbol{g} + \partial_{\boldsymbol{e}}\Psi \cdot \mathcal{L}_{\boldsymbol{v}}\boldsymbol{e}\,. \tag{2.139}$$

When (2.139) is inserted into (2.137), the electro-mechanical constitutive equations are obtained through the work conjugate variables

$$\rho_0\mathcal{D}_{loc} := \big[\overline{\boldsymbol{\tau}} - 2\rho_0\partial_{\boldsymbol{g}}\Psi\big(\boldsymbol{g};\boldsymbol{F},\boldsymbol{e}\big)\big] : \frac{1}{2}\mathcal{L}_{\boldsymbol{v}}\boldsymbol{g} + \big[\tilde{\boldsymbol{d}} + \rho_0\partial_{\boldsymbol{e}}\Psi\big(\boldsymbol{g};\boldsymbol{F},\boldsymbol{e}\big)\big] : \mathcal{L}_{\boldsymbol{v}}\boldsymbol{e} \geq 0\,. \tag{2.140}$$

The equality in (2.140) holds for arbitrary rates, in other words, $\mathcal{L}_{\boldsymbol{v}}\boldsymbol{g} \neq \boldsymbol{0}$ and $\mathcal{L}_{\boldsymbol{v}}\boldsymbol{e} \neq \boldsymbol{0}$. Hence,

$$\begin{aligned} \overline{\boldsymbol{\tau}}\big(\boldsymbol{g};\boldsymbol{F},\boldsymbol{e}\big) &= 2\rho_0\partial_{\boldsymbol{g}}\Psi\big(\boldsymbol{g};\boldsymbol{F},\boldsymbol{e}\big)\,, \\ \tilde{\boldsymbol{d}}\big(\boldsymbol{g};\boldsymbol{F},\boldsymbol{e}\big) &= -\rho_0\partial_{\boldsymbol{e}}\Psi\big(\boldsymbol{g};\boldsymbol{F},\boldsymbol{e}\big)\,. \end{aligned} \tag{2.141}$$

Employing *the push-forward* and *the pull-back* operations, the other dual variables can be obtained using the commutative diagram defined in the previous sections. To illustrate, mechanical stress power $\mathfrak{P}_{mec}$ per unit reference volume is defined as

$$\begin{aligned} \mathfrak{P}_{mec} := \overline{\boldsymbol{\tau}} : \frac{1}{2}\mathcal{L}_{\boldsymbol{v}}\boldsymbol{g} &= \overline{\boldsymbol{\tau}} : \frac{1}{2}\big(\boldsymbol{F}^{-T}\dot{\boldsymbol{C}}\boldsymbol{F}^{-1}\big)\,, \\ &= \boldsymbol{F}^{-1}\overline{\boldsymbol{\tau}}\boldsymbol{F}^{-T} : \frac{1}{2}\dot{\boldsymbol{C}}\,, \\ &= \overline{\boldsymbol{S}} : \frac{1}{2}\dot{\boldsymbol{C}} \end{aligned} \tag{2.142}$$

Therefore, the second Piola-Kirchhoff stress tensor and the right Cauchy-Green deformation tensor are work conjugates. Other dual variables are the first Piola-Kirchhoff stress tensor and the deformation gradient. In order to show the duality, (2.142) is elaborated as

$$\begin{aligned} \overline{\boldsymbol{S}} : \frac{1}{2}\dot{\boldsymbol{C}} := \overline{\boldsymbol{S}} : \frac{1}{2}\big(\dot{\boldsymbol{F}}^T\boldsymbol{g}\boldsymbol{F} + \boldsymbol{F}^T\boldsymbol{g}\dot{\boldsymbol{F}}\big) &= \overline{\boldsymbol{S}} : \frac{1}{2}\big(\dot{\boldsymbol{F}}^T\boldsymbol{g}\boldsymbol{F}\big) + \overline{\boldsymbol{S}} : \frac{1}{2}\big(\boldsymbol{F}^T\boldsymbol{g}\dot{\boldsymbol{F}}\big)\,, \\ &= \overline{\boldsymbol{S}}^T : \frac{1}{2}\big(\boldsymbol{F}^T\boldsymbol{g}\dot{\boldsymbol{F}}\big)^T + \overline{\boldsymbol{S}} : \frac{1}{2}\big(\boldsymbol{F}^T\boldsymbol{g}\dot{\boldsymbol{F}}\big)\,, \\ &= \overline{\boldsymbol{S}} : \big(\boldsymbol{F}^T\boldsymbol{g}\dot{\boldsymbol{F}}\big)\,, \\ &= \boldsymbol{g}\boldsymbol{F}\overline{\boldsymbol{S}} : \dot{\boldsymbol{F}}\,, \\ &= \overline{\boldsymbol{P}} : \dot{\boldsymbol{F}}\,. \end{aligned} \tag{2.143}$$

Finally, the work conjugate variables can be determined by considering the mechanical stress power and *push-forward* and *pull-back* operations. Final form of mechanical stress power is

$$\mathfrak{P}_{mec} := \overline{\boldsymbol{\tau}} : \frac{1}{2}\mathcal{L}_{\boldsymbol{v}}\big(\boldsymbol{g}\big) = \overline{\boldsymbol{S}} : \frac{1}{2}\dot{\boldsymbol{C}} = \overline{\boldsymbol{P}} : \dot{\boldsymbol{F}}\,. \tag{2.144}$$

Similarly, the electrical power denoted as $\mathfrak{P}_{elec}$ can be obtained by

$$\begin{aligned} \mathfrak{P}_{elec} := -\tilde{\boldsymbol{d}} : \mathcal{L}_{\boldsymbol{v}}\boldsymbol{e} &= -\tilde{\boldsymbol{d}} : \boldsymbol{F}\dot{\boldsymbol{E}}\,, \\ &= -\boldsymbol{F}^T\tilde{\boldsymbol{d}} : \dot{\boldsymbol{E}}\,, \\ &= -\boldsymbol{D} : \dot{\boldsymbol{E}}\,. \end{aligned} \tag{2.145}$$

Therefore, electrical power can be written for each configuration

$$\mathfrak{P}_{elec} := -\tilde{\boldsymbol{d}} : \mathcal{L}_{\boldsymbol{v}}\boldsymbol{e} = -\boldsymbol{D} : \dot{\boldsymbol{E}}\,. \tag{2.146}$$

The mechanical stress power (2.144) and the electrical power (2.146) are useful equations for the constitutive relations. It is important to state that the mechanical stress and the electrical displacement are dependent upon each other in terms of the nonlinear deformation map and the gradient of the electric potential, or electric field. Using the state variables, electro-mechanical interactions can be determined for each configurations. However, the equations for the Eulerian configuration are used for the rest of this work.

CHAPTER 3

CONSTITUTIVE EQUATIONS

The fundamental equations of continuum mechanics such as kinematics, balance equations, and stress expressions apply to all materials. However, the material behavior depends on the type of material at hand. Hence, this part of the thesis consists of the specific material models. Material models are the subject that is generated mathematically to represent the real behavior of material. Some of the materials may undergo small deformations whereas some other exhibit finite deformations. Among them, hyperelastic material behavior is generally employed for the materials undergoing finite deformations. According to [47] and many others, in solid mechanics, the hyperelasticity theory requires the Helmholtz free energy to model the characteristics of materials. The Helmholtz free energy function is defined as the energy per unit volume and it depends on the state variables. For the coupled electro-mechanical interactions, the state is defined as

$$\text{State}\big(\boldsymbol{X}, t\big) := \Big\{\boldsymbol{\varphi}\big(\boldsymbol{X}, t\big), \phi\big(\boldsymbol{X}, t\big)\Big\}\,. \tag{3.1}$$

It is important to point out for hyperelasticity theory that constitutive equations can be considered as functions of state variables. Accordingly, the electro-mechanical Helmholtz free energy density is a function of the spatial metric tensor $\boldsymbol{g}$, the deformation gradient $\boldsymbol{F}$, and the electric field $\boldsymbol{e}$ and can be written as

$$\Psi\big(\boldsymbol{g}; \boldsymbol{F}, \boldsymbol{e}\big) := \Psi^{m}\big(\boldsymbol{g}; \boldsymbol{F}\big) + \Psi^{em}\big(\boldsymbol{g}; \boldsymbol{F}, \boldsymbol{e}\big)\,, \tag{3.2}$$

where Ψ^{m} is characterized as the mechanical part and Ψ^{em} is the electro-mechanical part of the total free energy density function, respectively. It is important to note that the Helmholtz free energy function shows the normalization condition, i.e. $\Psi\big(\mathbf{1}\big) = 0$

at the stress-free or reference state, and $\Psi\big(\boldsymbol{g};\boldsymbol{F},\boldsymbol{e}\big) \geq 0$ when it is under some electro-mechanical deformations.

It must be considered that the rigid body at its reference state is exposed to a rigid body translation $\boldsymbol{c}$ and a rotation $\boldsymbol{Q}$ such that the material point $\boldsymbol{X}$ is mapped to $\boldsymbol{X}^{+} = \boldsymbol{c}+\boldsymbol{Q}\boldsymbol{X}$ and $\forall \boldsymbol{Q} \in G \subset SO\big(3\big)$. According to [9, 29, 46, 47] and many others, the material is called *isotropic* provided that the Helmholtz free energy function at the reference configuration is equal to free energy function when it is under rigid body translation and rotation. To figure out, Helmholtz free energy functions can be rewritten as

$$\Psi^{m}\big(\boldsymbol{g};\boldsymbol{F}\big) = \Psi^{m}\big(\boldsymbol{g};\boldsymbol{b}\big)\,, \tag{3.3}$$

and the special orthogonal group is defined as:

$$G \equiv SO\big(3\big) = \big\{\boldsymbol{Q}|\boldsymbol{Q}\boldsymbol{Q}^{T} = \mathbf{1} \wedge \det\boldsymbol{Q} = +1\big\}\,. \tag{3.4}$$

Due to symmetry conditions, the Helmholtz free energy function can be written in terms of eigenvalues (λ_i for $i = 1, 2, 3$) or the principle invariants of the left Cauchy-Green tensor in the Eulerian configuration (I_i for $i = 1, 2, 3$) for isotropic response.

$$\Psi = \tilde{\Psi}\big(\lambda_1, \lambda_2, \lambda_3\big), \quad \text{or} \quad \Psi = \tilde{\Psi}\big(I_1, I_2, I_3\big) \tag{3.5}$$

Some of the materials like foams show compressible nature whereas some others, such as rubberlike materials show incompressible or quasi-incompressible behavior. To be more specific, in compressible materials, volume changes are observed in considerable amounts such that $J = \det\boldsymbol{F} \neq 1$. Nevertheless, like most of the rubbers, the volume changes of such materials are not very much effective in incompressible materials, i.e. $J = \det\boldsymbol{F} = 1$. Consequently, the deformation gradient can be multiplicatively decomposed into the volumetric (spherical) and the isochoric (unimodular) part. It can be shown as

$$\boldsymbol{F} := \boldsymbol{F}_{vol}\boldsymbol{F}_{iso}, \quad \text{where} \quad \boldsymbol{F}_{vol} := J^{\frac{1}{3}}\mathbf{1} \quad \text{and} \quad \boldsymbol{F}_{iso} := J^{-\frac{1}{3}}\boldsymbol{F}\,. \tag{3.6}$$

The volumetric part of the deformation gradient $\boldsymbol{F}_{vol}$ is responsible for the volume changing and shape preserving deformations,whereas the isochoric part $\boldsymbol{F}_{iso}$ indi-

cates the shape changing and volume preserving deformations. Similarly, the isochoric part of the right and left Cauchy-Green deformation tensors can be written as

$$\begin{aligned} \boldsymbol{C}_{iso} &:= J^{-\frac{1}{3}}\boldsymbol{F}^T\boldsymbol{g}J^{-\frac{1}{3}}\boldsymbol{F} = J^{-\frac{2}{3}}\boldsymbol{C}\,, \\ \boldsymbol{b}_{iso} &:= J^{-\frac{1}{3}}\boldsymbol{F}\boldsymbol{G}^{-1}J^{-\frac{1}{3}}\boldsymbol{F}^T = J^{-\frac{2}{3}}\boldsymbol{b}\,. \end{aligned} \tag{3.7}$$

In addition, in the light of this information and using (3.2), the Helmholtz free energy function can be additively decomposed into three for the coupled electro-mechanical response as: mechanical-volumetric, mechanical-isochoric, and coupled electro-mechanical free energy functions

$$\Psi\big(\boldsymbol{g};\boldsymbol{F},\boldsymbol{e}\big) := U\big(J\big) + \overline{\Psi}\big(\boldsymbol{g};\boldsymbol{F}_{iso}\big) + \Psi^{em}\big(\boldsymbol{g};\boldsymbol{F},\boldsymbol{e}\big)\,. \tag{3.8}$$

The Helmholtz free energy functions are defined for different material models. Among them the Neo-Hookean model is often employed for the mechanical part. For the electro-mechanical part of the total free energy function, different functions are proposed. While some researchers consider the mechanical effects to explain the electromechanical part of the Helmholtz free energy, some others think this may not be the case [18]. To be more specific, some of the researchers explain relative permittivity as deformation-dependent [10, 18] and some others indicate that the relative permittivity is constant [32]. Two alternative models, which are proposed by [10] and [32], are provided for the electro-mechanical free energy functions.

To study the pattern transformation behavior, the material is exposed to the compression. With the effect of periodic boundary conditions, periodicity changes when the critical loading is reached. The experimental investigations is carried out by [6] and the numerical analysis are went through [6, 4, 5]. Thus, in Model III, the Helmholtz free energy function that is proposed in [6, 4, 5] are provided to determine the stress and moduli terms which are required to obtain the residual vector and consisten tangent matrice.

3.1 Model I

For the first model problem, the electro-mechanical free energy function proposed by [10] for VHB 4910 as a dielectric elastomer is considered. It suggests that the

Helmholtz free energy density function in the Lagrangian configuration is decomposed as:

$$
\begin{aligned}
\Psi\big(J, \boldsymbol{C}_{iso}, \boldsymbol{E}\big) &:= U\big(J\big) + \overline{\Psi}\big(\boldsymbol{C}_{iso}\big) + \Psi^{em}\big(J, \boldsymbol{C}_{iso}, \boldsymbol{E}\big)\,, \\
U\big(J\big) &:= \frac{\kappa}{4}\big(J^2 - 1 - 2\ln J\big)\,, \\
\overline{\Psi}\big(\boldsymbol{C}_{iso}\big) &:= \frac{\mu}{2}\big(\boldsymbol{C}_{iso} : \boldsymbol{G}^{-1} - 3\big)\,, \\
\Psi^{em}\big(J, \boldsymbol{C}_{iso}, \boldsymbol{E}\big) &:= -\frac{1}{2} J\, \epsilon_0 \epsilon_r \boldsymbol{C}^{-1} : \big(\boldsymbol{E} \otimes \boldsymbol{E}\big)\,,
\end{aligned}
\tag{3.9}
$$

where ϵ_0 is the electric permittivity for vacuum and ϵ_r is the relative permittivity. According to [50], the relative permittivity is dependent upon the stretches. [10] provides improvements to the relative permittivity expressions. Consequently, the relative electric permittivity is defined as:

$$
\epsilon_r := c_0\big[1 + c_1\big(\boldsymbol{C} : \boldsymbol{G}^{-1} - 3\big)\big]\,. \tag{3.10}
$$

Similarly, (3.9) and (3.10) can be redefined in the spatial setting as:

$$
\begin{aligned}
\Psi\big(J, \boldsymbol{b}_{iso}, \boldsymbol{e}\big) &:= U\big(J\big) + \overline{\Psi}\big(\boldsymbol{b}_{iso}\big) + \Psi^{em}\big(J, \boldsymbol{b}_{iso}, \boldsymbol{e}\big)\,, \\
U\big(J\big) &:= \frac{\kappa}{4}\big(J^2 - 1 - 2\ln J\big)\,, \\
\overline{\Psi}\big(\boldsymbol{b}_{iso}\big) &:= \frac{\mu}{2}\big(\boldsymbol{b}_{iso} : \boldsymbol{g} - 3\big)\,, \\
\Psi^{em}\big(J, \boldsymbol{g}, \boldsymbol{e}\big) &:= -\frac{1}{2} J\, \epsilon_0 \epsilon_r \boldsymbol{g}^{-1} : \big(\boldsymbol{e} \otimes \boldsymbol{e}\big)\,,
\end{aligned}
\tag{3.11}
$$

where

$$
\epsilon_r := c_0\big[1 + c_1\big(\boldsymbol{b} : \boldsymbol{g} - 3\big)\big]\,. \tag{3.12}
$$

From (3.9) to (3.12), all the material parameters are provided in Table 3.1.

Considering the definitions in (2.141), the Kirchhoff stress tensors obtained from volumetric, isochoric, and electro-mechanical parts of the total free energy function and the electric displacement obtained from the electro-mechanical part of the total free

Table 3.1: Material Properties for Model I

Parameter	Unit	Definition	Value
κ	[MPa]	Bulk Modulus	13.5
μ	[kPa]	Shear Modulus	13.5
ϵ_0	[F/m]	Electric Permittivity of Vacuum	8.854×10^{-12}
c_0	[–]	Relative permittivity coefficient 1	4.68
c_1	[–]	Relative permittivity coefficient 2	-0.0105

energy function per unit reference volume can be expressed for the Model I as

$$\begin{aligned}
\boldsymbol{\tau}_{vol} &:= 2\,\partial_{\boldsymbol{g}} U = \frac{\kappa}{2}\big(J^2 - 1\big)\boldsymbol{g}^{-1}\,, \\
\boldsymbol{\tau}_{iso} &:= 2\,\partial_{\boldsymbol{g}} \overline{\Psi} = \mu \boldsymbol{b}_{iso}\,, \\
\boldsymbol{\tau}^{em} &:= 2\,\partial_{\boldsymbol{g}} \Psi^{em} = -\frac{1}{2}\,J\,\epsilon_0\,\epsilon_r\,\big(\boldsymbol{e}\cdot\boldsymbol{e}\big)\,\boldsymbol{g}^{-1} \\
&\qquad - J\,\epsilon_0\,c_0\,c_1\,\big(\boldsymbol{e}\cdot\boldsymbol{e}\big)\,\boldsymbol{b} \\
&\qquad + J\,\epsilon_0\,\epsilon_r\,\big(\boldsymbol{e}\otimes\boldsymbol{e}\big)\,, \\
\tilde{\boldsymbol{d}} &:= -\partial_{\boldsymbol{e}} \Psi^{em} = J\,\epsilon_0\,\epsilon_r\,\boldsymbol{e}^{\flat}\,,
\end{aligned} \tag{3.13}$$

where $\boldsymbol{e}^{\flat} := \boldsymbol{g}^{-1}\boldsymbol{e}$. The total Kirchhoff stress tensor $\boldsymbol{\tau} := \boldsymbol{\tau}_{vol} + \boldsymbol{\tau}_{iso} + \boldsymbol{\tau}^{em}$ and the electric displacement vector $\tilde{\boldsymbol{d}}$ are employed for the calculation of residual vectors. Nonetheless, the residual vectors are non-linear. Hence, linearization is required to be applied to the residual vectors. Consequently, the mechanical, electrical, and mixed electro-mechanical moduli terms in the Eulerian configuration are defined as

$$\begin{aligned}
\mathbb{c}_{vol} &:= 2\,\partial_{\boldsymbol{g}} \boldsymbol{\tau}_{vol} = 4\,\partial_{\boldsymbol{gg}} U\,, \\
\mathbb{c}_{iso} &:= 2\,\partial_{\boldsymbol{g}} \boldsymbol{\tau}_{iso} = 4\,\partial_{\boldsymbol{gg}} \overline{\Psi}\,, \\
\mathbb{c}^{em} &:= 2\,\partial_{\boldsymbol{g}} \boldsymbol{\tau}^{em} = 4\,\partial_{\boldsymbol{gg}} \Psi^{em}\,, \\
\mathbb{a} &:= 2\,\partial_{\boldsymbol{g}} \tilde{\boldsymbol{d}} = -2\,\partial_{\boldsymbol{ge}} \Psi^{em}\,, \\
\mathbb{b} &:= -\partial_{\boldsymbol{e}} \boldsymbol{\tau}^{em} = -2\,\partial_{\boldsymbol{eg}} \Psi^{em}\,, \\
\mathbb{d} &:= -\partial_{\boldsymbol{e}} \tilde{\boldsymbol{d}} = \partial_{\boldsymbol{ee}} \Psi^{em}\,,
\end{aligned} \tag{3.14}$$

where $\mathbb{a}$ and $\mathbb{b}$ are third-order mixed moduli terms, and $\mathbb{d}$ is second-order electric

moduli. Besides, it can be stated that $\mathbb{a} = \mathbb{b}^T$.

3.2 Model II

In Model II, the electro-mechanical free energy function is defined as indicated in [32]. In this model, [32] do not define the multiplicative split of deformation gradient. Hence, the free energy density function for the Lagrangian configuration is proposed as follows:

$$\begin{aligned}
\Psi(J, \boldsymbol{C}, \boldsymbol{E}) &:= \Psi^m\big(J, \boldsymbol{C}\big) + \Psi^{em}\big(J, \boldsymbol{C}, \boldsymbol{E}\big)\,, \\
\Psi^m\big(J, \boldsymbol{C}\big) &:= \frac{\lambda}{2}\big(\ln J\big)^2 - \mu \ln J + \frac{\mu}{2}\big(\boldsymbol{C} : \boldsymbol{G}^{-1} - 3\big)\,, \\
\Psi^{em}\big(J, \boldsymbol{C}, \boldsymbol{E}\big) &:= \alpha \boldsymbol{G}^{-1} : \big(\boldsymbol{E} \otimes \boldsymbol{E}\big) + \beta \boldsymbol{C}^{-1} : \big(\boldsymbol{E} \otimes \boldsymbol{E}\big) \\
&\quad - \frac{1}{2} J \epsilon_r \boldsymbol{C}^{-1} : \big(\boldsymbol{E} \otimes \boldsymbol{E}\big)
\end{aligned} \tag{3.15}$$

In contrast to Model I, the relative permittivity is independent of deformation. In addition, material coeeficients and their definitions are presented in Table 3.2. The expressions in (3.15) can be transformed into the free energy function in the Eulerian configuration as:

$$\begin{aligned}
\Psi\big(J, \boldsymbol{b}, \boldsymbol{e}\big) &:= \Psi^m\big(J, \boldsymbol{b}\big) + \Psi^{em}\big(J, \boldsymbol{b}, \boldsymbol{e}\big)\,, \\
\Psi^m\big(J, \boldsymbol{b}\big) &:= \frac{\lambda}{2}\big(\ln J\big)^2 - \mu \ln J + \frac{\mu}{2}\big(\boldsymbol{b} : \boldsymbol{g} - 3\big)\,, \\
\Psi^{em}\big(J, \boldsymbol{b}, \boldsymbol{e}\big) &:= \alpha \boldsymbol{b} : \big(\boldsymbol{e} \otimes \boldsymbol{e}\big) + \beta \boldsymbol{g}^{-1} : \big(\boldsymbol{e} \otimes \boldsymbol{e}\big) \\
&\quad - \frac{1}{2} J \epsilon_r \boldsymbol{g}^{-1} : \big(\boldsymbol{e} \otimes \boldsymbol{e}\big)
\end{aligned} \tag{3.16}$$

Likewise, the total Kirchhoff stress tensor $\boldsymbol{\tau} := \boldsymbol{\tau}^m + \boldsymbol{\tau}^{em}$ and the electric displacement vector $\tilde{\boldsymbol{d}}$ can be calculated for Model II as

$$\begin{aligned}
\boldsymbol{\tau}^m := 2\, \partial_{\boldsymbol{g}} \Psi^m &= \big(\lambda \ln J - \mu\big)\boldsymbol{g}^{-1} + \mu \boldsymbol{b}\,, \\
\boldsymbol{\tau}^{em} := 2\, \partial_{\boldsymbol{g}} \Psi^{em} &= \big(J\, \epsilon_r - 2\beta\big)\big(\boldsymbol{e}^\flat \otimes \boldsymbol{e}^\flat\big) \\
&\quad - \frac{1}{2}\, J\, \epsilon_r\, \big(\boldsymbol{e}^\flat \cdot \boldsymbol{e}\big)\boldsymbol{g}^{-1}\,, \\
\tilde{\boldsymbol{d}} := -\partial_{\boldsymbol{e}} \Psi^{em} &= \big(J\, \epsilon_r - 2\, \beta\big)\boldsymbol{e}^\flat - 2\, \alpha \boldsymbol{b}\boldsymbol{e}\,.
\end{aligned} \tag{3.17}$$

(3.17) is necessary for the determination of the residual vectors. For the linearization

Table 3.2: Material Properties for Model II

Parameter	Unit	Definition	Value
λ	[MPa]	Lamé Constant	0.06
μ	[MPa]	Shear Modulus	0.05
ϵ_0	[F/m]	Electric Permittivity of Vacuum	8.854×10^{-12}
ϵ_r	[F/m]	Relative Permittivity	$\left[5\epsilon_0, 1000\epsilon_0\right]$
α	[F/m]	Coefficient 1	$0.2\epsilon_0$
β	[F/m]	Coefficient 2	$2\epsilon_0$

of the coupled electromechanical residual vectors, moduli expressions are required. Hence, coupled electro-mechanical moduli terms can be determined as in (3.14).

3.3 Model III

In this section, the Helmholtz free energy function is defined only for the mechanical state variables ($\Psi\big(J, \boldsymbol{F}\big) = \Psi^m\big(J, \boldsymbol{F}\big)$). For this model problem, the microstructure possess unit cells which are periodically located. Consequently, the state different from the electromechanical state (3.1) can be redefined for the periodic microstructures as

$$\text{State}\big(\boldsymbol{X}, t\big) := \Big\{\boldsymbol{\varphi}\big(\boldsymbol{X}, t\big)\Big\}\,. \tag{3.18}$$

According to [4, 5, 6], the Helmholtz free energy function is provided for Model III in the Lagrangian configuration as

$$\Psi\big(J, \boldsymbol{C}\big) := \frac{\kappa}{2}\big(J-1\big)^2 - 2\,c_1 \ln J + c_1\big(\boldsymbol{C} : \boldsymbol{G}^{-1} - 3\big) + c_2\big(\boldsymbol{C} : \boldsymbol{G}^{-1} - 3\big)^2\,, \tag{3.19}$$

(3.19) is also called a *two-term I_1-based Rivlin model*. The Eulerian counterpart of (3.19) can be expressed as

$$\Psi\big(J, \boldsymbol{b}\big) := \frac{\kappa}{2}\big(J-1\big)^2 - 2\,c_1 \ln J + c_1\big(\boldsymbol{b} : \boldsymbol{g} - 3\big) + c_2\big(\boldsymbol{b} : \boldsymbol{g} - 3\big)^2\,, \tag{3.20}$$

where κ, c_1, and c_2 are material parameters and they are presented in Table 3.3.

Table 3.3: Material Properties for Model III

Parameter	Unit	Definition	Value
κ	[MPa]	Bulk Modulus	55.0
c_1	[MPa]	Material Parameter 1	0.55
c_2	[MPa]	Material Parameter 2	0.30

Then, the total Kirchhoff stress tensor $\boldsymbol{\tau}$ and the Eulerian moduli $\mathbb{c}$ can be determined as

$$\begin{aligned} \boldsymbol{\tau} &:= \big[\kappa\big(J^2 - J\big) - 2\,c_1\big]\,\boldsymbol{g}^{-1} + \big[2\,c_1 + 4\,c_2\big(\boldsymbol{b} : \boldsymbol{g} - 3\big)\big]\,\boldsymbol{b}\,, \\ \mathbb{c} &:= 8\,c_2\,\boldsymbol{b} \otimes \boldsymbol{b} + \kappa\big(2\,J^2 - J\big)\,\boldsymbol{g}^{-1} \otimes \boldsymbol{g}^{-1} + \big[4\,c_1 - 2\,\kappa\big(J^2 - J\big)\big]\mathbb{I}_{\boldsymbol{g}^{-1}}\,, \end{aligned} \tag{3.21}$$

where $\big(\mathbb{I}_{\boldsymbol{g}^{-1}}\big)^{abcd} := \frac{1}{2}\left[\big(g^{-1}\big)^{ac}\big(g^{-1}\big)^{bd} + \big(g^{-1}\big)^{ad}\big(g^{-1}\big)^{bc}\right]$ in indicial representation.

CHAPTER 4

DISCRETIZATION OF THE COUPLED EQUATIONS

This chapter is concerned with the numerical solution techniques for the coupled differential equations of electromechanics. Employing the constitutive equations for the selected models which are presented in Chapter 3, the Finite Element Method (FEM) is used to solve the coupled electro-mechanical differential equations. At the begining of this chapter, the preliminaries for the coupled electro-mechanical system of equations; that is, the governing differential equations in strong form, are recalled. Then, the standard FEM procedure is presented in Section 4.2. So as to solve the weak form of the electro-mechanical equations, linearization must be applied since they are still nonlinear. Consequently, Galerkin functionals for the mechanical and electrical parts of the coupled electro-mechanical equations, and their incremental form are desired in Section 4.3. In Section 4.4, employing the FE discretization in the Galerkin functionals and their incremental form, the residual vectors and the consistent tangent matrices are obtained. To find the solution vector of electro-mechanical system, the Newton scheme is used. In this chapter, only the formulation for the standard FEM is explained. The four-field mixed FEM has been used, but its formulation has not been shown for the sake of generality and brevity. Detailed information about the latter method is available in [9, 10, 27] and the ones cited therein.

4.1 Preliminaries

The detailed information for the preliminaries of coupled electromechanical system of equations are provided in Chapters 2 and 3. However, for the sake of completeness, these are briefly recalled in this section as well. To begin with, $\boldsymbol{X}$ and $\boldsymbol{x}$ are the

locations of a material point in the reference and spatial configurations, respectively. Moreover, the deformation gradient (2.8) is denoted as

$$\boldsymbol{F}\big(\boldsymbol{X}\big) = \nabla_{\boldsymbol{X}}\boldsymbol{\varphi}\big(\boldsymbol{X}, t\big)\,, \tag{4.1}$$

which maps a tangent vector in the Lagrangian configuration to that of the Eulerian configuration. Furthermore, $\boldsymbol{E}$ and $\boldsymbol{D}$ are the electric field vector and the electric displacement vector in reference configuration, respectively. The spatial counterparts can be determined by the *push-forward* operations (2.82) and (2.84) such that [9, 10]

$$\begin{aligned} \boldsymbol{e} &:= \boldsymbol{\varphi}_*\big(\boldsymbol{E}\big) = \boldsymbol{F}^{-T}\boldsymbol{E}\,, \\ \tilde{\boldsymbol{d}} &:= \boldsymbol{\varphi}_*\big(\boldsymbol{D}\big) = \boldsymbol{F}\boldsymbol{D}, \quad \text{and} \quad \tilde{\boldsymbol{d}} = J\boldsymbol{d}\,. \end{aligned} \tag{4.2}$$

In the current configuration, the Maxwell equations for electrostatics are written as

$$\text{div}\,\big(\boldsymbol{d}\big) = \rho_f \quad \text{and} \quad \text{curl}\,\big(\boldsymbol{e}\big) = \boldsymbol{0} \tag{4.3}$$

where $\boldsymbol{e} = -\nabla_{\boldsymbol{x}}\,\phi$. The latter can be written for the electric field vector and the electric displacement vector in the reference configuration as:

$$\text{Div}\,\big(\boldsymbol{D}\big) = \rho_f^0 \quad \text{and} \quad \text{Curl}\,\big(\boldsymbol{E}\big) = \boldsymbol{0} \tag{4.4}$$

where $\boldsymbol{E} = -\nabla_{\boldsymbol{X}}\,\phi$.

The governing constitutive relation for the electric field vector and the electric displacement vector for a dielectric material are defined as:

$$\begin{aligned} \boldsymbol{d} &:= \epsilon_0\,\boldsymbol{g}^{-1}\,\boldsymbol{e} + \boldsymbol{p}\,, \\ \boldsymbol{D} &:= J\epsilon_0\boldsymbol{C}^{-1}\boldsymbol{E} + \boldsymbol{P}\,, \end{aligned} \tag{4.5}$$

where $\boldsymbol{P}$ and $\boldsymbol{p}$ are the electric polarization vectors in the Lagrangian and Eulerian settings, respectively, and the relation between these two vectors can be expressed as $\boldsymbol{P} = J\boldsymbol{F}^{-1}\boldsymbol{p}$. For linear isotropic dielectric materials, the polarization induced by the medium is proportional to electric field itself [9, 15]. Hence, for these materials, the polarization term is dropped out and the expression (4.5) simplifies to

$$\begin{aligned} \tilde{\boldsymbol{d}} &:= \epsilon_0\,\epsilon_r\,\boldsymbol{g}^{-1}\,\boldsymbol{e}\,, \\ \boldsymbol{D} &:= J\epsilon_0\,\epsilon_r\,\boldsymbol{C}^{-1}\boldsymbol{E}\,. \end{aligned} \tag{4.6}$$

In order to solve the mechanical part of the coupled electromechanical equations, the conservation of linear momentum (2.102) and the Maxwell equation for electrostatics (2.77) are applied. To illustrate, in the Eulerian configuration, the conservation of linear momentum states that

$$\operatorname{div}\left(\boldsymbol{\sigma}\right) + \rho\boldsymbol{\gamma} = \rho\dot{\boldsymbol{v}} \quad \text{in} \quad \mathcal{S}\,. \tag{4.7}$$

Knowing that the total Cauchy stress can be written in terms of the total Kirchhoff stress using (2.36), (4.7) is modified as

$$\operatorname{div}\left(J^{-1}\boldsymbol{\tau}\right) + \rho\boldsymbol{\gamma} = \rho\dot{\boldsymbol{v}} \quad \text{in} \quad \mathcal{S}\,. \tag{4.8}$$

To finalize the description of the boundary value problem of the coupled electromechanics in the Eulerian configuration, the boundary conditions must be introduced. For that case, the surface of the body is divided into two such that mechanical and electrical essential (Dirichlet) and natural (Neumann) boundary conditions are prescribed; that is,

$$\begin{aligned} &\partial\mathcal{S} = \partial\mathcal{S}^{\boldsymbol{\varphi}} \cup \partial\mathcal{S}^{\boldsymbol{t}} \quad \text{and} \quad \partial\mathcal{S} = \partial\mathcal{S}^{\phi} \cup \partial\mathcal{S}^{\sigma}\,, \\ &\partial\mathcal{S}^{\boldsymbol{\varphi}} \cap \partial\mathcal{S}^{\boldsymbol{t}} = \varnothing \quad \text{and} \quad \partial\mathcal{S}^{\phi} \cap \partial\mathcal{S}^{\sigma} = \varnothing\,. \end{aligned} \tag{4.9}$$

Superscript $\boldsymbol{\varphi}$ and ϕ represent the mechanical and electrical Dirichler boundary conditions, respectively. Similarly, $\boldsymbol{t}$ and σ are written for the mechanical and electrical Neumann boundary conditions, respectively. Particularly, in the current configuration, the Dirichlet boundary conditions for the mechanical and the electrical equations are represented as follows

$$\boldsymbol{\varphi} = \overline{\boldsymbol{\varphi}} \quad \text{on} \quad \partial\mathcal{S}^{\boldsymbol{\varphi}} \quad \text{and} \quad \phi = \overline{\phi} \quad \text{on} \quad \partial\mathcal{S}^{\phi}\,. \tag{4.10}$$

Similarly, in the current configuration, the Neumann boundary conditions for the mechanical and electrical equations are represented as follows

$$\boldsymbol{\sigma}\,\boldsymbol{n} = \overline{\boldsymbol{t}} \quad \text{on} \quad \partial\mathcal{S}^{\boldsymbol{t}} \quad \text{and} \quad \boldsymbol{d}\cdot\boldsymbol{n} = \sigma_f \quad \text{on} \quad \partial\mathcal{S}^{\sigma}\,. \tag{4.11}$$

4.2 Discretization using Finite Element Method

In this section, the governing differential equations of the coupled electromechanics in strong form is transformed into the weak form for the prescribed boundary conditions given in (4.10) and (4.11). For this purpose, (4.6) and (4.8) are multiplied by the test functions $\{-\boldsymbol{g}\delta\boldsymbol{\varphi}, -\delta\phi\}$. $\delta\boldsymbol{\varphi}$ is the variational form of the non-linear deformation map while $\delta\phi$ is the variational form of the electric potential.

$$\begin{aligned}
&\int_{\mathcal{S}} \left\{ -\left(\boldsymbol{g}\delta\boldsymbol{\varphi}\right) \cdot \operatorname{div}\left(J^{-1}\boldsymbol{\tau}\right)\right\} dv - \int_{\mathcal{S}} \left\{\left(\boldsymbol{g}\delta\boldsymbol{\varphi}\right) \cdot \rho\boldsymbol{\gamma}\right\} dv + \int_{\mathcal{S}} \left\{\left(\boldsymbol{g}\delta\boldsymbol{\varphi}\right) \cdot \rho\dot{\boldsymbol{v}}\right\} \mathrm{d}v = 0 \\
&\int_{\mathcal{S}} \left\{ -\delta\phi \operatorname{div}\left(J^{-1}\tilde{\boldsymbol{d}}\right)\right\} dv + \int_{\mathcal{S}} \left\{\delta\phi\, \rho_f\right\} dv = 0
\end{aligned} \tag{4.12}$$

Integration-by-parts is applied to first terms on the left hand side of (4.12) to obtain

$$\begin{aligned}
\int_{\mathcal{S}} \left\{ -\left(\boldsymbol{g}\delta\boldsymbol{\varphi}\right) \cdot \operatorname{div}\left(J^{-1}\boldsymbol{\tau}\right)\right\} dv &= -\int_{\mathcal{S}} \left\{ \operatorname{div}\left[\left(\boldsymbol{g}\delta\boldsymbol{\varphi}\right) \cdot J^{-1}\boldsymbol{\tau}\right]\right\} dv \\
&\quad + \int_{\mathcal{S}} \left\{\left(\boldsymbol{g}\nabla_{\boldsymbol{x}}\delta\boldsymbol{\varphi}\right) : \left(J^{-1}\boldsymbol{\tau}\right)\right\} dv\,, \\
\int_{\mathcal{S}} \left\{ -\delta\phi \operatorname{div}\left(J^{-1}\tilde{\boldsymbol{d}}\right)\right\} dv &= -\int_{\mathcal{S}} \left\{ \operatorname{div}\left(\delta\phi\, J^{-1}\tilde{\boldsymbol{d}}\right)\right\} dv \\
&\quad + \int_{\mathcal{S}} \left\{\nabla_{\boldsymbol{x}}\delta\phi \cdot J^{-1}\tilde{\boldsymbol{d}}\right\} dv\,.
\end{aligned} \tag{4.13}$$

Inserting (4.13) into (4.12), the Galerkin functionals can be obtained as

$$\begin{aligned}
G^m\left(\delta\boldsymbol{\varphi}, \boldsymbol{\varphi}, \phi\right) &= \int_{\mathcal{S}} \left\{\left(\boldsymbol{g}\nabla_{\boldsymbol{x}}\delta\boldsymbol{\varphi}\right) : \left(J^{-1}\boldsymbol{\tau}\right)\right\} dv - \int_{\partial\mathcal{S}} \left\{\left(\boldsymbol{g}\delta\boldsymbol{\varphi}\right) \cdot \boldsymbol{t}\right\} da \\
&\quad - \int_{\mathcal{S}} \left\{\left(\boldsymbol{g}\delta\boldsymbol{\varphi}\right) \cdot \rho\boldsymbol{\gamma}\right\} dv + \int_{\mathcal{S}} \left\{\left(\boldsymbol{g}\delta\boldsymbol{\varphi}\right) \cdot \rho\dot{\boldsymbol{v}}\right\} \mathrm{d}v\,, \\
G^e\left(\delta\phi, \phi, \boldsymbol{\varphi}\right) &= \int_{\mathcal{S}} \left\{\nabla_{\boldsymbol{x}}\delta\phi \cdot J^{-1}\tilde{\boldsymbol{d}}\right\} dv - \int_{\partial\mathcal{S}} \left\{\delta\phi\, \sigma_f\right\} da \\
&\quad + \int_{\mathcal{S}} \left\{\delta\phi\, \rho_f\right\} dv\,,
\end{aligned} \tag{4.14}$$

where (4.14) can be decomposed as:

$$\begin{aligned}
G^m\left(\delta\boldsymbol{\varphi}, \boldsymbol{\varphi}, \phi\right) &:= G^m_{int}\left(\delta\boldsymbol{\varphi}, \boldsymbol{\varphi}, \phi\right) - G^m_{ext}\left(\delta\boldsymbol{\varphi}, \boldsymbol{\varphi}, \phi\right)\,, \\
G^e\left(\delta\phi, \phi, \boldsymbol{\varphi}\right) &:= G^e_{int}\left(\delta\phi, \phi, \boldsymbol{\varphi}\right) - G^e_{ext}\left(\delta\phi, \phi, \boldsymbol{\varphi}\right)\,.
\end{aligned} \tag{4.15}$$

In the absence of mechanical traction vector on the surface $\partial\mathcal{S}^{\boldsymbol{t}}$ and body force for the quasi-static loading, external mechanical part of the Galerkin functional become

zero such that

$$
\begin{aligned}
G^m_{ext}\big(\delta\boldsymbol{\varphi},\boldsymbol{\varphi},\phi\big) = &\int_{\partial\mathcal{S}} \big\{\big(\boldsymbol{g}\delta\boldsymbol{\varphi}\big)\cdot\boldsymbol{t}\big\}\,da + \int_{\mathcal{S}} \big\{\big(\boldsymbol{g}\delta\boldsymbol{\varphi}\big)\cdot\rho\boldsymbol{\gamma}\big\}\,dv \\
&- \int_{\mathcal{S}} \big\{\big(\boldsymbol{g}\delta\boldsymbol{\varphi}\big)\cdot\rho\dot{\boldsymbol{v}}\big\}\mathrm{d}v = 0
\end{aligned}
\tag{4.16}
$$

Likewise, in the case that there is no free electric charges on the surface of the body $\partial\mathcal{S}^\sigma$ and in the body, external electrical part of the Galerkin functional boils down to

$$
G^e_{ext}\big(\delta\phi,\phi,\boldsymbol{\varphi}\big) = \int_{\partial\mathcal{S}} \big\{\delta\phi\,\sigma_f\big\}\,da - \int_{\mathcal{S}} \big\{\delta\phi\,\rho_f\big\}\,dv = 0 \tag{4.17}
$$

As a result, the internal part of the mechanical and electrical Galerkin functionals are used for the calculation of the residual vector and the consistent tangent matrice.

$$
\begin{aligned}
G^m\big(\delta\boldsymbol{\varphi},\boldsymbol{\varphi},\phi\big) &= \int_{\mathcal{B}} \big\{\big(\boldsymbol{g}\nabla_{\boldsymbol{x}}\delta\boldsymbol{\varphi}\big):\boldsymbol{\tau}\big\}\,dV\,, \\
G^e\big(\delta\phi,\phi,\boldsymbol{\varphi}\big) &= \int_{\mathcal{B}} \big\{\nabla_{\boldsymbol{x}}\delta\phi\cdot\tilde{\boldsymbol{d}}\big\}\,dV\,,
\end{aligned}
\tag{4.18}
$$

where $\boldsymbol{\tau}$ is the total Kirchhoff stress, which is defined as $\boldsymbol{\tau} := \boldsymbol{\tau}_{vol} + \boldsymbol{\tau}_{iso} + \boldsymbol{\tau}^{em}$ in (3.13) or $\boldsymbol{\tau} := \boldsymbol{\tau}^m + \boldsymbol{\tau}^{em}$ in (3.17).

4.3 Linearization of Galerkin Functional

In order to solve (4.18) combined with the prescribed boundary conditions presented in (4.10) and (4.11), linearization must be conducted within the iterativeframework of the Newton method. The linearization of the Galerkin functionals yields

$$
\begin{aligned}
\mathrm{Lin}\Big[G^m\big(\delta\boldsymbol{\varphi},\boldsymbol{\varphi},\phi\big)\Big]_{\tilde{\boldsymbol{\varphi}},\tilde{\phi}} &= G^m\big(\delta\tilde{\boldsymbol{\varphi}},\tilde{\boldsymbol{\varphi}},\tilde{\phi}\big) + \Delta G^m\big(\delta\boldsymbol{\varphi},\tilde{\boldsymbol{\varphi}},\tilde{\phi};\Delta\boldsymbol{\varphi},\Delta\phi\big)\,, \\
\mathrm{Lin}\Big[G^e\big(\delta\phi,\phi,\boldsymbol{\varphi}\big)\Big]_{\tilde{\phi},\tilde{\boldsymbol{\varphi}}} &= G^e\big(\delta\tilde{\phi},\tilde{\phi},\tilde{\boldsymbol{\varphi}}\big) + \Delta G^e\big(\delta\phi,\tilde{\phi},\tilde{\boldsymbol{\varphi}};\Delta\phi,\Delta\boldsymbol{\varphi}\big)\,,
\end{aligned}
\tag{4.19}
$$

where ΔG^m and ΔG^e are the incremental forms of Galerkin functionals for the mechanical part and the electrical part, respectively. These two incremental functionals can be determined as

$$
\begin{aligned}
\Delta G^m\big(\delta\boldsymbol{\varphi},\boldsymbol{\varphi},\phi;\Delta\boldsymbol{\varphi},\Delta\phi\big) &= \Delta\Big[\int_{\mathcal{B}} \big\{\big(\boldsymbol{g}\nabla_{\boldsymbol{x}}\delta\boldsymbol{\varphi}\big):\boldsymbol{\tau}\big\}\,dV\Big]\,, \\
\Delta G^e\big(\delta\phi,\phi,\boldsymbol{\varphi};\Delta\phi,\Delta\boldsymbol{\varphi}\big) &= \Delta\Big[\int_{\mathcal{B}} \big\{\nabla_{\boldsymbol{x}}\delta\phi\cdot\tilde{\boldsymbol{d}}\big\}\,dV\Big]\,.
\end{aligned}
\tag{4.20}
$$

The linearized weak form of (4.20) can be rewritten using the chain rule operation. The incremental mechanical part $(4.20)_1$ of the Galerkin functional can be written as

$$\begin{aligned}\Delta G^m\big(\delta\boldsymbol{\varphi},\boldsymbol{\varphi},\phi;\Delta\boldsymbol{\varphi},\Delta\phi\big) =& \Delta\Big[\int_{\mathcal{B}}\big\{\big(\boldsymbol{g}\nabla_{\boldsymbol{x}}\delta\boldsymbol{\varphi}\big):\boldsymbol{\tau}\big\}\,dV\Big]\,,\\ &= \int_{\mathcal{B}}\big\{\Delta\big(\boldsymbol{g}\nabla_{\boldsymbol{x}}\delta\boldsymbol{\varphi}\big):\boldsymbol{\tau}\big\}\,dV\\ &+\int_{\mathcal{B}}\big\{\big(\boldsymbol{g}\nabla_{\boldsymbol{x}}\delta\boldsymbol{\varphi}\big):\Delta\boldsymbol{\tau}\big\}\,dV\,,\end{aligned} \tag{4.21}$$

where $\Delta\big(\boldsymbol{g}\nabla_{\boldsymbol{x}}\delta\boldsymbol{\varphi}\big)$ in (4.21) can be found by:

$$\Delta\big(\boldsymbol{g}\nabla_{\boldsymbol{x}}\delta\boldsymbol{\varphi}\big) := \boldsymbol{g}\Delta\big(\nabla_{\boldsymbol{x}}\delta\boldsymbol{\varphi}\big) = \boldsymbol{g}\Delta\big(\nabla_{\boldsymbol{X}}\delta\boldsymbol{\varphi}\boldsymbol{F}^{-1}\big) = -\boldsymbol{g}\big(\nabla_{\boldsymbol{x}}\delta\boldsymbol{\varphi}\big)\big(\nabla_{\boldsymbol{x}}\Delta\boldsymbol{\varphi}\big)\,. \tag{4.22}$$

The incremental form of the total Kirchhoff stress tensor $\Delta\boldsymbol{\tau}$ can be found by employing the Lie derivative of the total Kirchhoff stress tensor. The way how to obtain the Lie derivative is determined by (2.33)

$$\begin{aligned}\mathcal{L}_{\Delta}\boldsymbol{\tau} &= \boldsymbol{F}\Big\{\Delta\big(\boldsymbol{F}^{-1}\boldsymbol{\tau}\boldsymbol{F}^{-T}\big)\Big\}\boldsymbol{F}^{T}\,,\\ &= \boldsymbol{F}\Big\{\Delta\boldsymbol{F}^{-1}\boldsymbol{\tau}\boldsymbol{F}^{-T}+\boldsymbol{F}^{-1}\Delta\boldsymbol{\tau}\boldsymbol{F}^{-T}\\ &+\boldsymbol{F}^{-1}\boldsymbol{\tau}\Delta\boldsymbol{F}^{-T}\Big\}\boldsymbol{F}^{T}\,,\\ &= \big(\boldsymbol{F}\,\Delta\boldsymbol{F}^{-1}\big)\boldsymbol{\tau}+\Delta\boldsymbol{\tau}+\boldsymbol{\tau}\big(\boldsymbol{F}\,\Delta\boldsymbol{F}^{-1}\big)^{T}\,,\end{aligned} \tag{4.23}$$

where

$$\Delta\boldsymbol{F}^{-1} := -\boldsymbol{F}^{-1}\Delta\boldsymbol{F}\boldsymbol{F}^{-1} = -\boldsymbol{F}^{-1}\big(\nabla_{\boldsymbol{X}}\Delta\boldsymbol{\varphi}\big)\boldsymbol{F}^{-1} = -\boldsymbol{F}^{-1}\nabla_{\boldsymbol{x}}\Delta\boldsymbol{\varphi}\,, \tag{4.24}$$

Inserting (4.24) into (4.23), more pronounced results can be obtained. Hence, the incremental Kirchhoff stress tensor is

$$\Delta\boldsymbol{\tau} = \mathcal{L}_{\Delta}\boldsymbol{\tau}+\big(\nabla_{\boldsymbol{x}}\Delta\boldsymbol{\varphi}\big)\boldsymbol{\tau}+\boldsymbol{\tau}\big(\nabla_{\boldsymbol{x}}\Delta\boldsymbol{\varphi}\big)^{T}\,, \tag{4.25}$$

where

$$\begin{aligned}\mathcal{L}_{\Delta}\boldsymbol{\tau} :&= \big(\mathbb{c}_{vol}+\mathbb{c}_{iso}+\mathbb{c}^{em}\big):\big(\boldsymbol{g}\nabla_{\boldsymbol{x}}\Delta\boldsymbol{\varphi}\big)-\mathbb{b}\cdot\mathcal{L}_{\Delta}\boldsymbol{e}\\ &= \mathbb{c}:\big(\boldsymbol{g}\nabla_{\boldsymbol{x}}\Delta\boldsymbol{\varphi}\big)+\mathbb{b}\cdot\nabla_{\boldsymbol{x}}\Delta\phi\end{aligned} \tag{4.26}$$

Using (4.22),(4.25), and (4.26) in (4.21), the linearized form of Galerkin functional for mechanical equation, (4.21), can be obtained

$$\begin{aligned}\Delta G^m\big(\delta\boldsymbol{\varphi},\boldsymbol{\varphi},\phi;\Delta\boldsymbol{\varphi},\Delta\phi\big) &= \int_{\mathcal{B}}\big\{\big(\boldsymbol{g}\,\nabla_{\boldsymbol{x}}\delta\boldsymbol{\varphi}\big):\mathbb{c}:\big(\boldsymbol{g}\,\nabla_{\boldsymbol{x}}\Delta\boldsymbol{\varphi}\big)\big\}\,dV\\ &+\int_{\mathcal{B}}\big\{\big(\boldsymbol{g}\,\nabla_{\boldsymbol{x}}\delta\boldsymbol{\varphi}\big):\mathbb{b}\cdot\nabla_{\boldsymbol{x}}\Delta\phi\big\}\,dV\\ &+\int_{\mathcal{B}}\big\{\big(\boldsymbol{g}\,\nabla_{\boldsymbol{x}}\delta\boldsymbol{\varphi}\big):\big(\nabla_{\boldsymbol{x}}\Delta\boldsymbol{\varphi}\,\boldsymbol{\tau}\big)\big\}\,dV\,,\end{aligned} \tag{4.27}$$

where $\mathbb{b} := -\partial_{\boldsymbol{e}}\boldsymbol{\tau}^{em}$ from $(3.14)_5$. Consequently, the linearized Galerkin functional is acquired. Furthermore, the linearization of electrical part $(4.20)_2$ can be derived as

$$\begin{aligned}\Delta G^e\big(\delta\phi,\phi,\boldsymbol{\varphi};\Delta\phi,\Delta\boldsymbol{\varphi}\big) &= \Delta\Big[\int_{\mathcal{B}}\big\{\nabla_{\boldsymbol{x}}\delta\phi\cdot\tilde{\boldsymbol{d}}\big\}\,dV\Big]\,,\\ &= \int_{\mathcal{B}}\big\{\Delta\big(\nabla_{\boldsymbol{x}}\delta\phi\big)\cdot\tilde{\boldsymbol{d}}\big\}\,dV\\ &+\int_{\mathcal{B}}\big\{\nabla_{\boldsymbol{x}}\delta\phi\cdot\Delta\big(\tilde{\boldsymbol{d}}\big)\big\}\,dV\,,\end{aligned} \tag{4.28}$$

where $\Delta\big(\nabla_{\boldsymbol{x}}\delta\phi\big) := \Delta\big(\nabla_{\boldsymbol{X}}\delta\phi\boldsymbol{F}^{-1}\big)$ and using the chain rule as in the case of (4.22), the first term in the right hand side of (4.28) can be redefined as

$$\begin{aligned}\Delta\big(\nabla_{\boldsymbol{x}}\delta\phi\big) :&= \Delta\big(\nabla_{\boldsymbol{X}}\delta\phi\boldsymbol{F}^{-1}\big)\,,\\ &= \Delta\big(\nabla_{\boldsymbol{X}}\delta\phi\big)\boldsymbol{F}^{-1}+\nabla_{\boldsymbol{X}}\delta\phi\Delta\big(\boldsymbol{F}^{-1}\big)\,,\\ &= -\big(\nabla_{\boldsymbol{x}}\delta\phi\big)\big(\nabla_{\boldsymbol{x}}\Delta\boldsymbol{\varphi}\big)\,.\end{aligned} \tag{4.29}$$

In addition, the second term of (4.28) can be determined by employing the Lie derivative of the electric displacement vector, which is an Eulerian vector. It can be interpreted considering the Lie derivative in (2.33):

$$\begin{aligned}\mathcal{L}_{\Delta}\tilde{\boldsymbol{d}} :&= \boldsymbol{F}\big[\Delta\big(\boldsymbol{F}^{-1}\tilde{\boldsymbol{d}}\big)\big]\,,\\ &= \boldsymbol{F}\big[\Delta\big(\boldsymbol{F}^{-1}\big)\tilde{\boldsymbol{d}}+\boldsymbol{F}^{-1}\Delta\big(\tilde{\boldsymbol{d}}\big)\big]\,,\\ &= -\big(\nabla_{\boldsymbol{x}}\Delta\boldsymbol{\varphi}\big)\tilde{\boldsymbol{d}}+\Delta\tilde{\boldsymbol{d}}\,.\end{aligned} \tag{4.30}$$

The incremental electric displacement vector is then found as

$$\Delta\tilde{\boldsymbol{d}} := \mathcal{L}_{\Delta}\tilde{\boldsymbol{d}}+\big(\nabla_{\boldsymbol{x}}\Delta\boldsymbol{\varphi}\big)\tilde{\boldsymbol{d}}\,, \tag{4.31}$$

where the Lie derivative of the electric displacement vector can also be defined as

$$\begin{aligned}\mathcal{L}_{\Delta}\tilde{\boldsymbol{d}} &:= \mathbb{a} : \frac{1}{2}\mathcal{L}_{\Delta}\boldsymbol{g} - \mathbb{d}\cdot\mathcal{L}_{\Delta}\boldsymbol{e}\,,\\ &= \mathbb{a} : \big(\boldsymbol{g}\,\nabla_{\boldsymbol{x}}\Delta\boldsymbol{\varphi}\big) + \mathbb{d}\cdot\nabla_{\boldsymbol{x}}\Delta\phi\end{aligned} \tag{4.32}$$

In (4.32), $\mathbb{a} := 2\partial_{\boldsymbol{g}}\tilde{\boldsymbol{d}}$ and $\mathbb{d} := -\partial_{\boldsymbol{e}}\tilde{\boldsymbol{d}}$ from $(3.14)_4$ and$(3.14)_6$, respectively. Finally, electric part of the incremental Galerkin functional becomes

$$\begin{aligned}\Delta G^{e}\big(\delta\phi,\phi,\boldsymbol{\varphi};\Delta\phi,\Delta\boldsymbol{\varphi}\big) &= \int_{\mathcal{B}}\big(\nabla_{\boldsymbol{x}}\delta\phi\big)\cdot\mathbb{a} : \big(\boldsymbol{g}\,\nabla_{\boldsymbol{x}}\Delta\boldsymbol{\varphi}\big)\,dV\\ &\quad+\int_{\mathcal{B}}\big(\nabla_{\boldsymbol{x}}\delta\phi\big)\cdot\mathbb{d}\cdot\nabla_{\boldsymbol{x}}\Delta\phi\,dV\,.\end{aligned} \tag{4.33}$$

To sum up, all the Galerkin functionals and their incremental forms can be summarized as follows

$$\begin{aligned}G^{m}\big(\delta\boldsymbol{\varphi},\boldsymbol{\varphi},\phi\big) &= \int_{\mathcal{B}}\big\{\big(\boldsymbol{g}\,\nabla_{\boldsymbol{x}}\delta\boldsymbol{\varphi}\big) : \boldsymbol{\tau}\big\}\,dV\,,\\ G^{e}\big(\delta\phi,\phi,\boldsymbol{\varphi}\big) &= \int_{\mathcal{B}}\big\{\nabla_{\boldsymbol{x}}\delta\phi\cdot\tilde{\boldsymbol{d}}\big\}\,dV\,,\\ \Delta G^{mm}_{mat}\big(\delta\boldsymbol{\varphi},\boldsymbol{\varphi},\phi;\Delta\boldsymbol{\varphi},\Delta\phi\big) &= \int_{\mathcal{B}}\big\{\big(\boldsymbol{g}\,\nabla_{\boldsymbol{x}}\delta\boldsymbol{\varphi}\big) : \mathbb{c} : \big(\boldsymbol{g}\,\nabla_{\boldsymbol{x}}\Delta\boldsymbol{\varphi}\big)\big\}\,dV\,,\\ \Delta G^{mm}_{geo}\big(\delta\boldsymbol{\varphi},\boldsymbol{\varphi},\phi;\Delta\boldsymbol{\varphi},\Delta\phi\big) &= \int_{\mathcal{B}}\big\{\big(\boldsymbol{g}\,\nabla_{\boldsymbol{x}}\delta\boldsymbol{\varphi}\big) : \big(\nabla_{\boldsymbol{x}}\Delta\boldsymbol{\varphi}\,\boldsymbol{\tau}\big)\big\}\,dV\,,\\ \Delta G^{me}\big(\delta\boldsymbol{\varphi},\phi,\boldsymbol{\varphi};\Delta\phi,\Delta\boldsymbol{\varphi}\big) &= \int_{\mathcal{B}}\big\{\big(\boldsymbol{g}\,\nabla_{\boldsymbol{x}}\delta\boldsymbol{\varphi}\big) : \mathbb{b}\cdot\nabla_{\boldsymbol{x}}\Delta\phi\big\}\,dV\,,\\ \Delta G^{em}\big(\delta\phi,\boldsymbol{\varphi},\phi;\Delta\boldsymbol{\varphi},\Delta\phi\big) &= \int_{\mathcal{B}}\big\{\big(\nabla_{\boldsymbol{x}}\delta\phi\big)\cdot\mathbb{a} : \big(\boldsymbol{g}\,\nabla_{\boldsymbol{x}}\Delta\boldsymbol{\varphi}\big)\big\}\,dV\\ \Delta G^{ee}\big(\delta\phi,\phi,\boldsymbol{\varphi};\Delta\phi,\Delta\boldsymbol{\varphi}\big) &= \int_{\mathcal{B}}\big\{\big(\nabla_{\boldsymbol{x}}\delta\phi\big)\cdot\mathbb{d}\cdot\nabla_{\boldsymbol{x}}\Delta\phi\big\}\,dV\,.\end{aligned} \tag{4.34}$$

where ΔG^{mm}_{mat} denotes the material part of the incremental Galerkin functional of the mechanical contribution whereas ΔG^{mm}_{geo} stands for the geometric counterpart of the mechanical contribution.

4.4 Discretization of Galerkin Functionals

So as to numerically analyze a coupled boundary-value problem, the body of interest $\mathcal{B}$ is divided into finite elements $\mathcal{B}^{e}$. Then, the Galerkin functionals and their increments for the prescribed boundary conditions are discretized to obtain the associated

residual vectors and the consistent tangent matrix terms. For this purpose, the test functions and the gradient terms in (4.34) are approximated as

$$
\begin{aligned}
\delta\boldsymbol{\varphi} &\cong \sum_{A=1}^{n} N^A\, \delta\boldsymbol{d}_A, \quad \text{in } \mathcal{B}^e \\
\nabla_{\boldsymbol{x}}\delta\boldsymbol{\varphi} &\cong \sum_{A=1}^{n} \delta\boldsymbol{d}_A \otimes \partial_{\boldsymbol{x}} N^A, \quad \text{in } \mathcal{B}^e \\
\Delta\boldsymbol{\varphi} &\cong \sum_{A=1}^{n} N^A\, \Delta\boldsymbol{d}_A, \quad \text{in } \mathcal{B}^e \\
\nabla_{\boldsymbol{x}}\Delta\boldsymbol{\varphi} &\cong \sum_{A=1}^{n} \Delta\boldsymbol{d}_A \otimes \partial_{\boldsymbol{x}} N^A, \quad \text{in } \mathcal{B}^e \\
\delta\phi &\cong \sum_{A=1}^{n} N^A\, \delta\phi_A, \quad \text{in } \mathcal{B}^e \\
\nabla_{\boldsymbol{x}}\delta\phi &= \sum_{A=1}^{n} \delta\phi_A\, \partial_{\boldsymbol{x}} N^A, \quad \text{in } \mathcal{B}^e \\
\Delta\phi &= \sum_{A=1}^{n} N^A\, \Delta\phi_A, \quad \text{in } \mathcal{B}^e \\
\nabla_{\boldsymbol{x}}\Delta\phi &= \sum_{A=1}^{n} \Delta\phi_A\, \partial_{\boldsymbol{x}} N^A, \quad \text{in } \mathcal{B}^e
\end{aligned}
\tag{4.35}
$$

where N^A is the shape function belonging to Node A where $\forall A = 1, 2, \ldots, n$. Moreover, *n* is the total number of nodes in each finite element. Inserting (4.35) into (4.34), the residual vectors and the tangent matrix terms are obtained as

$$
\begin{aligned}
\boldsymbol{R}^m &:= \mathop{\mathsf{A}}_{i=1}^{n_{el}} \left\{ \int_{\mathcal{B}} \partial_{\boldsymbol{x}} N^A \cdot \boldsymbol{\tau}\, dV \right\}, \\
\boldsymbol{R}^e &:= \mathop{\mathsf{A}}_{i=1}^{n_{el}} \left\{ \int_{\mathcal{B}} \partial_{\boldsymbol{x}} N^A \cdot \tilde{\boldsymbol{d}}\, dV \right\}, \\
\boldsymbol{K}^{mm}_{mat} &:= \mathop{\mathsf{A}}_{i=1}^{n_{el}} \left\{ \int_{\mathcal{B}} \partial_{\boldsymbol{x}} N^A \cdot \mathbb{c} \cdot \partial_{\boldsymbol{x}} N^B\, dV \right\}, \\
\boldsymbol{K}^{mm}_{geo} &:= \mathop{\mathsf{A}}_{i=1}^{n_{el}} \left\{ \int_{\mathcal{B}} \partial_{\boldsymbol{x}} N^A \cdot \left(\partial_{\boldsymbol{x}} N^B \boldsymbol{\tau}\right) dV \right\}, \\
\boldsymbol{K}^{me} &:= \mathop{\mathsf{A}}_{i=1}^{n_{el}} \left\{ \int_{\mathcal{B}} \partial_{\boldsymbol{x}} N^A \cdot \mathbb{b} \cdot \partial_{\boldsymbol{x}} N^B\, dV \right\}, \\
\boldsymbol{K}^{em} &:= \mathop{\mathsf{A}}_{i=1}^{n_{el}} \left\{ \int_{\mathcal{B}} \partial_{\boldsymbol{x}} N^A \cdot \mathbb{a} \cdot \partial_{\boldsymbol{x}} N^B\, dV \right\}, \\
\boldsymbol{K}^{ee} &:= \mathop{\mathsf{A}}_{i=1}^{n_{el}} \left\{ \int_{\mathcal{B}} \partial_{\boldsymbol{x}} N^A \cdot \mathbb{d} \cdot \partial_{\boldsymbol{x}} N^B\, dV \right\},
\end{aligned}
\tag{4.36}
$$

where A designates the assembly operator that gather the residual vector and tangent stiffness matrix of each local element into the global counterparts. Moreover, n_{el} is the total number of element. The assembly operation is carried out over the connectivity information of the elements. Hence, the Newton solution algorithm can be demonstrated as

$$\begin{bmatrix} \boldsymbol{d}^m \\ \boldsymbol{d}^e \end{bmatrix} \Longleftarrow \begin{bmatrix} \boldsymbol{d}^m \\ \boldsymbol{d}^e \end{bmatrix} - \begin{bmatrix} \boldsymbol{K}^{mm} & \boldsymbol{K}^{me} \\ \boldsymbol{K}^{em} & \boldsymbol{K}^{ee} \end{bmatrix}^{-1} \cdot \begin{bmatrix} \boldsymbol{R}^m \\ \boldsymbol{R}^e \end{bmatrix} \tag{4.37}$$

where $\boldsymbol{d}^m$ and $\boldsymbol{d}^e$ are the solution vectors for the mechanical and electrical parts of the coupled electro-mechanical equation system.

CHAPTER 5

NUMERICAL EXAMPLES

This chapter is devoted to representative numerical examples on the coupled electro-mechanics of EAPs, outlined in Chapters 2-4. Hence, in Section 5.1, the constitutive models presented in Chapter 3 are verfied with the associated articles. In addition, the mechanical behavior of elastomers with periodic microstructures under compression is considered. The smallest element that repeats itself before the deformation is called a unit cell. In the presence of inclusions or voids in unit cells, they can be symmetric or unsymmetric. In this study, only the symmetric unit cells with voids are employed. It is realized that under compressive loads with certain periodic boundary conditions, the microstructures with voids exhibit different mechanical instability phenomena than expected. Such materials show local buckling rather than global buckling which is demonstrated in the articles [4, 5, 6, 7] and many others. Moreover, the local buckling causes pattern transformations in the microstructure. Therefore, in Section 5.2, pattern transformation properties of periodic microstructures is investigated. In the final part of this chapter, combined effects; that is, pattern transformations of EAPs in the presence of both compressive loading and electric potential as boundary conditions are examined. The combined effect on the periodic microstructures is analyzed and the results are illustrated through computational examples. All these analyses are conducted using the Finite Element Analysis Program (FEAP) [51] and some of the meshes are created using ABAQUS/CAE [52].

5.1 Coupled Electromechanics

In this section, the electro-mechanical coupling is investigated for different free energy functions provided in Chapter 3. At first, the work carried out by [10] is examined. According to [10, 27], EAPs are quasi-incompressible materials where standard entirely displacement-based FEM may show a locking phenomenon. Hence, four-field FEM should be applied to overcome the volumetric locking. Hence, in Model I, four-field FEM formulated in the Eulerian configuration is applied along with the free energy functions which are different from the study provided in [10]. Accordingly, in Model I (3.9 or 3.11), the relative electric permittivity term is expressed as deformation dependent in [10]. The deformation dependence of the relative permittivity is obtained from the experimental results conducted by [50]. Secondly, [32] compares the effects of the coupled Boundary Element Method (BEM) and FEM, that is, the coupled BEM-FEM is compared with only standard FEM method. Moreover, for Model II in Table 3.2, the relative permittivity is simplified as being independent of deformation. Hence, the results obtained from the coupled electro-mechanical models are provided in the following subsections.

5.1.1 Example I: Bending Beam Actuator

In this model problem, a cantilever beam is exposed to the electric field through a voltage difference applied between two electrodes. One of the electrodes is placed at the bottom surface whereas the other is located in the middle of the beam, see Figure 5.2. It can be produced such that this electrode is sandwiched by two dielectric elastomers (EAPs). Besides, these electrodes are compliant meaning that they do not contribute to the stiffness of the beam. That is, they may deform along with the EAPs. The representation of the bending actuator which is employed throughout the analysis is shown in Figure 5.1 and 5.2. In addition, $\boldsymbol{e}_2 - \boldsymbol{e}_3$ plane in Figure 5.1 is fixed and the rest is free to move.

Hence, when the electric voltage difference is applied as depicted in Figure 5.2, there will be a contraction in the direction of the applied electric field whereas elongation occurs perpendicular to the electric field vector which causes the actuator bend. For

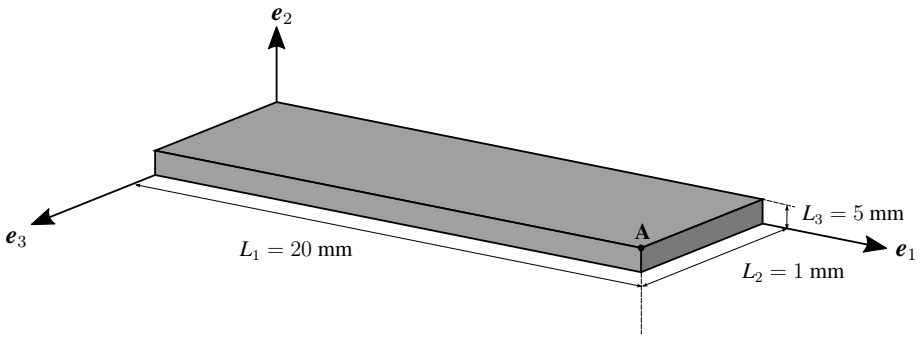

Figure 5.1: Representation of the bending actuator and its dimensions.

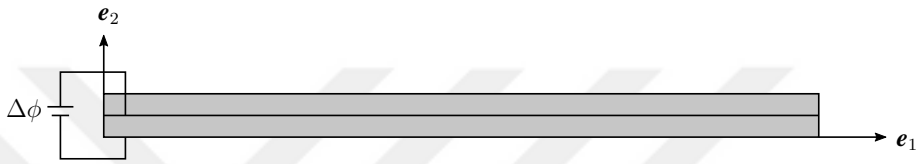

Figure 5.2: 2D representation of the bending actuator with an applied electric voltage difference.

the given electric voltage difference, different bending phases can be observed. To be more specific, the higher the electric voltage difference, the more the actuator bends under certain limits. To clearly understand the effect of the electrical stimulation on the beam actuator, the deformed shapes corresponding to different levels of voltage difference are presented in Figure 5.3. Moreover, in [10], the normalized displacement values of Point A shown in Figure 5.1 in $x-$ and $y-$ directions are provided for comparison. Point A is located at (20,1,5) as shown in Figure 5.1. The normalized values of the displacements in $x-$ and $y-$directions are plotted against the applied potential difference in Figure 5.5 and Figure 5.6, respectively.

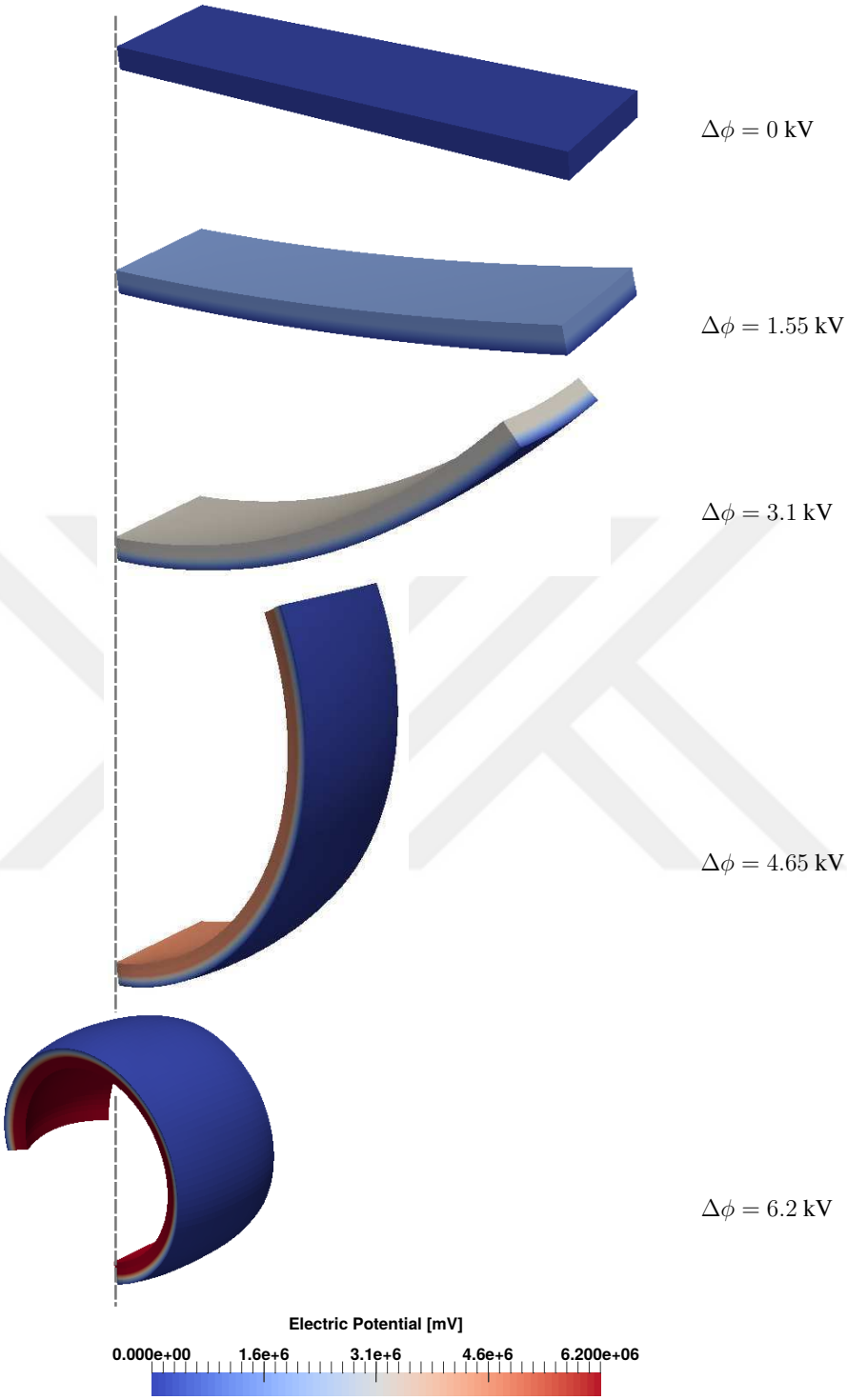

Figure 5.3: Deformed shapes of bending actuator.

Moreover, the distribution of the total stretch values of each element on the undeformed form of the bending beam actuator is depicted in Figure 5.4

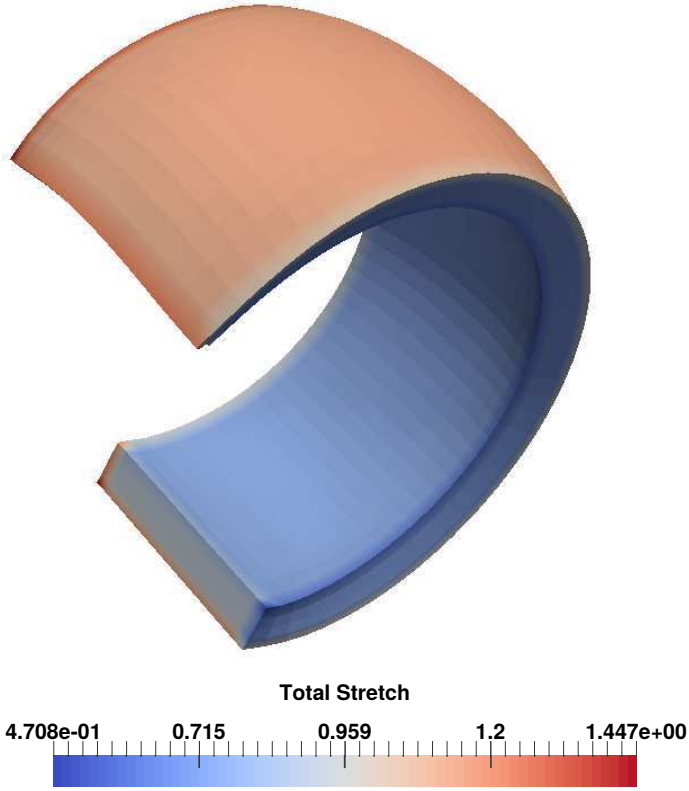

Figure 5.4: The stretch distribution on the undeformed form of the bending beam actuator.

Through this example our implementation of Model I is verified with the article results proposed by [10]. In this model, the relative permittivity is considered as deformation-dependent. Moreover, four-field FEM for finite deformations is achieved for the formulation considered in the Eulerian configuration. Furthermore, it can be seen from Figures 5.5 and 5.6 that employing about 2000 brick elements, similar results are obtained when it is compared with the results in the article proposed by [10]. However, when the number of elements is increased to about 5000 brick elements, the $x-$ and $y-$components of the displacement of Point A alters little from the results in the article and it reaches to its ultimate values when the number of elements is further increased to 8000 elements. Hence, for this problem 5000 element are accurate to achieve convergent and accurate results.

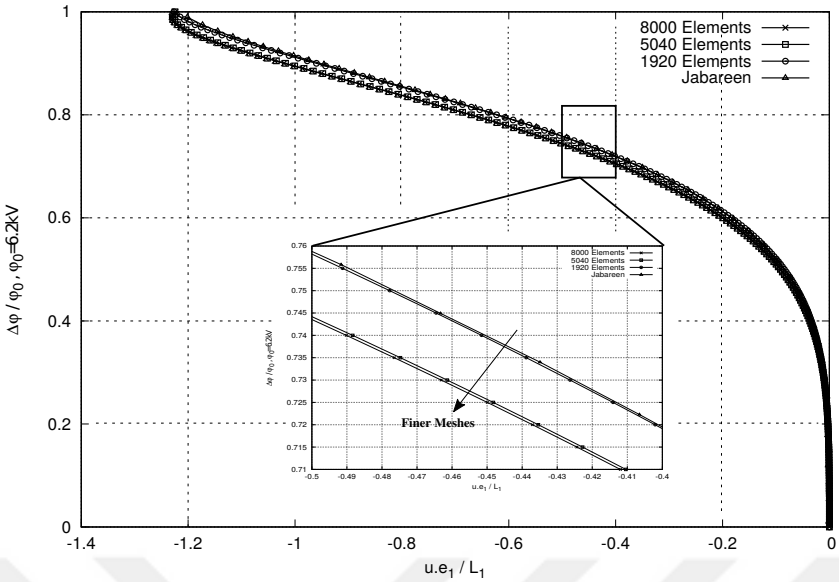

Figure 5.5: Potential difference vs. normalized displacement of Point A in $x-$direction.

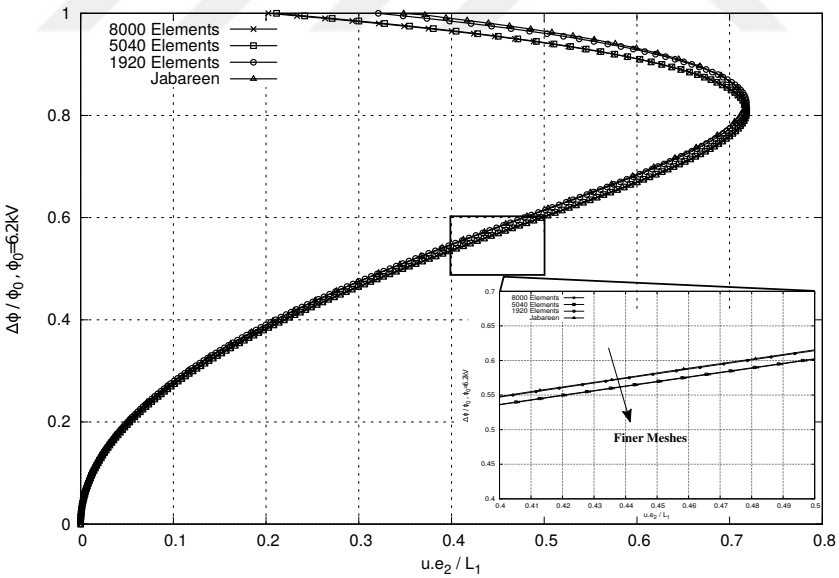

Figure 5.6: Potential difference vs. normalized displacement of Point A in $y-$direction.

5.1.2 Example II: C-Shaped Plate

In this part, Model II (3.16) mentioned in Chapter 3 is utilized for an electromechanical analysis of C-shaped plate body. For this model problem, the relative permittivity expression is independent of deformation. Accordingly, [32] compares the result of the coupled BEM-FEM and the standard FEM. It is emphasized that when the relative electric permittivity decreases, the effect of the free space increases. Hence, in order to eliminate such an effect, a coupled BEM-FEM approach is investigated. However, in this study only standard FEM is used for verification. In order to do so, the C-shaped plate is discretized by quadrilateral elements. The geometric dimesions and the FE mesh of the C-shaped plate is shown in Figure 5.7.

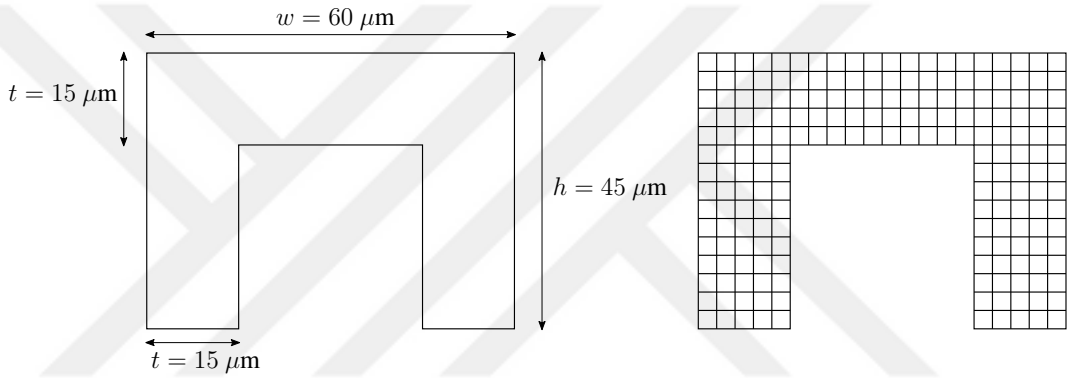

Figure 5.7: Dimensions of the C-shaped plate and quadrilateral mesh for standard FEM.

The electric potentials are applied to the plate as a boundary conditions as indicated in Figure 5.8. The lower and upper bounds are applied to electric voltages which have same magnitude but opposite signs. Also, the lower edges of the plate is not allowed to move in $y-$direction and bottom left corner point is fixed in $x-$ and $y-$direction to eliminate the rigid body motion. Employing different electric voltage differences and changing the relative permittivity constant defined in Table 3.2, the electric voltage gradients can be obtained and they are presented from Figure 5.9 to Figure 5.11.

In Figure 5.9, the relative permittivity is provided as 5 times greater than the electric permittivity of vacuum. For $\Delta\phi = \phi_{up} - \phi_{low} = 100 - (-100) = 200$ V, there appears a little deformation, whereas increasing the electric potential difference from

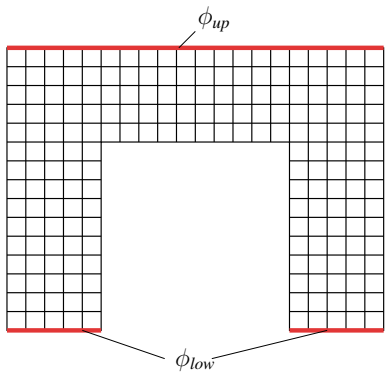

Figure 5.8: Applied electrical boundary conditions on the C-shaped plate.

200 V to 1 kV, there exists a considerable amount of deformation.

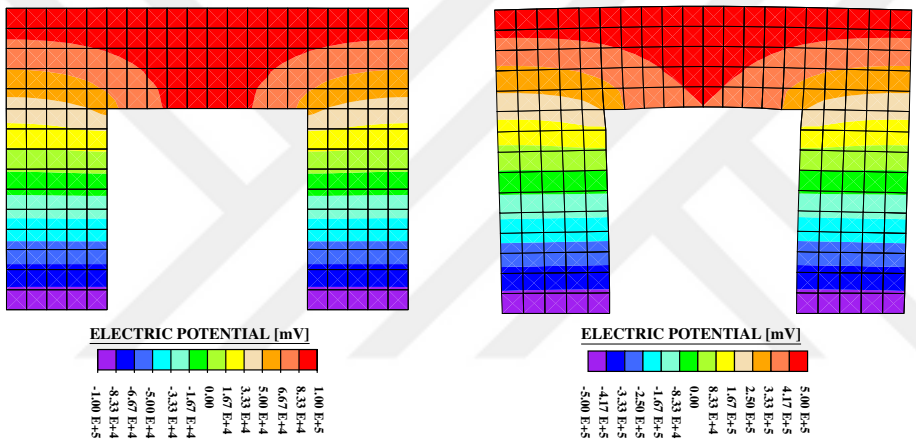

Figure 5.9: $\epsilon_r = 5\epsilon_0$ with electric potentials applied on upper and lower boundary of the plate.

For $\epsilon_r = 5\epsilon_0$, 200 V potential difference is not enough to deform the body. When such difference increases to 1 kV, it is then observed considerable amount of deformations. Similar results can be observed in Figure 5.10. It can be stated that the difference in electrical potential required to deform the body remarkably decreases as the relative permittivity value increases. Figure 5.9 and Figure 5.10 can be compared to examine. Accordingly, with lower electric potential differences, that is $\Delta\phi = 600$ V, considerable amount of deformation can be obtained when the relative permittivity value increases.

For $\epsilon_r = 100\epsilon_0$, $\Delta\phi = 100$ V is enough to deform the body of interest. According to

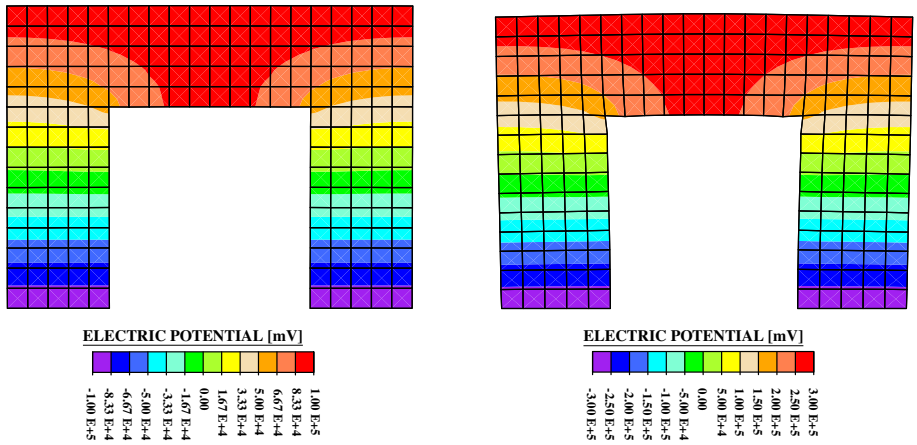

Figure 5.10: $\epsilon_r = 10\epsilon_0$ with electric potentials applied on upper and lower boundary of the plate.

[32], provided that the electric permittivity increases to $\epsilon_r = 1000\epsilon_0$, the contribution of the free space to the deformation can be neglected. The distribution of electric field for examples in Figure 5.9-5.11 show a good agreement with the results in [32].

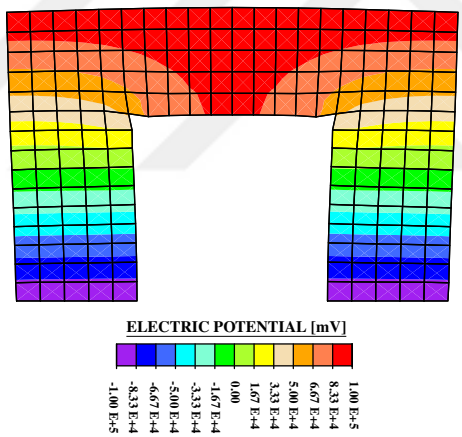

Figure 5.11: $\epsilon_r = 100\epsilon_0$ with electric potentials applied on upper and lower boundary of the plate.

5.2 Pattern Transformations in Porous Elastomers

In nature, materials may possess cell type structures which has periodically ordered occurance in their microstructures [3, 6, 7]. Hence, imitating periodic characteristics in the design and manufacturing of these materials, they can be employed in differ-

ent engineering applications. When the mechanical properties of these materials are searched, it is observed that under compressive loadings, due to the periodicity of the microstructure of the material, the pattern of the material in its initial state may change. Using Model III in (3.20), geometry whose periodic structure is presented in Figure 5.12 is examined to compare the results with the articles [4, 5]. In Figure 5.12, the body consists of about 1000 quadratic, triangular, plane strain elements, which is generated in ABAQUS/CAE [52]. However, the number of elements used for convergence analysis is more than 1000. It must be emphasized that at least four elements must be used for the region between circular voids and the edge at which PBC are defined for more precise results. The reason why PBC are defined on the left and right edges is that whole structure is semi-infinite such that the domain repeats itself in the lateral direction. Note that positions of the nodes on the left surface $\partial\mathcal{B}^-$ of the body $\mathcal{B}$ is denoted as $\boldsymbol{X}^- \in \partial\mathcal{B}^-$ and on the right surface $\partial\mathcal{B}^+$ of the body is specified as $\boldsymbol{X}^+ \in \partial\mathcal{B}^+$.

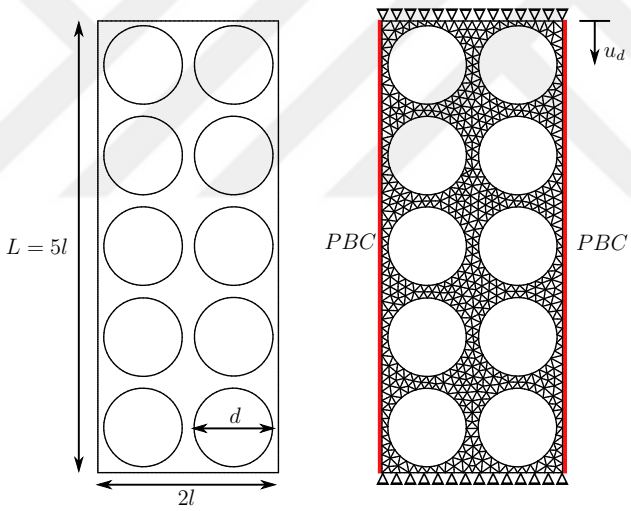

Figure 5.12: The dimensions of periodic microstructures (left) and quadratic triangular mesh and boundary conditions (right).

Besides, the nodal displacement vectors for the nodes on $\partial\mathcal{S}^-$ and $\partial\mathcal{S}^+$ are shown by $\boldsymbol{d}^-$ and $\boldsymbol{d}^+$, respectively. In Figure 5.12, PBC (*Periodic Boundary Conditions*) means that two corresponding degrees of freedom at each node on PBC are linked such that the global equation numbers for the corresponding nodes are the same. In

other words, with PBC, $\boldsymbol{d}^- = \boldsymbol{d}^+$ [27, 44, 45]. The dimensions of porous solid are given in Table 5.1.

Table 5.1: Geometric properties of the microstructure

Parameter	Unit	Definition	Value
L	[mm]	Height of the solid	49.85
l	[mm]	Size of a single unit cell	9.97
d	[mm]	Diameter of circular hole	8.67

The solid undergoes the uniform vertical displacement u_d on the upper edge as can be seen in Figure 5.12. Uniform compressive displacement is applied such that the nominal strain u_d/L is taken to a maximum of 0.1. Furthermore, this displacement is applied in 200 equal loading steps. For the given boundary value problem, the deformed shape of the specimen consisting of 2 by 5 unit cells at $u_d = 4.985$ mm is illustrated for about 1000 elements in Figure 5.13.

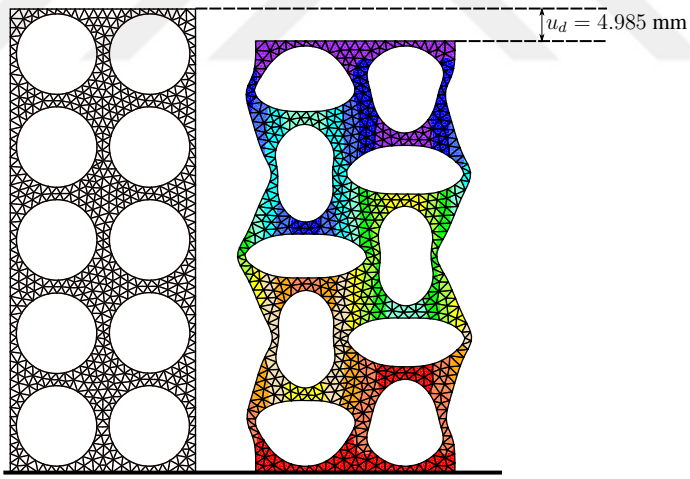

Figure 5.13: The pattern transformation between undeformed and deformed state.

It is observed that when the compression is applied on the specimen circular voids transform into elliptical voids whose major axes are perpendicular to each other due to local buckling on the ligaments [4, 5, 6, 7]. The ligament is, by definition, the ma-

terial thickness between two neighboring voids. Hence, before global buckling, local buckling, which alters the origin periodicity condition dominates the deformation. This is called a pattern transformation.

The nominal stress $f/2l$ where f is the reaction force and the nominal strain u_d/L results can be obtained from the analysis. Since it is a displacement-driven process, the nominal stress can be calculated using the reaction forces per unit thickness. The nominal stress-strain graph is provided for comparison with [4, 5] in Figure 5.14.

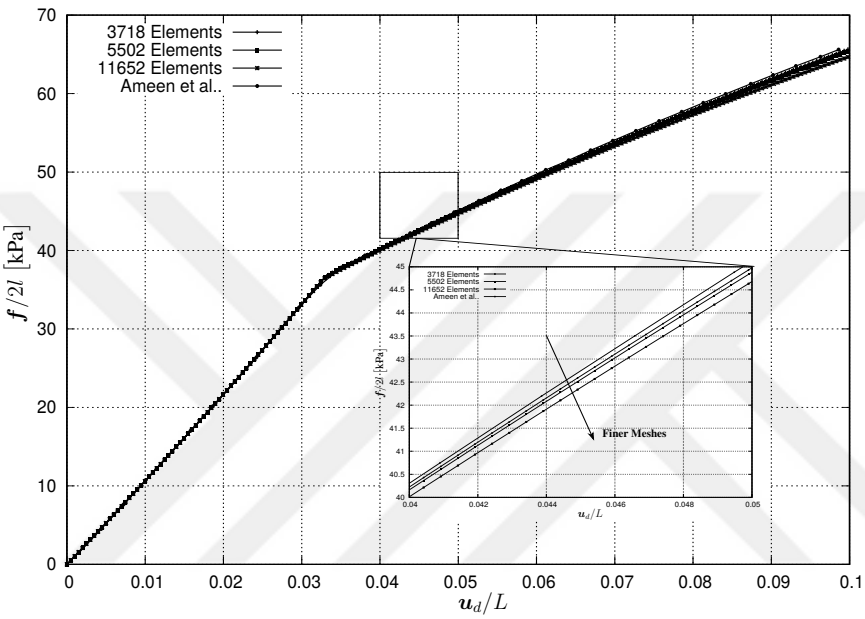

Figure 5.14: Comparison of the nominal stress-strain graph for different meshes with [4, 5].

From Figure 5.14, although the nominal stress-strain graph may appear to be an elastoplastic behavior with some hardening; in fact, it is completely elastic. This is a result of geometric instability [4, 5, 6]. In addition, when the number of finite elements increases, the nominal stress-strain values approaches to the results of [4, 5]. However, the time and the cost to solve the system also increases when the mesh is finer. As a consequence, the purely mechanical pattern transformation of the materials with periodic microstructures is accomplished for further analyses. In the next subsection, the pattern transformation of EAPs under electro-mechanical effects is to be determined.

5.3 Pattern Transformations in Porous EAPs Under Electromechanical Loading

In this section, the coupled electromechanical interaction is investigated in EAPs with porous microstructures. In other words, the material model defined for Model II is assigned to a geometry with a periodic and porous microstructure to examine the coupled electromechanical behavior. Two different analyzes are conducted. First, a constant electric field is applied to each element in the body. Second, the deformations under the associated electromechanical effects is examined under the action of electrical potentials applied to the surfaces mentioned.

5.3.1 Uniform Electric Field in Elements

At first, the microstructure shown in Figure 5.15a is employed such that electric field is uniformly applied over each element in the body. Note that the dimensions of the body is the same as ones in Figure 5.12 and PBC is applied again on the left and right surfaces of the body.

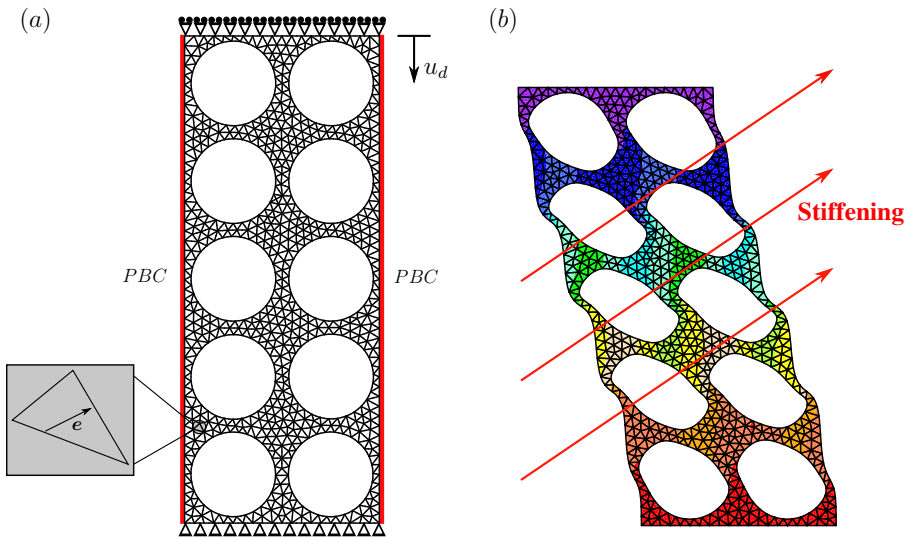

Figure 5.15: (a) Uniform electric field applied in each element $\mathcal{B}^e$ (b) Deformed shape of the periodic microstructure under combined electric field and compressive load $u_d = 4.985$ mm.

The value of $x-$ and $y-$components of the applied electric field in each element $\mathcal{B}^e$ is presented in Table 5.2.

Table 5.2: The value of $x-$ and $y-$components of the applied electric field in each element $\mathcal{B}^e$

Parameter	Unit	Definition	Value
$\boldsymbol{e}_x$	[mV/mm]	$x-$component of electric field	4×10^5
$\boldsymbol{e}_y$	[mV/mm]	$y-$component of electric field	2×10^5

In this boundary value problem, the upper edge is uniformly displaced u_d in $y-$ direction, whereas it is free to move in the $x-$direction as shown in Figure 5.15a. When the electric field 4.47×10^5 mV/mm is applied in the direction at an angle 26.56°, the material stiffens in that direction, causing the material to deform according to the stiffening effect. Hence, the deformed shape is obtained as in Figure 5.15b.

In the following example, constant electric field vectors having the same magnitude but different directions are applied to different parts of the body. Specifically, the electric field vectors are applied to the upper two and the lower two rows of the microstructure which are symmetrically applied to the middle of the microstructure as shown in Figure 5.16a. Being different from Figure 5.15, uniform vertical displacement is applied on the upper edge of the microstructure and this edge is fixed not to move in the $x-$direction. By applying the electric field vectors in this way and under the effect of the specified boundary conditions, the microstructure tends to bend. As a result of this bending, a completely new pattern is formed, which is totally different from the pattern created only by mechanical loads, see Figure (5.13). In other words, the ellipses whose major axes are perpendicular to each other formed by compression are transformed into the deformed configuration illustrated in Figure 5.16b.

The values of $x-$ and $y-$components of the applied electric fields $\boldsymbol{e}_1$ and $\boldsymbol{e}_2$ is presented in Table 5.3. Subjected to the constant electric field applied in the specified portions of the microstructure, the nominal stress-strain curve of the body is demonstrated in Figure 5.17.

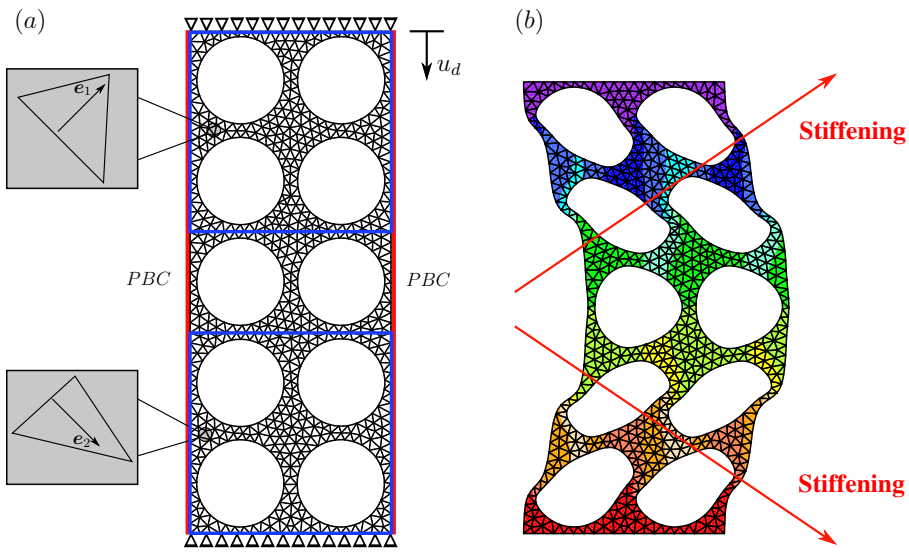

Figure 5.16: (a) Uniform electric field which the magnitude but different directions applied to different portions of the microstructure (b) Deformed shape of the periodic microstructure under combined electric fields in different directions and compressive load.

Table 5.3: The value of $x-$ and $y-$components of the applied electric fields $\boldsymbol{e}_1$ and $\boldsymbol{e}_2$

Parameter	Unit	Definition	Value
$\boldsymbol{e}_{1x}$	[mV/mm]	$x-$component of electric field, $\boldsymbol{e}_1$	5×10^5
$\boldsymbol{e}_{1y}$	[mV/mm]	$y-$component of electric field, $\boldsymbol{e}_1$	5×10^5
$\boldsymbol{e}_{2x}$	[mV/mm]	$x-$component of electric field, $\boldsymbol{e}_2$	5×10^5
$\boldsymbol{e}_{2y}$	[mV/mm]	$y-$component of electric field, $\boldsymbol{e}_2$	-5 $\times 10^5$

The $x-$component of the electric field vector applied in the elements in the upper and lower portions demonstrated as in Figure 5.16, is changed while the $y-$component is kept constant. In Figure 5.17, $\boldsymbol{e}_{1x} = \boldsymbol{e}_{2x} = 4 \times 10^5$mV/mm and $\boldsymbol{e}_{1x} = \boldsymbol{e}_{2x} = 5 \times 10^5$mV/mm are compared with the only compression case. It is observed that for the case in which the constant electric field vector is applied as in Figure 5.16, the nominal stress-strain behavior of the microstructure increases in the presence of the electric field. Furthermore, the ultimate stress values are almost the same for both

$e_{1x} = 4 \times 10^{5}$mV/mm and $e_{1x} = 5 \times 10^{5}$mV/mm loading case.

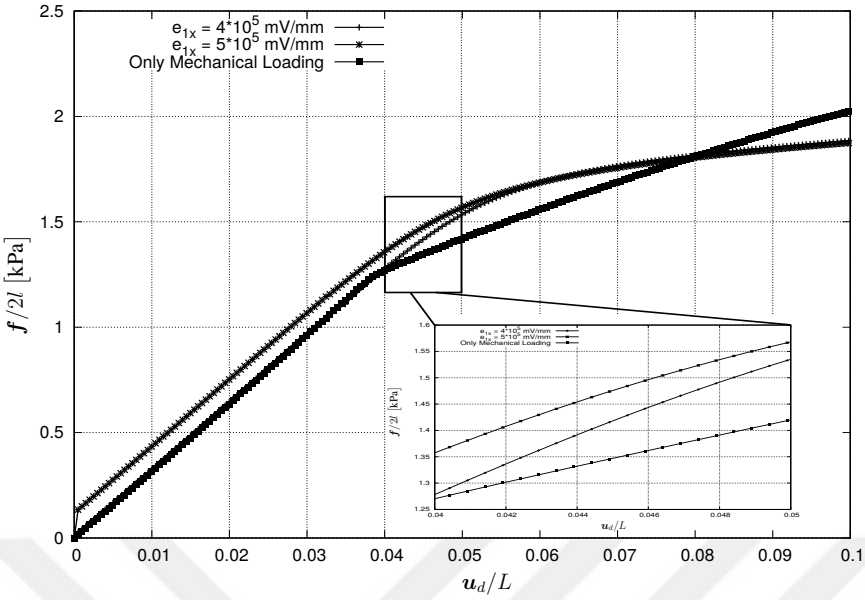

Figure 5.17: Nominal stress-strain graph for constant electric fields applied on different portions of the microstructure.

This approach provides pronounced results. Nonetheless, the more realistic scenario is needed for the application point of view. To do so, electric potentials are applied by electrodes on the edges.

5.3.2 Uniform Electric Potentials on Edges

There are alternative configurations for the location of electrodes, hence, electric potentials. For a simpler case, the electric potentials are applied on the left and right sides of the microstructure. The electric field, by definition, is the negative value of the gradient of the electric potential. Hence, the variation of electric field changed over the volume of the microstructure. However, such a variation is not directly proportional through the volume since the microstructure does not have homogeneity. Moreover, the boundary conditions are prescribed on the surface of the geometry as in Figure 5.15a. The only difference is that electric potentials are applied on the edges where PBC are defined as shown in Figure 5.18a.

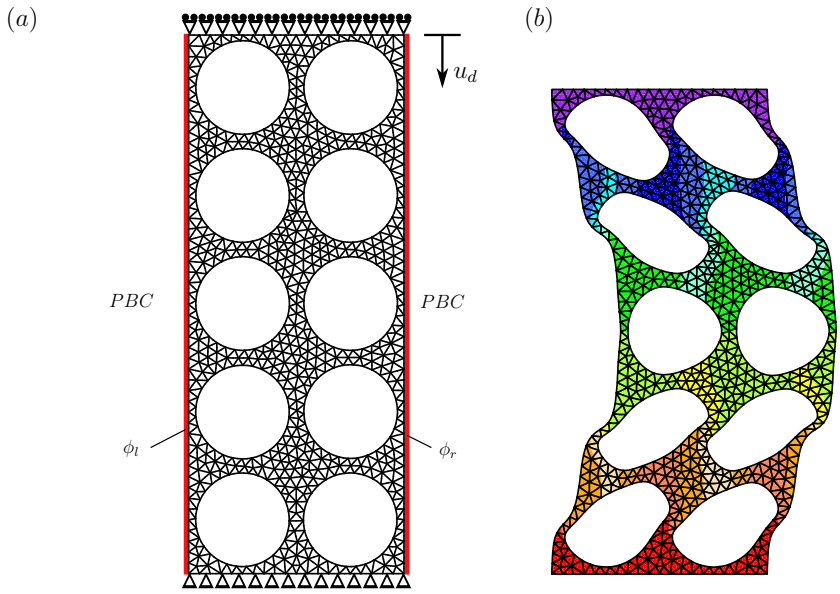

Figure 5.18: (a) Electric potentials are employed on the left and right edge of the microstructure and (b) Deformed shape of the periodic microstructure under the influence of applied electric potentials and compression.

By the application of electric potentials on the left and right edges of the microstructure, its deformed shape is obtained as shown in Figure 5.18b. Employing the electric potentials, the nominal stress-strain curve of the microstructure is presented in Figure 5.19.

It must be emphasized that the model is allowed to deform due to the electric potential difference at first; prior to the application of vertical deformation, the body buckles due to the applied electric potential difference. Later, the compression is applied in the presence of the electric potential difference. Under this combined loading, the deformed shape in Figure 5.18b is obtained at $u_d = 4.985$ mm.

Employing the electric potentials along with the mechanical loading, the nominal stress values increase when the electric potential difference increases up to a certain limit. However, it should be noted that the applied voltage differences are huge. Therefore, additional analyzes are conducted for the same model with edge lengths three orders of magnitude shorter. Hence, the unit of lengths become in μm.

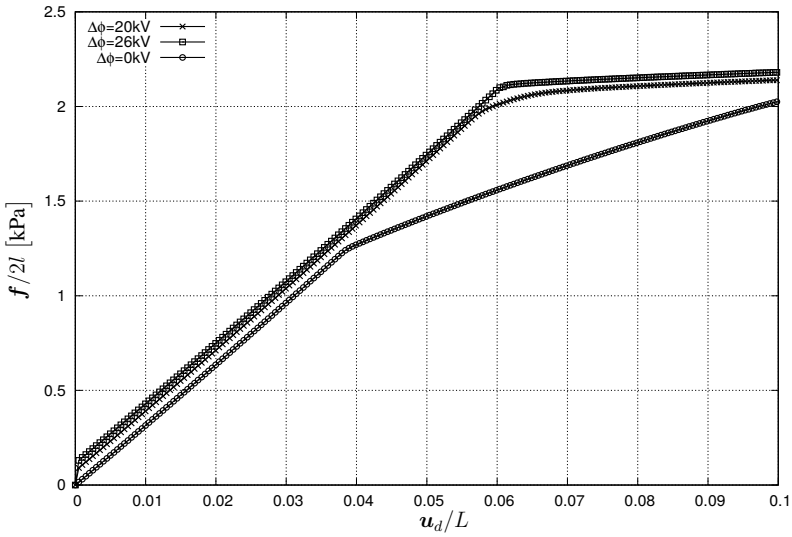

Figure 5.19: Nominal stress-strain graph for applied electric potentials on the left and right surfaces of the microstructure.

5.3.3 Uniform Electric Potentials on Edges For Microscale Model

In this section, the same geometry is created with different edge lengths. The edge lengths were reduced to the order of microns, unlike the previous examples. A sample of micron sized is thus scaled by far 10^{-3}. For this example, the electric potential is applied to the side edges as well. However, unlike the previous examples, the values of the electrical potentials applied are much smaller due to size differences. Geometry and boundary conditions are applied as in Figure 5.18a. However, before the coupled electromechanical equation system was solved iteratively, the sample was deformed by applying the electric field resulting from the difference between the electrical potentials and then the stability behavior was examined by applying compression. In addition, since the smaller sample is used for the current analysis, the value of the applied compression is reduced by the same ratio. The deformed shapes of the microstructure for different electric potentials are provided in Figure 5.20.As can be observed from Figure 5.20, the applied electric potential differences to deform the microstructure is comparably small. The nominal stress-strain behavior of the corresponding deformations is presented in Figure 5.21.

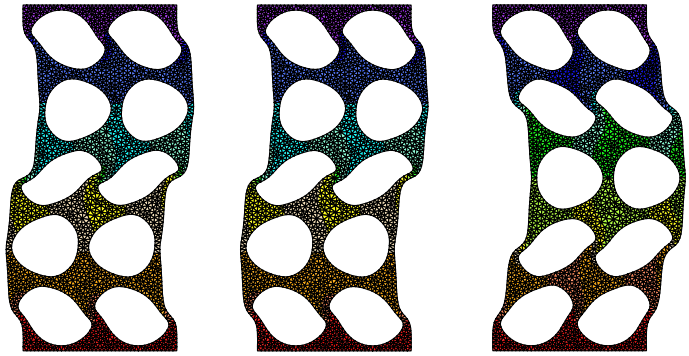

Figure 5.20: Deformed shapes of the periodic microstructure under combined electric field and compressive load.

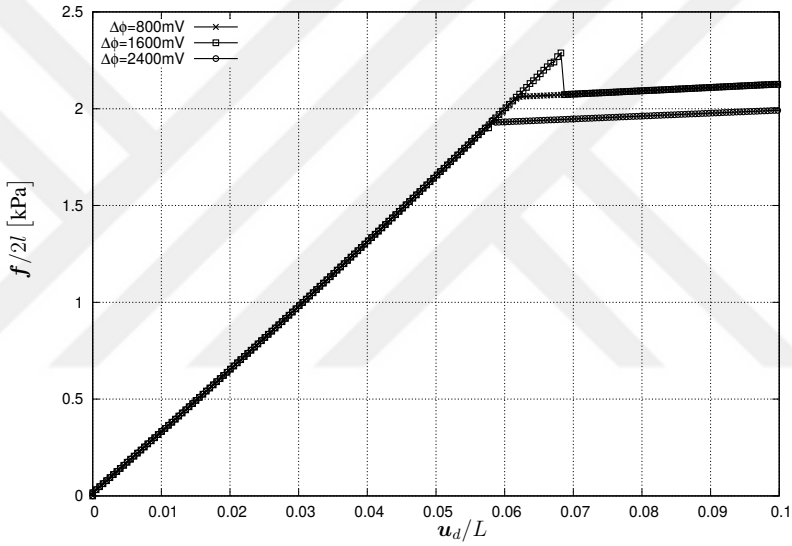

Figure 5.21: Nominal stress-strain graph for applied electric potentials on the left and right surfaces of the micron sized microstructure.

Up to certain electric potential differences, micron sized specimen exhibits the sway type deformation. However, prior to vertical displacement, when the applied electric potential difference is $\Delta\phi = 2400$ mV, the micron sized solid body is predeformed due to electric field and the mode switch can be obtained. Moreover, it must be emphasized that the maximum nominal stress increases when the higher electric potential difference is applied on the side edges of the solid.

CHAPTER 6

CONCLUSION

In this thesis, the pattern transformation of Electro-Active Polymers (EAPs) under coupled electromechanical effects has been investigated within the framework of FEM. Three representative numerical examples have been proposed for verification. Among these three examples, the first two have been examined for the coupled electromechanical effects and the last one has been solved considering mechanical instability of porous cellular microstructures. In the first of the examples, the relative electrical permittivity value is defined as deformation-dependent [10]. Moreover, considering the incompressible behavior of EAPs, the four-field FEM has been used for discretization. On the other hand, the relative permittivity is defined independent of the deformation in [32]. Also, only the standard FEM has been used for verification in the second example. In the last example of numerical examples for verification, computational investigation on the stability analysis of elastomeric materials whose microstructures exhibit periodic occurances has been conducted. The models in [4, 5] for given periodic boundary conditions have been verified using FEM. The pattern transformation of the 2D porous solids shown in [4, 5] has been tested for only mechanical compression.

In literature, there are no studies on pattern transformation of EAPs with periodic porous microstructures with coupled electromechanical interaction. To fill this gap, an additional examples have been studied where both the electromechanical coupling and the pattern transformation have been examined. Under entirely mechanical compression, the pattern transformation of periodic microstructures manifest itself in the form where the initially circular voids become ellipses whose major axes are perpendicular to each other. It has been observed in the analyses, in the presence of electric

field, the mode shape can be shifted to another one. When electrical potentials are applied to the geometry in which the geometry is then subjected to the progressively increasing mechanical loading only, the order of these potentials to change the deformation mode of the geometry is still relatively large. Hence, the micron-sized geometry has also been analyzed to investigate the influence of size on the order of the electric potentials applied. It has been realized that there is a significant decrease in the order of electrical potentials applied when it is compared with the decrease in the size of porous microstructure.

In this thesis, the geometric stability analysis has been investigated by conducting the stability analysis of the EAPs having periodic microstructures. Thus, controllable mode changes can be achieved through the small electrical potential differences applied. It is possible to obtain more optimized results in the future by conducting design studies of this claim of materials with periodic microstructure. This study can be further enhanced by computational homogenization method for coupled electromechanics. Furthermore, it is thought that these materials may be applicable in aerospace applications, especially in morphing technology. Hence, design studies could be beneficial for the aerospace applications. It is known that Refined Eigen Analysis (REA) shows a good agreement with the experimental studies [6]. Since the REA utilizes the enlarged system consisting of more than one unit cell, the time required to solve the system is relatively high. Therefore, more economical investigation for the prediction of the onset of instability which is called as Bloch-Floquet wave analysis is to be employed in the future studies.

REFERENCES

[1] Y. Bar-Cohen and Q. Zhang, "Electroactive polymer actuators and sensors," *MRS Bulletin*, vol. 33, no. 3, p. 173–181, 2008.

[2] K. J. Kim and S. Tadokoro, "Electroactive polymers for robotic applications," *Artificial Muscles and Sensors*, vol. 23, p. 291, 2007.

[3] P. Vukusic and J. R. Sambles, "Photonic structures in biology," *Nature*, vol. 424, no. 6950, p. 852, 2003.

[4] M. M. Ameen, O. Rokoš, R. Peerlings, and M. Geers, "Size effects in nonlinear periodic materials exhibiting reversible pattern transformations," *Mechanics of Materials*, vol. 124, pp. 55–70, 2018.

[5] O. Rokoš, M. M. Ameen, R. Peerlings, and M. Geers, "Micromorphic computational homogenization for mechanical metamaterials with patterning fluctuation fields," *Journal of the Mechanics and Physics of Solids*, vol. 123, pp. 119–137, 2019.

[6] K. Bertoldi, M. C. Boyce, S. Deschanel, S. Prange, and T. Mullin, "Mechanics of deformation-triggered pattern transformations and superelastic behavior in periodic elastomeric structures," *Journal of the Mechanics and Physics of Solids*, vol. 56, no. 8, pp. 2642–2668, 2008.

[7] K. Bertoldi and M. Boyce, "Mechanically triggered transformations of phononic band gaps in periodic elastomeric structures," *Physical Review B*, vol. 77, no. 5, p. 052105, 2008.

[8] Y. Bar-Cohen and Y. Bar-Cohen, *Electroactive polymer (EAP) actuators as artificial muscles: reality, potential, and challenges*, vol. 136. SPIE press Bellingham, WA, 2004.

[9] D. Zäh, *Variational homogenization in electro-mechanics: from micro-electro-elasticity to electroactive polymers*. PhD thesis, University of Stutgart, 2014.

[10] M. Jabareen, “On the modeling of electromechanical coupling in electroactive polymers using the mixed finite element formulation,” *Procedia IUTAM*, vol. 12, pp. 105–115, 2015.

[11] G. Kofod, *Dielectric elastomer actuators*. PhD thesis, The Technical University of Denmark, 2001.

[12] N. Triantafyllidis, M. Nestorović, and M. Schraad, “Failure surfaces for finitely strained two-phase periodic solids under general in-plane loading,” *Journal of Applied Mechanics*, vol. 73, no. 3, pp. 505–515, 2006.

[13] T. Mullin, S. Deschanel, K. Bertoldi, and M. C. Boyce, “Pattern transformation triggered by deformation,” *Physical review letters*, vol. 99, no. 8, p. 084301, 2007.

[14] Y. Bar-Cohen, “Biomimetics: biologically inspired technology,”

[15] D. Rosato, *On the Formulation and Numerical Implementation of Dissipative Electro–Mechanics at Large Strains*. PhD thesis, University of Stutgart, 2010.

[16] R. E. Pelrine, R. D. Kornbluh, and J. P. Joseph, “Electrostriction of polymer dielectrics with compliant electrodes as a means of actuation,” *Sensors and Actuators A: Physical*, vol. 64, no. 1, pp. 77–85, 1998.

[17] J. Su, J. Harrison, T. S. Clair, Y. Bar-Cohen, and S. Leary, “Electrostrictive grafr elastomers and applications,” *MRS Online Proceedings Library Archive*, vol. 600, 1999.

[18] A. Ask, A. Menzel, and M. Ristinmaa, “Modelling of viscoelastic dielectric elastomers with deformation dependent electric properties,” *Procedia IUTAM*, vol. 12, pp. 134 – 144, 2015. IUTAM Symposium on Mechanics of Soft Active Materials.

[19] J. D. W. Madden, N. A. Vandesteeg, P. A. Anquetil, P. G. Madden, A. Takshi, R. Z. Pytel, S. R. Lafontaine, P. A. Wieringa, and I. W. Hunter, “Artificial muscle technology: physical principles and naval prospects,” *IEEE Journal of Oceanic Engineering*, 2004.

[20] J.-S. Plante and S. Dubowsky, "On the performance mechanisms of dielectric elastomer actuators," *Sensors and Actuators A: Physical*, vol. 137, no. 1, pp. 96–109, 2007.

[21] T. Tanaka, I. Nishio, S.-T. Sun, and S. Ueno-Nishio, "Collapse of gels in an electric field," *Science*, vol. 218, no. 4571, pp. 467–469, 1982.

[22] T. Shiga and T. Kurauchi, "Deformation of polyelectrolyte gels under the influence of electric field," *Journal of Applied Polymer Science*, vol. 39, no. 11-12, pp. 2305–2320, 1990.

[23] A. C. Eringen, "On the foundations of electroelastostatics," *International Journal of Engineering Science*, vol. 1, no. 1, pp. 127–153, 1963.

[24] R. A. Toupin, "The elastic dielectric," *Journal of Rational Mechanics and Analysis*, vol. 5, no. 6, pp. 849–915, 1956.

[25] H. Tiersten, "On the nonlinear equations of thermo-electroelasticity," *International Journal of Engineering Science*, vol. 9, no. 7, pp. 587–604, 1971.

[26] L. Dorfmann and R. W. Ogden, *Nonlinear theory of electroelastic and magnetoelastic interactions*. Springer, 2014.

[27] E. Polukhov, D. Vallicotti, and M.-A. Keip, "Computational stability analysis of periodic electroactive polymer composites across scales," *Computer Methods in Applied Mechanics and Engineering*, vol. 337, pp. 165 – 197, 2018.

[28] J. C. Simo and R. L. Taylor, "Quasi-incompressible finite elasticity in principal stretches. continuum basis and numerical algorithms," *Computer methods in applied mechanics and engineering*, vol. 85, no. 3, pp. 273–310, 1991.

[29] C. Miehe, "Aspects of the formulation and finite element implementation of large strain isotropic elasticity," *International Journal for Numerical Methods in Engineering*, vol. 37, no. 12, pp. 1981–2004, 1994.

[30] D. K. Vu, P. Steinmann, and G. Possart, "Numerical modelling of non-linear electroelasticity," *International Journal for Numerical Methods in Engineering*, vol. 70, no. 6, pp. 685–704.

[31] D. Vu and P. Steinmann, "A 2-d coupled bem–fem simulation of electro-elastostatics at large strain," *Computer Methods in Applied Mechanics and Engineering*, vol. 199, no. 17-20, pp. 1124–1133, 2010.

[32] P. Steinmann and D. K. Vu, "Computational challenges in the simulation of nonlinear electroelasticity," *Computer Assisted Methods in Engineering and Science*, vol. 19, no. 3, pp. 199–212, 2017.

[33] S. Thylander, A. Menzel, and M. Ristinmaa, "An electromechanically coupled micro-sphere framework: application to the finite element analysis of electrostrictive polymers," *Smart Materials and Structures*, vol. 21, no. 9, p. 094008, 2012.

[34] A. Ask, A. Menzel, and M. Ristinmaa, "On the modelling of electro-viscoelastic response of electrostrictive polyurethane elastomers," in *IOP Conference Series: Materials Science and Engineering*, vol. 10, p. 012101, IOP Publishing, 2010.

[35] A. Ask, R. Denzer, A. Menzel, and M. Ristinmaa, "Inverse-motion-based form finding for quasi-incompressible finite electroelasticity," *International Journal for Numerical Methods in Engineering*, vol. 94, no. 6, pp. 554–572, 2013.

[36] K. Bertoldi, P. M. Reis, S. Willshaw, and T. Mullin, "Negative poisson's ratio behavior induced by an elastic instability," *Advanced materials*, vol. 22, no. 3, pp. 361–366, 2010.

[37] J. T. Overvelde, S. Shan, and K. Bertoldi, "Compaction through buckling in 2d periodic, soft and porous structures: effect of pore shape," *Advanced Materials*, vol. 24, no. 17, pp. 2337–2342, 2012.

[38] K. Bertoldi and M. C. Boyce, "Wave propagation and instabilities in monolithic and periodically structured elastomeric materials undergoing large deformations," *Physical Review B*, vol. 78, no. 18, p. 184107, 2008.

[39] J. T. Overvelde and K. Bertoldi, "Relating pore shape to the non-linear response of periodic elastomeric structures," *Journal of the Mechanics and Physics of Solids*, vol. 64, pp. 351–366, 2014.

[40] K. Bertoldi, "Stability of periodic porous structures," in *Extremely Deformable Structures* (D. Bigoni, ed.), ch. 5, pp. 157–178, Springer, 2015.

[41] X. Ning and S. Pellegrino, "Bloch wave buckling analysis of axially loaded periodic cylindrical shells," *Computers & Structures*, vol. 177, pp. 114–125, 2016.

[42] M. Åberg and P. Gudmundson, "The usage of standard finite element codes for computation of dispersion relations in materials with periodic microstructure," *The Journal of the Acoustical Society of America*, vol. 102, no. 4, pp. 2007–2013, 1997.

[43] C. Miehe, "Strain-driven homogenization of inelastic microstructures and composites based on an incremental variational formulation," *International Journal for Numerical Methods in Engineering*, vol. 55, no. 11, pp. 1285–1322, 2002.

[44] C. Miehe, J. Schotte, and M. Lambrecht, "Homogenization of inelastic solid materials at finite strains based on incremental minimization principles. application to the texture analysis of polycrystals," *Journal of the Mechanics and Physics of Solids*, vol. 50, no. 10, pp. 2123–2167, 2002.

[45] C. Miehe, J. Schröder, and M. Becker, "Computational homogenization analysis in finite elasticity: material and structural instabilities on the micro-and macro-scales of periodic composites and their interaction," *Computer Methods in Applied Mechanics and Engineering*, vol. 191, no. 44, pp. 4971–5005, 2002.

[46] S. Göktepe, *Micro-macro approaches to rubbery and glassy polymers: Predictive micromechanically-based models and simulations*. PhD thesis, University of Stutgart, 2007.

[47] G. Holzapfel, "Nonlinear solid mechanics. a continuum approach for engineering," 2001.

[48] F. W. Sears, M. W. Zemansky, and H. D. Young, *University physics*. Addison-Wesley, 1987.

[49] B. D. Coleman and W. Noll, "The thermodynamics of elastic materials with heat conduction and viscosity," in *The Foundations of Mechanics and Thermodynamics*, pp. 145–156, Springer, 1974.

[50] M. Wissler and E. Mazza, “Electromechanical coupling in dielectric elastomer actuators,” *Sensors and Actuators A: Physical*, vol. 138, no. 2, pp. 384–393, 2007.

[51] R. L. Taylor, “FEAP - finite element analysis program,” 2014.

[52] D. Systèmes, “Abaqus 6.10: Analysis user’s manual,” *Providence, RI: Dassault Systèmes Simulia Corp*, 2010.